

Habilitation à diriger des recherches

Quantum effects in nanoscale condensed matter systems

— **Guillaume Weick** —

Maître de Conférences

Institut de Physique et Chimie des Matériaux de Strasbourg
Université de Strasbourg & CNRS

Présenté le 7 juillet 2015 devant la commission d'examen composée de

Prof. William L. Barnes	Examineur	(University of Exeter)
Prof. Tobias Brandes	Rapporteur externe	(TU-Berlin)
Prof. Piet Brouwer	Examineur	(FU-Berlin)
Prof. Didier Felbacq	Rapporteur externe	(L2C, Montpellier)
Prof. Rodolfo A. Jalabert	Invité	(IPCMS, Strasbourg)
Prof. Guido Pupillo	Rapporteur interne	(IPCMS & ISIS, Strasbourg)
Dr. Fabrice Vallée	Examineur	(ILM, Villeurbanne)
Dr. Dietmar Weinmann	Garant	(IPCMS, Strasbourg)

Contents

Foreword	vii
1 Nanoelectromechanical systems close to mechanical instabilities	11
1.1 Introduction	11
1.2 Enhanced current blockade in suspended single-electron transistors	13
1.2.1 Model	13
1.2.2 Current-induced Langevin dynamics	15
1.2.3 Current blockade	16
1.2.4 Large current noise	22
1.2.5 Role of cotunneling on the current blockade	27
1.3 Current-induced discontinuous Euler instability	30
1.4 Conclusion	33
2 A plasmonic analogue of graphene	35
2.1 Introduction	35
2.2 Dirac plasmons in honeycomb arrays of metallic nanoparticles	36
2.2.1 Model	37
2.2.2 Analogy with massless Dirac fermions in graphene	38
2.2.3 Collective plasmon dispersion	39
2.2.4 Dirac-like collective plasmons	40
2.2.5 Concluding remarks	42
2.3 How do the dark and bright plasmonic modes decay in a metallic nanoparticle dimer?	43
2.3.1 Model	43
2.3.2 Coupled plasmonic modes	45
2.3.3 Landau damping	46
2.3.4 Absorption and radiation losses	48
2.3.5 Discussion	48
2.3.6 Concluding remarks	50
2.4 Coupling of collective plasmons to light: plasmon polaritons	50
2.4.1 Arrays of interacting metallic nanoparticles	51
2.4.2 Collective plasmon dispersion	52
2.4.3 Coupling to light	53
2.4.4 Plasmon polariton dispersion	54
2.4.5 Concluding remarks	56
2.5 Conclusion	57
3 Parametric resonances in many-body fermionic systems	59
3.1 Introduction	59
3.2 Parametric resonance in a one-dimensional interacting Fermi system	60

Contents

3.2.1	Model	61
3.2.2	Parametric amplification	62
3.2.3	Fermionic momentum distribution	63
3.2.4	Experimental realization	66
3.3	Parametric amplification of collective modes in a two-dimensional fermionic system	66
3.3.1	Model	67
3.3.2	Parametric resonance of the magnetoplasmons	69
3.3.3	Effects of damping and anharmonicities on the parametric resonance of the magnetoplasmons	70
3.3.4	Experimental consequences	73
3.4	Conclusion	74
4	Research project: Novel quantum metamaterials based on metallic nanoparticles	77
4.1	Scientific context at IPCMS	77
A	Résumé détaillé en français	79
	Bibliography	91

Foreword

The present “habilitation à diriger des recherches” (habilitation thesis) summarizes the research activities I have been conducting in the field of condensed matter theory since the end of my PhD thesis, which I defended in September 2006. During my PhD, which was under the regime of “cotutelle” and cosupervised by Gert Ingold (Universität Augsburg) and Rodolfo Jalabert (Université Louis Pasteur, Strasbourg), I investigated the electron dynamics in single metallic nanoparticles. Motivated by experiments conducted in the group of Jean-Yves Bigot [1–3] at the Institut de Physique et Chimie des Matériaux de Strasbourg (IPCMS), I was in particular interested in developing a consistent theoretical framework [4–9] for understanding the mechanisms leading to the finite lifetime of collective electronic excitations in nanoscale metallic clusters.

In order to explore new research topics, I moved to Berlin in October 2006 for taking up a post-doctoral position in the Quantum Transport group of Felix von Oppen at the Freie Universität (FU). I entered into the field of nanoelectromechanical systems (NEMS), in which a tiny movable mechanical object (such as, e.g., a single molecule, a nanoresonator or a suspended carbon nanotube) is coupled to electronic transport [10–12]. In particular, I was involved in a project aiming at understanding how the current flow from a scanning tunneling microscope tip to a molecule presenting different conformations can induce the switching between its different isomers [13]. This work, motivated by experiments [14] conducted in the group of Nacho Pascual at the FU (now in San Sebastian), was performed in collaboration with a PhD student (Florian Elste), Carsten Timm (Technische Universität Dresden) and Felix von Oppen. Together with Fabio Pistolesi (Bordeaux), Eros Mariani (back then also a postdoc at FU, now a lecturer at the University of Exeter) and Felix von Oppen, we initiated during that period a work on mechanical instabilities in NEMS [15], taking the paradigmatic Euler instability as an exemple [16,17]. Together with Eros Mariani and a Master student (Christian Graf), we also started a new line of research during these years in Berlin, namely the study of parametric resonances in interacting many-body fermionic systems [18].

In December 2009, I moved back to Strasbourg to take a three-year CNRS researcher position (CR2 CDD) at IPCMS, in the Mesoscopic Physics Team led by Rodolfo Jalabert and Dietmar Weinmann. There, in collaboration with Fabio Pistolesi and Felix von Oppen, but also with two Master students which I supervised (Dominique Meyer and Jochen Brüggemann), I further investigated in detail NEMS close to mechanical instabilities [19–21]. During that period, together with Eros Mariani, we pushed forward our understanding of parametric resonances in many-body fermionic systems [22]. It is also during these postdoc years at IPCMS that, in collaboration with Dietmar Weinmann, we predicted the existence of surface magnetoplasmons in metallic nanoparticles [23], a prediction which was recently confirmed experimentally [24,25].

In November 2011, I got appointed as a “Maître de Conférences” (tenured assistant professor) at Université de Strasbourg, in the Mesoscopic Physics Team at IPCMS, a position which I started in September 2012. Together with Eros Mariani, two of his PhD students (Claire Woollacott and Tom Sturges) and in collaboration with Bill Barnes (University of

Exeter) and Ortwin Hess (Imperial College London), we then started a project on artificial plasmonic graphene, where metallic nanoparticles form a honeycomb array and where the near-field interaction between them lead to collective modes that behave like electrons in real graphene [26–28]. Such a research line motivated further investigations of how plasmons couple to light in three-dimensional plasmonic arrays [29], and how collective plasmons decay in arrays of interacting metallic nanoparticles [30]. The latter topic is the subject of the PhD thesis of Adam Brandstetter-Kunc, which I cosupervise together with Rodolfo Jalabert. Recently, I also got involved in the problem of the transmission phase of a quantum dot in a collaboration with Rodolfo Jalabert, Hans Weidenmüller (Max Planck Institute, Heidelberg) and Dietmar Weinmann [31].

The various condensed matter systems I am investigating (metallic nanoparticles, nanoresonators, carbon nanotubes, single molecules, semiconductor quantum dots, etc.) have in common their small size (from few nanometers to micrometers), small enough (and/or at sufficiently low temperature) so that phase coherence is preserved and quantum mechanical effects show up in various properties of such systems.¹ However, these systems still contain a relatively large number of particles, large enough so that a statistical description is often needed. The appropriate approach to tackle the various questions described in this manuscript is thus the one of mesoscopic quantum physics [32–34], as exemplified in the following chapters.

The manuscript contains three chapters summarizing my research activities on nanoelectromechanical systems (Chapter 1), plasmonic metamaterials (Chapter 2) and parametrically modulated many-body fermionic systems (Chapter 3).² Each of these chapters is self-contained and can be read independently. Chapter 4 presents our ongoing research projects at IPCMS and concludes the main body of the manuscript. A general summary (in French) of the manuscript is provided in the Appendix.

More specifically, Chapter 1 describes our research activities aiming at understanding the fate of a mechanical instability in a nanoscale resonator (such as, e.g., a suspended carbon nanotube) when electric current is driven through the system. Due to the coupling between the mechanical and electronic degrees of freedom, the current flow inevitably modifies the mechanical properties of the nanoresonator and hence the nature of the mechanical instability. Due to the backaction of the nanoresonator onto the electronic degrees of freedom, the transport properties of the device are modified as well. In particular, we show in Chapter 1 how the Euler buckling instability, which is the paradigm of a continuous mechanical instability, can be exploited so as to effectively increase by orders of magnitude the effect of the electromechanical coupling on the current-voltage and noise characteristics of the system. Remarkably, we further show that an electron-phonon coupling intrinsic to the nanoresonator changes qualitatively the nature of the Euler instability, turning it into a discontinuous one for certain parameter ranges.

Chapter 2 summarizes our recent activities in the field of plasmonic metamaterials and artificial graphene. We show in this chapter that a honeycomb array of metallic nanoparticles, each supporting a localized surface plasmon and interacting through their near-field, presents collective plasmonic modes that mimic the unique properties of electrons in graphene. Indeed, when the plasmon polarization points close to the normal to the plane of the honeycomb array of nanoparticles, the spectrum presents Dirac cones, similar to those present in the

¹ Hence the title of this manuscript.

² For the sake of brevity, I decided not to include in the manuscript our work [31] on the transmission phase of quantum dots, as it is somewhat not in the lines of the research topics of Chapters 1 to 3. Also, while Refs. [13] and [23] are topicwise related to Chapter 1 and Chapters 2 & 3, respectively, these two papers are not summarized in what follows and can be read independently.

electronic band structure of graphene. We show that the corresponding plasmon eigenstates represent Dirac-like massless bosonic excitations that present similar effects to electrons in graphene, such as a nontrivial Berry phase and the absence of backscattering off smooth inhomogeneities. We further discuss how one can manipulate the Dirac points in the Brillouin zone and open a gap in the collective plasmon dispersion by modifying the polarization of the localized surface plasmons, paving the way for a fully tunable plasmonic analogue of graphene. Since plasmonic damping will inevitably limit the propagation of collective plasmons, we further study in Chapter 2 the crucial question of the finite lifetime of coupled plasmonic modes, and analyze how these bosonic excitations couple to light in a situation where the light-matter interaction is strong.

In Chapter 3, we analyze parametric resonances in many-body fermionic systems. We start by showing that the periodic modulation of the Hamiltonian parameters for one-dimensional correlated fermionic systems can be used to parametrically amplify their bosonic collective modes. Treating the problem within the Luttinger-liquid picture, we show how charge and spin density waves with different momenta are simultaneously amplified. We discuss the implementation of our predictions for cold atoms in one-dimensional modulated optical lattices. Interestingly, we show that the fermionic momentum distribution directly provides a clear signature of spin-charge separation. We then extend these ideas to the challenging case of two-dimensional systems. In particular, we show that the magnetoplasmon collective modes in quasi-two-dimensional semiconductor quantum dots can be parametrically amplified by periodically modulating the magnetic field perpendicular to the nanostructure. The two magnetoplasmon modes are excited and amplified simultaneously, leading to an exponential growth of the number of bosonic excitations in the system. We further demonstrate that damping mechanisms as well as anharmonicities in the confinement of the quantum dot lead to a saturation of the parametric amplification.

Chapter 4 describes our research project which aims at investigating novel quantum metamaterials based on metallic nanoparticles. These are the subject of active experimental investigations at IPCMS and elsewhere. The goal of our project is to bring theoretical support to these experiments. Specifically, a first part of the project aims at understanding the unusual magnetism observed in gold nanoparticles [35–39]. In particular, we plan to investigate the orbital magnetism of nanoparticle assemblies and determine whether such intriguing magnetic behaviors can be accounted for by this mechanism. A second part of the project is devoted to the investigation of the properties of plasmon polaritons in honeycomb plasmonic lattices [26–30] in order to predict experimental signatures of this peculiar nanoparticle array.

Beside my research activities briefly exposed above, a significant part of my time is devoted to teaching. I actually have the chance to teach since the beginning of my PhD studies in 2003, with the exception of my postdoc years in Strasbourg, which, opposite to my postdoc in Berlin, did not involve a teaching duty. As a *Maître de Conférences*, I am at present responsible for three modules at Université de Strasbourg.³ The first one is a lecture on classical electrodynamics for second-year students of the curriculum “*Mathématiques et Physique Approfondies*” which also involves tutorials (a so-called “*cours intégré*”). The second of these modules is a lecture on classical mechanics and special relativity for fourth-year students preparing the exam for becoming high-school teachers (CAPES). The third module I am responsible for is the tutorial of advanced statistical mechanics in the first year of the Master of Physics.

In conclusion of this foreword, I would like to acknowledge a number of people without

³ http://www.ipcms.unistra.fr/?page_id=13004

whom the research presented in this manuscript could not have been possible. I am indeed very much indebted to all the wonderful collaborators with whom I had the privilege to interact over the last years and from whom I learned a lot. In particular, I have benefited from a long and continuous collaboration with Rodolfo Jalabert, Eros Mariani, Felix von Oppen and Dietmar Weinmann. I further acknowledge fruitful collaboration with Bill Barnes, Philippe Beckrich, Adam Brandstetter-Kunc, Jochen Brüggemann, Thierry Charitat, Christian Graf, Ortwin Hess, Gert Ingold, Carlos Marques, Dominique Meyer, Rafael Molina, Fabio Pistolesi, César Seoánez, Tom Sturges, Carsten Timm, Hans Weidenmüller, and Claire Woolacott. Furthermore, I would like to express my gratitude to my colleagues Matthieu Bailleul, Stéphane Berciaud, Bertrand Donnio, Jean-Louis Gallani, François Gautier, Pierre Gilliot, Cosimo Gorini, Pablo Tamborenea, and Mircea Vomir for valuable and helpful discussions. Moreover, I would like to thank all members of the Département de Magnétisme des Objets Nanostructurés at IPCMS and of the Dahlem Center for Complex Quantum Systems in Berlin for creating a friendly and stimulating atmosphere while the research presented in this manuscript was carried on. Last, but not least, I would like to express my gratitude to Bill Barnes, Tobias Brandes, Piet Brouwer, Didier Felbacq, Guido Pupillo and Fabrice Vallée for accepting to review this habilitation thesis.

The research presented in this manuscript has been financially supported in parts by the Deutsche Forschungsgemeinschaft through Sonderforschungsbereich 658 “Elementary Processes in Molecular Switches at Surfaces”, the Centre National de la Recherche Scientifique through Projet International de Coopération Scientifique No. 6384 APAG (“A Plasmonic Analogue of Graphene”) and the Agence Nationale de la Recherche (Project No. ANR-14-CE26-0005-01 Q-MetaMat, “Quantum Metamaterials Based on Metallic Nanoparticles”).

Strasbourg, April 2015

Chapter 1

Nanoelectromechanical systems close to mechanical instabilities

1.1 Introduction

The buckling of an elastic rod by a longitudinal compression force F applied to its two ends constitutes the paradigm of a mechanical instability, called buckling instability [16]. It was first studied by Euler in 1744 while investigating the maximal load that a column can sustain [17]. As long as F stays below a critical force F_c , the rod remains straight, while for $F > F_c$ it buckles, as sketched in Figs. 1.1(a) and 1.1(b). The transition between the two states is continuous and the frequency of the fundamental bending mode vanishes at the instability.

There has been much recent interest in exploring buckling instabilities in micro- and nanomechanical systems. In the quest to understand the remarkable mechanical properties of carbon nanotubes [40–42], there have been observations of compressive buckling instabilities in this system [43]. The Euler buckling instability has been observed in SiO₂ nanobeams and shown to obey, despite the small size of these objects, continuum classical elasticity theory [44, 45]. There are also close relations with the recently observed wrinkling [46] and possibly with the rippling [47] of suspended graphene samples. Theoretical works have studied the quantum properties of nanobeams near the Euler instability [48–52], proposing this system to explore zero-point fluctuations of a mechanical mode [49] or to serve as a mechanical qubit [51, 52].

In this chapter, we study the interaction of current flow with the vibrational motion near such continuous mechanical instabilities which constitutes a fundamental issue of nanoelectromechanics [10–12]. Remarkably, we find that under quite general conditions, this problem admits an essentially exact solution due to the continuity of the instability and the consequent vanishing of the vibronic frequency at the transition (“critical slowing down”). In fact, the vanishing of the frequency implies that the mechanical motion becomes slow compared to the electronic dynamics and an appropriate non-equilibrium Born-Oppenheimer approximation becomes asymptotically exact near the transition. Here, we illustrate our general framework by applying it to the nanoelectromechanics of the Euler instability. We find that the interplay of electronic transport and the mechanical instability causes significant qualitative changes both in the nature of the buckling and in the electronic transport properties.

Nanoelectromechanical systems (NEMS) in which a nanomechanical resonator is coupled to electronic degrees of freedom [10–12] through, e.g., a single-electron transistor (SET), show spectacular effects stemming from the coupling of the mechanical part of the device to the electronic charge. These effects arise due to the reduced size of the nanoresonator, so that the backaction of the mechanical degree of freedom on the SET can have significant consequences for the transport properties. A prominent example is the low-bias current blockade that occurs in the Coulomb blockade regime when the nanoresonator is capacitively coupled to the SET

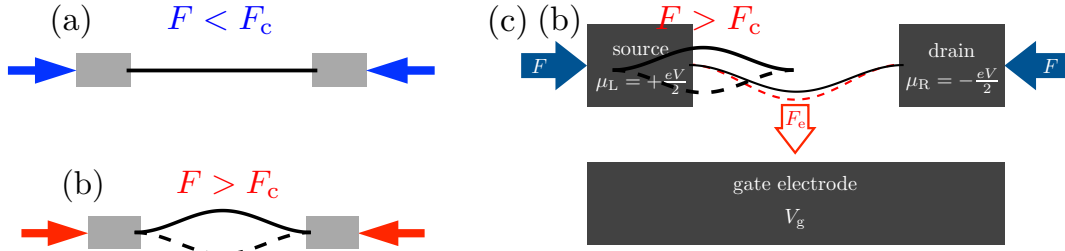


Figure 1.1: Sketch of a nanobeam (a) in the flat state and (b) the buckled state with two equivalent metastable positions of the rod (solid and dashed lines). (c) Sketch of a suspended doubly clamped nanobeam forming a quantum dot (solid black line) connected via tunnel barriers to source and drain electrodes held at chemical potentials μ_L and μ_R by the bias voltage V . The lateral force F compresses the nanobeam and may induce the buckling instability. The beam is capacitively coupled to a metallic electrode kept at a gate voltage V_g . This induces a stochastic force F_e that attracts the beam towards the gate electrode whenever the quantum dot is charged (dashed red line), inducing fluctuations of the nanobeam’s deflection and, in turn, fluctuations of the current through the device.

[53, 54]. The presence of an extra electron with charge $-e < 0$ on the central island forming a quantum dot on the suspended vibrating structure induces an electrostatic force F_e on the resonator, shifting the equilibrium position of the latter by an amount F_e/k , with k the spring constant of the oscillator [see Fig. 1.1(c)]. This induces a shift of the gate voltage $V_g \sim F_e^2/ek$ seen by the SET, and, hence, a blockade of the current through the device for bias voltages $V \lesssim F_e^2/ek$ (see the sketch in Fig. 1.2). This phenomenon is the classical counterpart of the Franck-Condon blockade (also sometimes refer to as “phonon blockade”) in molecular devices [55, 56] that has been observed in carbon nanotube-based resonators for high-energy vibrational modes [57, 58], and recently in a single-molecule junction containing an individual Fe_4 single-molecule magnet [59].¹ For classical nanoresonators, the current blockade is difficult to observe experimentally due to the relatively weak electromechanical coupling F_e to the low-energy bending modes of the suspended structure, although a precursor of this effect has been reported in the literature [41, 42].

In Sec. 1.2 we show how one can enhance the classical current blockade by orders of magnitude by exploiting the Euler buckling instability. Indeed, the spring constant k (or equivalently, the vibrational frequency of the fundamental bending mode ω) tends to zero when one brings the nanoresonator to the buckling instability with the help of a lateral compression force F (see Fig. 1.1). Thus, the energy scale F_e^2/k at which the current blockade occurs dramatically increases (cf. Fig. 1.2), rendering this phenomenon potentially observable in future experiments.

In addition to the capacitive coupling mentioned above and resulting in the classical current blockade effect, there exists a coupling which arises from the electron-phonon interaction which is intrinsic to the nanobeam [61]. In Sec. 1.3 we show that this coupling modifies qualitatively the nature of the Euler buckling instability. Indeed, the electronic dynamics can change the

¹ A low-bias current blockade has also been observed in a quantum dot embedded in a freestanding GaAs/AlGaAs membrane [60], but the interpretation of the observed phenomena is somewhat different from the Franck-Condon blockade described theoretically in Refs. [55, 56].

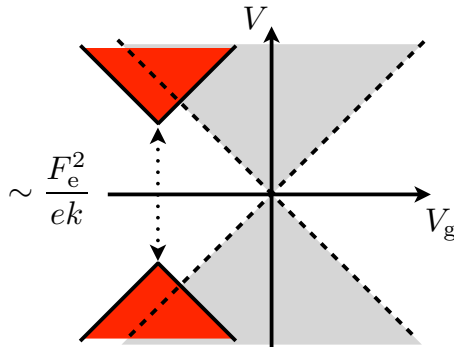


Figure 1.2: Sketch of the regions in the V - V_g plane for which the system in the Coulomb blockade regime conducts current (colored regions) in absence/presence of electromechanical coupling (gray/red regions).

nature of the buckling instability from a continuous to a discontinuous transition which is closely analogous to tricritical behavior in the Landau theory of phase transitions.

1.2 Enhanced current blockade in suspended single-electron transistors

In this first part of Chapter 1, we focus on the role played by the extrinsic capacitive coupling induced by the gate electrode, and show how one can enhance by orders of magnitude the low-bias current blockade when one brings the nanoresonator to the Euler buckling instability. We start by presenting our model in Sec. 1.2.1, while Sec. 1.2.2 is devoted to the description of the effective Langevin dynamics of the nanoresonator deflection. In Secs. 1.2.3 and 1.2.4, our main results for the I - V characteristics and the noise power spectrum of the system are presented, respectively. Finally, Sec. 1.2.5 discusses the role played by cotunneling on the current blockade phenomenon.

1.2.1 Model

We consider a quantum dot embedded in a doubly-clamped beam as shown in Fig. 1.1(c). The presence of the metallic gate near the dot, as well as the electron-phonon interaction intrinsic to the nanoresonator, are responsible for the coupling of the bending modes of the beam to the charge state of the dot. The Hamiltonian of the system can then be written as

$$H = H_{\text{vib}} + H_{\text{SET}} + H_c, \quad (1.1)$$

where H_{vib} describes the oscillating modes of the nanobeam, H_{SET} the electronic degrees of freedom of the single-electron transistor, and H_c the coupling between the SET and the resonator. The model describes, for instance, transport through suspended carbon nanotubes as considered in the experiments of Refs. [41, 42, 58, 62].

Using standard methods of elasticity theory one can show that, close to the buckling instability, the frequency ω of the fundamental bending mode of the nanobeam vanishes while those of the higher modes remain finite [16]. This allows one to retain only the fundamental mode

parametrized by the displacement X of the center of the beam. The Hamiltonian representing the oscillations of the nanobeam thus takes the Landau-Ginzburg form [19, 44, 48–50]

$$H_{\text{vib}} = \frac{P^2}{2m} + \frac{m\omega^2}{2}X^2 + \frac{\alpha}{4}X^4, \quad (1.2)$$

where P is the momentum conjugate to X . For a doubly-clamped uniform nanobeam of length L , linear mass density σ , and bending rigidity κ , one can show [49, 50] that close to the instability the effective mass of the beam is $m = 3\sigma L/8$. The fundamental bending mode frequency reads

$$\omega = \omega_0 \sqrt{1 - \frac{F}{F_c}}, \quad (1.3)$$

where F is the compression force, $F_c = \kappa(2\pi/L)^2$ the critical force at which buckling occurs, and $\omega_0 = \sqrt{\kappa/\sigma}(2\pi/L)^2$. The positive parameter $\alpha = F_c L(\pi/2L)^4$ ensures the stability of the system for $F > F_c$. For $F < F_c$, we have $\omega^2 > 0$, so that $X = 0$ is the only stable solution and the beam remains straight. For $F > F_c$, it buckles into one of the two metastable states at $X = \pm\sqrt{-m\omega^2/\alpha}$. Notice that in writing Eq. (1.2), we assumed that the nanobeam cannot rotate around its axis due to clamping at its two ends, such that the oscillation of the nanoresonator takes place in a given fixed plane, reducing the vibrational Hamiltonian to the one-dimensional form (1.2).

Electronic transport is accounted for by the SET Hamiltonian consisting of three parts,

$$H_{\text{SET}} = H_{\text{dot}} + H_{\text{leads}} + H_{\text{tun}}, \quad (1.4)$$

where H_{dot} describes the quantum dot, H_{leads} the left (L) and right (R) leads, and H_{tun} the tunneling between leads and dot. Explicitly,

$$H_{\text{dot}} = (\epsilon_d - e\bar{V}_g) n_d + \frac{U}{2} n_d(n_d - 1), \quad (1.5)$$

with n_d the number of excess electrons on the quantum dot, $\bar{V}_g = C_g V_g / C_\Sigma$, with C_g and C_Σ the gate and total capacitances of the SET, respectively. The intra-dot Coulomb repulsion denoted by U is assumed to be constant, and in what follows, we consider it as the largest energy scale of the problem ($U \rightarrow \infty$) such that multiple occupancy of the dot is forbidden (strong Coulomb blockade regime). Hence, we write $n_d = d^\dagger d$, where d^\dagger (d) creates (annihilates) a single electron on the dot. In the following, we also set $\epsilon_d = 0$, measuring V_g from the degeneracy point. The left and right leads are assumed to be Fermi liquids at temperature T with chemical potentials μ_L and μ_R (measured from ϵ_d), respectively. A (symmetric) bias voltage V is applied to the junction such that $\mu_L = -\mu_R = eV/2$. The lead Hamiltonian reads

$$H_{\text{leads}} = \sum_{ka} (\epsilon_k - \mu_a) c_{ka}^\dagger c_{ka}, \quad (1.6)$$

with c_{ka} the annihilation operator for a spinless electron of momentum k in lead $a = \text{L, R}$. Finally, tunneling is accounted for by the Hamiltonian

$$H_{\text{tun}} = \sum_{ka} (t_a c_{ka}^\dagger d + \text{h.c.}), \quad (1.7)$$

with t_a the tunneling amplitude between the quantum dot and lead a , which is assumed to be energy-independent on the range of bias voltages considered in what follows.

As already mentioned in the introduction of the chapter, two different kinds of couplings exist between the electronic occupation of the dot n_d and the vibrational degrees of freedom: (i) an intrinsic one that originates from the variation of the electronic energy due to the elastic deformation of the beam [61] and (ii) an electrostatic one, induced by the capacitive coupling to the gate electrode of the SET [57, 63–65]. By symmetry, the former is quadratic in the amplitude X and its effect on the Euler instability will be considered in Sec. 1.3. The latter, which arises from the dependence of the gate capacitance on the deflection X of the nanoresonator (see, e.g., Ref. [41]), is in the limit of small deformation linear in X . Here we are interested in the case where the second coupling dominates over the first one. Their relative intensity is controlled by the distance h between the gate electrode and the beam, since the intrinsic coupling does not depend on h , while the electrostatic force depends logarithmically on h [63]. Assuming that the beam is sufficiently close to the gate electrode such that the capacitive coupling dominates, we can write

$$H_c = F_e X n_d, \quad (1.8)$$

where $-F_e$ is the force exerted on the tube when one excess electron occupies the quantum dot [see Fig. 1.1(c)]. The model assumes that the gate voltage is such that only charge states with $n_d = 0$ and 1 are accessible. For larger gate voltages overcoming the charging energy of the quantum dot, the charge on the dot will instead fluctuate between N and $N + 1$. This induces an additional constant force further bending the tube.²

1.2.2 Current-induced Langevin dynamics

As $\omega \rightarrow 0$ close to the buckling instability, the oscillator becomes classical ($\hbar\omega \ll k_B T$) and slow compared to the electronic degrees of freedom ($\omega \ll \Gamma$, with Γ the tunneling-induced width of the dot energy level). This justifies a nonequilibrium Born-Oppenheimer approximation [66–71], in which the vibrational dynamics is characterized by a Langevin process with white noise,

$$\frac{d^2 x}{d\tau^2} + [\gamma(x) + \gamma_e] \frac{dx}{d\tau} = f_{\text{eff}}(x) + \xi(x, \tau). \quad (1.9)$$

Here and in what follows, we use reduced units $x = X/\ell$, $p = P/m\omega_0\ell$ and $\tau = \omega_0 t$ in terms of the polaron shift $\ell = F_e/m\omega_0^2$ and the relevant energy scale of the problem $E_E^0 = F_e\ell$.

The explicit form of the coefficients entering into the Langevin equation (1.9) depends on the transport regime one considers (sequential or resonant transport), as well as on the nature of the quantum dot (metallic or semiconducting quantum dot). Here we consider the case of a single level in the sequential tunneling regime. To be specific, we assume that the dot-lead hybridization $\hbar\Gamma = \sum_{a=L,R} \Gamma_a \ll k_B T$ with $\Gamma_a = 2\pi|t_a|^2\nu/\hbar$ and ν the density of states at the Fermi level of the leads. The strong-coupling regime (or equivalently the low-temperature regime) $k_B T \ll \hbar\Gamma$ will be discussed in Sec. 1.2.5.

In Eq. (1.9), the effective reduced force (in units of F_e) acting on the nanobeam,

$$f_{\text{eff}}(x) = \delta x - \tilde{\alpha} x^3 - n_0(x), \quad (1.10)$$

with $\delta = F/F_c - 1$ and $\tilde{\alpha} = \alpha\ell^4/E_E^0$ arises (i) from the bare vibrational Hamiltonian (1.2) and (ii) from the coupling between vibrational and electronic degrees of freedom (1.8). This

² The effect of such a force on the classical current blockade is discussed in detail in Ref. [19].

current-induced force is proportional to the occupation of the dot for fixed x , which, in the sequential tunneling regime ($\hbar\Gamma \ll k_B T$) and for symmetric coupling to the leads ($\Gamma_L = \Gamma_R$), is given by

$$n_0(x) = \frac{1}{2} [f_L(x) + f_R(x)], \quad (1.11)$$

with

$$f_{L/R}(x) = \left[\exp\left(\frac{x - v_g \mp v/2}{\tilde{T}}\right) + 1 \right]^{-1} \quad (1.12)$$

the Fermi function in the left and right leads, respectively. Here we introduced a reduced bias voltage $v = eV/E_E^0$, gate voltage $v_g = (e\bar{V}_g - \epsilon_d)/E_E^0$, and temperature $\tilde{T} = k_B T/E_E^0$. The charge fluctuations on the quantum dot induce a fluctuating force $\xi(x, \tau)$ in the Langevin equation (1.9), with average $\langle \xi(x, \tau) \rangle = 0$ and white-noise correlator $\langle \xi(x, \tau) \xi(x, \tau') \rangle = [d(x) + 2\gamma_e \tilde{T}] \delta(\tau - \tau')$. Here, the current-induced fluctuation is given by [19, 53]

$$d(x) = \frac{2\omega_0}{\Gamma} n_0(x) [1 - n_0(x)], \quad (1.13)$$

and the extrinsic damping constant γ_e accounts for the finite quality factor $Q = 1/\gamma_e$ of the nanoresonator. Finally, retardation effects in the response of the resonator to the current flow lead to a current-induced dissipative force with friction coefficient [19, 53]

$$\gamma(x) = -\frac{\omega_0}{\Gamma} \frac{\partial}{\partial x} n_0(x). \quad (1.14)$$

The Langevin equation (1.9) is equivalent to the Fokker-Planck equation [72]

$$\frac{\partial}{\partial \tau} \mathcal{P}(x, p, \tau) = \mathcal{L} \mathcal{P}(x, p, \tau) \quad (1.15)$$

for the probability distribution $\mathcal{P}(x, p, \tau)$ that the nanobeam is at phase-space point (x, p) at time τ . In Eq. (1.15), the Fokker-Planck operator is defined as

$$\mathcal{L} = -p \frac{\partial}{\partial x} - f_{\text{eff}}(x) \frac{\partial}{\partial p} + [\gamma(x) + \gamma_e] \frac{\partial}{\partial p} p + \left[\frac{d(x)}{2} + \gamma_e \tilde{T} \right] \frac{\partial^2}{\partial p^2}. \quad (1.16)$$

Solving the Fokker-Planck equation (1.15) [or equivalently the Langevin equation (1.9)] gives access to both the dynamics of the vibrational mode of the nanoresonator and the resulting transport properties of the device, such as its I - V characteristics (see Sec. 1.2.3) and its noise power spectrum (see Sec. 1.2.4).

1.2.3 Current blockade

Due to the separation of timescales between slow vibrational motion and fast electronic dynamics, the average current

$$I = \int dx dp \mathcal{P}_{\text{st}}(x, p) \mathcal{I}(x) \quad (1.17)$$

is obtained by averaging the quasistationary current

$$\mathcal{I}(x) = \frac{e\Gamma}{4} [f_L(x) - f_R(x)] \quad (1.18)$$

for fixed deflection x over the stationary solution \mathcal{P}_{st} of the Fokker-Planck equation (1.15).

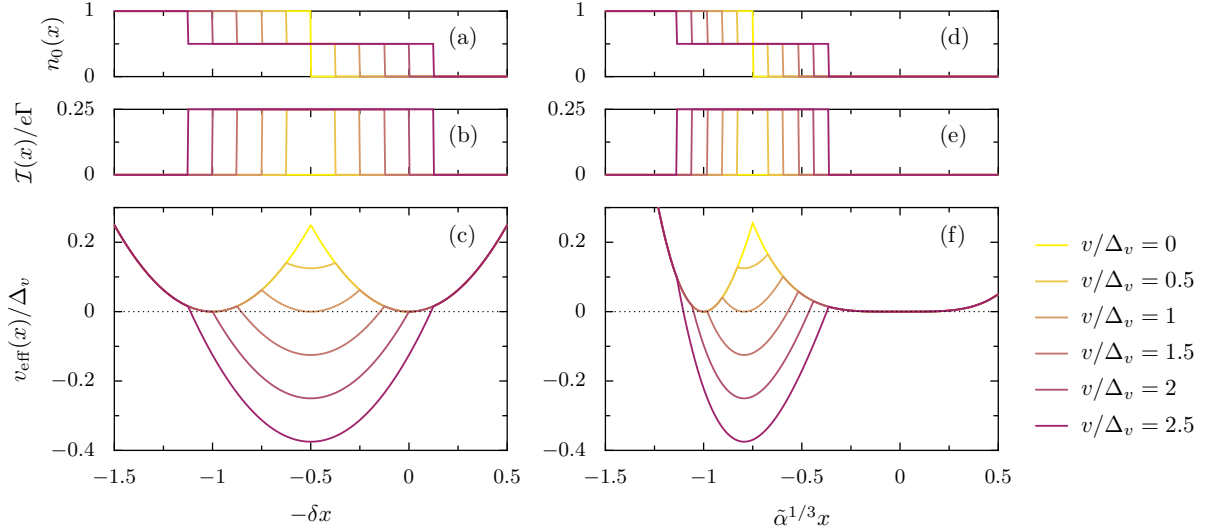


Figure 1.3: Zero temperature (a),(d) average occupation of the dot for fixed x [Eq. (1.11)], (b),(e) quasistationary current [Eq. (1.18)] and (c),(f) effective potential [Eq. (1.19)], (a)–(c) far below the Euler instability ($-\delta \gg \tilde{\alpha}^{1/3}$) and (d)–(f) at the instability ($\delta = 0$) for increasing bias voltages and for a gate voltage $v_g = v_g^{\min}$ [cf. Eq. (1.22)].

Mean-field treatment

It is instructive to start our analysis by neglecting the current-induced fluctuations and dissipation in the Langevin equation (1.9) [extreme adiabatic limit $\omega_0/\Gamma \rightarrow 0$, cf. Eqs. (1.13) and (1.14)]. We further neglect the temperature-induced fluctuations, hence restricting ourselves to a mean-field treatment of the problem.

Within this approximation, the classical current blockade phenomenon [19, 53] can be understood in terms of the effective potential

$$v_{\text{eff}}(x) = -\frac{\delta x^2}{2} + \frac{\tilde{\alpha} x^4}{4} + x + \frac{\tilde{T}}{2} \ln(f_L(x)f_R(x)) \quad (1.19)$$

associated to the effective force (1.10). The effective potential is shown in Fig. 1.3 for $\tilde{T} = 0$ together with the average occupation of the dot (1.11) and the quasistationary current (1.18) for compression forces corresponding to the beam far below [Figs. 1.3(a)–(c)] and at the Euler instability [Figs. 1.3(d)–(f)]. In both cases, the most stable minima of $v_{\text{eff}}(x)$ correspond, for bias voltages v smaller than the gap [19]

$$\Delta_v = \begin{cases} -\frac{1}{2\delta}, & -\delta \gg \tilde{\alpha}^{1/3}, \\ \frac{1}{4\delta}, & \delta \gg \tilde{\alpha}^{1/3}, \\ \frac{2^{1/3} - 1}{\tilde{\alpha}^{1/3}} \left(\frac{3}{2^{4/3}} - \frac{\delta}{\tilde{\alpha}^{1/3}} \right), & |\delta| \ll \tilde{\alpha}^{1/3}, \end{cases} \quad (1.20)$$

which corresponds to the apex of the Coulomb diamond, to an average occupation $n_0(x) = 0$ or 1, i.e., the system is not conducting [“blocked” minima for which $\mathcal{I}(x) = 0$, cf. Figs. 1.3(b),(e)].

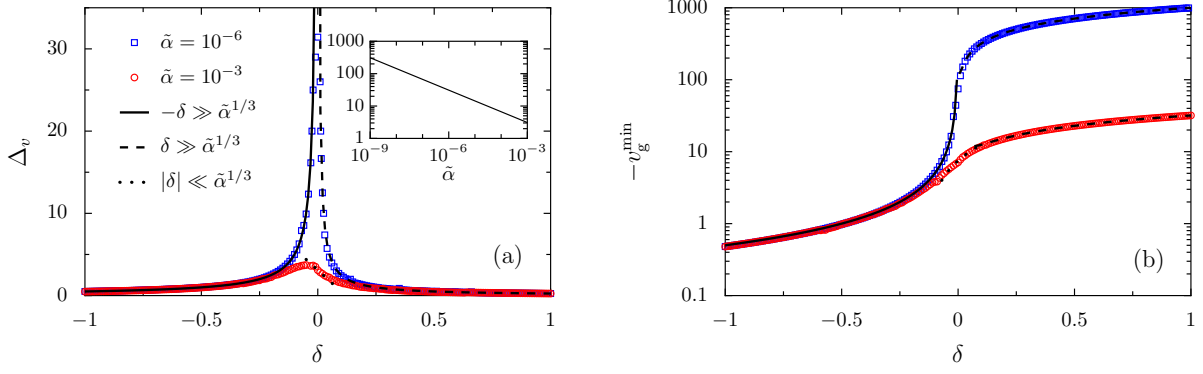


Figure 1.4: (a) Gap Δ_v and (b) gate voltage v_g^{\min} (defined as the bias and gate voltages in reduced units at the apex of the Coulomb diamond, respectively) as a function of the scaled compression force $\delta = F/F_c - 1$. The red circles and blue squares are numerical results for $\tilde{\alpha} = 10^{-3}$ and 10^{-6} , respectively, which are compared to the asymptotic behaviors (1.20) and (1.22) for forces below (solid line), above (dashed line), and in the vicinity (dotted line) of the critical force F_c . Inset: Gap $\Delta_v \sim 1/\tilde{\alpha}^{1/3}$ from Eq. (1.20) as a function of $\tilde{\alpha}$ at the mechanical instability ($\delta = 0$).

For $v > \Delta_v$, the most stable minimum corresponds to $n_0(x) = 1/2$ and the current can flow [“conducting” minimum corresponding to $\mathcal{I}(x) \neq 0$]. At the threshold $v = \Delta_v$, the three minima are metastable, leading to a current-induced instability of the system. Notice that the asymptotic results of Eq. (1.20) are obtained by solving the dynamical equilibrium condition

$$f_{\text{eff}}(x) = 0, \quad \frac{df_{\text{eff}}(x)}{dx} < 0, \quad (1.21)$$

in the limiting cases where the nanoresonator lies well below (above) the Euler buckling instability, i.e., $-\delta \gg \tilde{\alpha}^{1/3}$ ($\delta \gg \tilde{\alpha}^{1/3}$), or in the vicinity of the mechanical instability ($|\delta| \ll \tilde{\alpha}^{1/3}$).

The asymptotic analytical results of Eq. (1.20) are compared to a numerical calculation of the gap in Fig. 1.4(a) for $\tilde{\alpha} = 10^{-3}$ and $\tilde{\alpha} = 10^{-6}$ (red dots and blue squares in the figure, respectively). The latter is obtained by searching numerically the local minima of the effective potential (1.19). It is evident from the figure that there is a dramatic increase of the gap close to the instability. Furthermore, the smaller $\tilde{\alpha}$, i.e., the smaller the electromechanical coupling, the larger is the increase of the gap at the instability relative to its value for vanishing compression force [see the inset in Fig. 1.4(a)]. However, of course, the maximal value of the gap in absolute terms increases with the strength of the electromechanical coupling as $F_e^{4/3}$. It would thus be of great experimental interest to exploit the Euler instability to obtain a clear signature of the classical current blockade in transport experiments on suspended quantum dots.

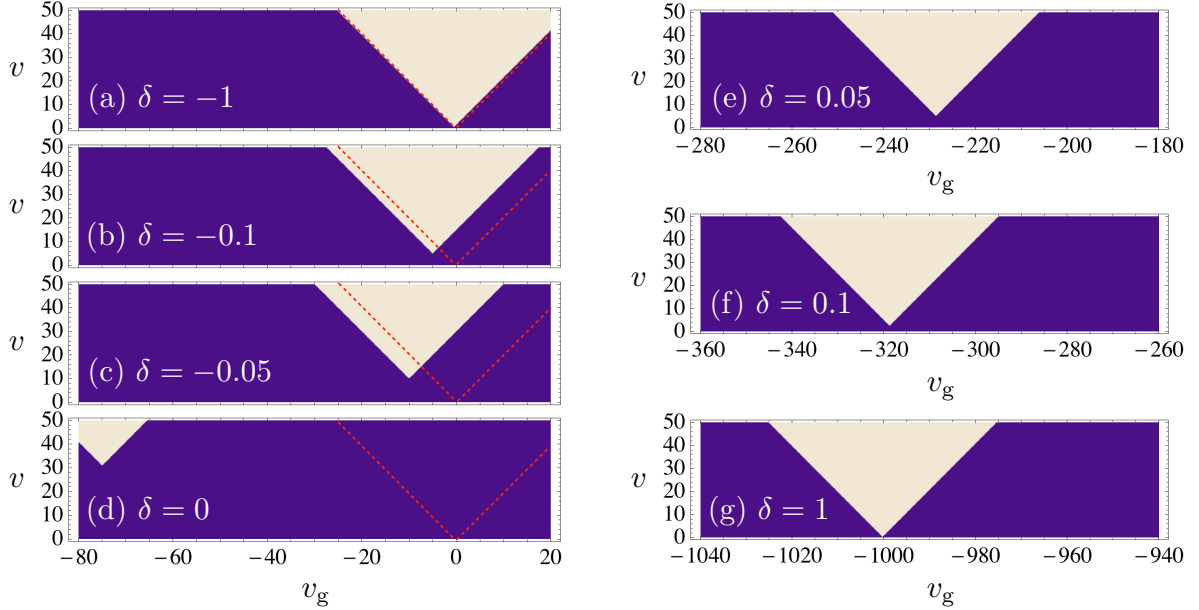


Figure 1.5: Mean-field current I at zero temperature and for symmetric coupling to the leads ($\Gamma_L = \Gamma_R = \Gamma/2$), as a function of bias v and gate voltage v_g (measured in units of the elastic energy E_E^0). The (scaled) compression force δ increases from (a) to (g). Notice that the scale of the v_g -axis is different in (e), (f), and (g), and in (a)–(d). The red dashed lines indicate the position of the Coulomb diamond in the absence of electromechanical coupling ($F_e = 0$). In the figure, $\tilde{\alpha} = 10^{-6}$, and dark blue and white regions correspond to $I = 0$ and $I = e\Gamma/4$, respectively.

The gaps of Eq. (1.20) are obtained for gate voltages $v_g = v_g^{\min}$, with [19]

$$v_g^{\min} = \begin{cases} \frac{1}{2\delta}, & -\delta \gg \tilde{\alpha}^{1/3}, \\ -\frac{1}{4\delta} - \sqrt{\frac{\delta}{\tilde{\alpha}}}, & \delta \gg \tilde{\alpha}^{1/3}, \\ -\frac{1}{4\tilde{\alpha}^{1/3}} \left(3 + \frac{2\delta}{\tilde{\alpha}^{1/3}} \right), & |\delta| \ll \tilde{\alpha}^{1/3}, \end{cases} \quad (1.22)$$

which are shown in Fig. 1.4(b) and compared to a numerical calculation. Equations (1.20) and (1.22) define the apexes of the Coulomb diamonds which are shown in Fig. 1.5.

The effect of the compression force is thus to continuously displace the Coulomb diamond in the v - v_g plane towards negative gate voltages [see also Fig. 1.4(b)], and to open a gap which is maximal close to the Euler instability at $\delta = 0$ [see Fig. 1.5(d)]. Note that the shift in gate voltage is strongly asymmetric around the Euler instability. While the shifts are only small below the Euler instability [see Figs. 1.5(a)–(c) and Fig. 1.4(b)], the shifts in gate voltage are orders of magnitude larger on the buckled side of the Euler instability [see Figs. 1.5(e)–(g) and Fig. 1.4(b)]. In fact, it may be that these shifts are the most easily detectable consequence of the Euler buckling instability in NEMS. In Fig. 1.5, the bias and gate voltages are measured in units of the elastic energy E_E^0 which is of the order of a few μeV for typical experiments

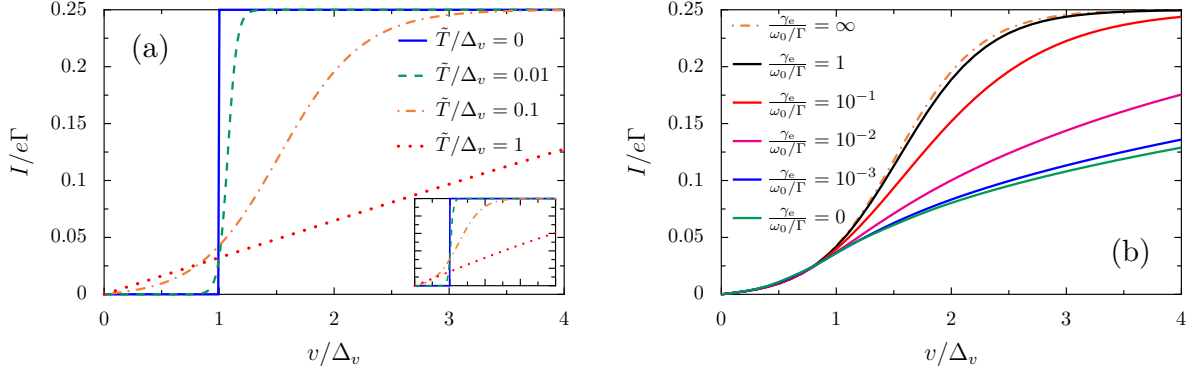


Figure 1.6: (a) Current I at the apex of the Coulomb diamond as a function of bias v scaled by the energy gap Δ_v for various values of \tilde{T}/Δ_v , and for compression forces in the vicinity of the buckling instability ($|\delta| \ll \sqrt[3]{\tilde{\alpha}}$). In the figure, only the temperature-induced fluctuations are considered. Inset: Same as the main figure for compression forces far from the buckling instability ($|\delta| \gg \sqrt[3]{\tilde{\alpha}}$). (b) Current I at the apex of the Coulomb diamond for $\delta = 0$ as a function of v/Δ_v for $\tilde{\alpha} = 10^{-6}$ and $\tilde{T}/\Delta_v = 0.1$. In our numerical calculations, we used $\omega_0/\Gamma = 10^{-2}$.

on suspended carbon nanotubes [41, 42]. The smallness of this energy scale explains why the scaled numerical values of the shifts become so large on the buckled side of the Euler instability.

Thermal and current-induced fluctuations

We now go beyond the mean-field results of the previous section by taking into account the effects of the thermal as well as the current-induced fluctuations. It is physically clear that these fluctuations will lead to a smoothing of the current blockade at low bias voltages, as the system can explore more conducting states in phase space.

Temperature effects – We first neglect the current-induced fluctuations and focus on thermal fluctuations only. This becomes asymptotically exact in the extreme adiabatic limit of $\omega_0/\Gamma \rightarrow 0$, where the terms $\gamma(x)$ and $d(x)$ can be dropped from the Fokker-Planck equation (1.15). The stationary solution for \mathcal{P} is then given by a Boltzmann distribution at the (reduced) temperature \tilde{T} corresponding to the effective potential (1.19). The current can then be easily calculated by numerical integration of Eq. (1.17). The result is shown in Fig. 1.6(a) as a function of the bias voltage, for gate voltages corresponding to the apex of the modified zero-temperature Coulomb diamond [cf. Eq. (1.22)]. Once plotted as a function of v/Δ_v , one finds that the current behavior is similar at the transition [Fig. 1.6(a)] and far from the transition [inset of Fig. 1.6(a)]. In both cases, the low-bias blockade of the current becomes less pronounced as temperature increases, and vanishes completely for temperatures of the order of the gap Δ_v . As shown in Ref. [19], the current has a Fermi-function-like behavior as a function of the bias voltage for temperatures much smaller than the energy gap Δ_v [see dashed and dashed-dotted lines in Fig. 1.6(a)]. It is thus exponentially suppressed for bias voltage below the gap. At larger temperatures, the current is linear in the bias voltage [see dotted line in Fig. 1.6(a)]. Our numerical and analytical results [19] thus confirm that tuning the system near the buckling instability where Δ_v dramatically increases allows one to enlarge the temperature

region over which the current blockade is observable.

Nonequilibrium dynamics – We now consider the non-equilibrium Langevin dynamics of the nanobeam by solving the full Fokker-Planck equation (1.15). This is done by discretization of the Fokker-Planck equation and solution of the resulting linear system. We focus on the transition region ($\delta = 0$) and calculate the current for v_g at the apex of the Coulomb diamond [see Eq. (1.22) and Fig. 1.4(b)] and temperature lower than the gap $\tilde{T}/\Delta_v = 0.1$. Before we present our results, we notice that for $(\omega_0/\Gamma, \gamma_e) \ll 1$, we can show that the stationary distribution of the Fokker-Planck equation only depends on the ratio $\frac{\gamma_e}{\omega_0/\Gamma}$, a result we have also checked numerically [19].

Numerical results for the current are shown in Fig. 1.6(b) for various ratios of the inverse quality factor $Q^{-1} = \gamma_e$ as quantified by the damping coefficient γ_e and the adiabaticity parameter ω_0/Γ . Our principal observation is that the current blockade becomes sharper for low- Q resonators.

One can qualitatively understand the behavior of the current in Fig. 1.6(b) by defining an effective temperature of the system

$$\tilde{T}_{\text{eff}} = \frac{\langle d \rangle / 2 + \gamma_e \tilde{T}}{\langle \gamma \rangle + \gamma_e} \quad (1.23)$$

in close analogy with the fluctuation-dissipation theorem [72]. In Eq. (1.23), $\langle d \rangle$ and $\langle \gamma \rangle$ are the averages over the phase-space probability distribution of the current-induced fluctuations and dissipation [cf. Eqs. (1.13) and (1.14)], respectively. Notice that the strength of these two quantities is controlled by the adiabaticity parameter ω_0/Γ . In the limit $\langle \gamma \rangle \ll \gamma_e$, we find [19]

$$\tilde{T}_{\text{eff}} \simeq \tilde{T} + \frac{\omega_0/\Gamma}{4\gamma_e} \Theta(v - \Delta_v). \quad (1.24)$$

Hence, for $v < \Delta_v$, the current-induced fluctuations behave like the thermal ones, essentially keeping the system at thermal equilibrium in a state for which the current is suppressed. For $v > \Delta_v$, the estimate (1.24) of the effective temperature shows that the system becomes “hotter” as the ratio $\frac{\gamma_e}{\omega_0/\Gamma}$ decreases. Hence, the system can explore more states in phase space for which $\mathcal{I}(x)$ is suppressed, and, in turn, the current decreases for decreasing $\frac{\gamma_e}{\omega_0/\Gamma}$ for $v > \Delta_v$ [see Fig. 1.6(b)]. The latter argument breaks down when $\gamma_e \ll \langle \gamma \rangle$. In that case, we estimate [19] that $\tilde{T}_{\text{eff}}/\Delta_v \sim (v/\Delta_v)^2 / \ln(v/\Delta_v) \gg \tilde{T}/\Delta_v$, which explains why for $\gamma_e = 0$ the current is more suppressed than for finite γ_e .

Our results show that a low quality factor is more suitable for the observation of the current blockade in classical resonators. It is interesting to note that this conclusion is also valid in the quantum case [55, 56], where the Franck-Condon blockade is more pronounced for fast equilibration of the vibron mode. Due to the scaling of our results for the classical current blockade with the parameter $\frac{\gamma_e}{\omega_0/\Gamma}$ [see Fig. 1.6(b)], we also conclude that it is advantageous for the observation of this phenomenon to have a resonator which is slow compared to the tunneling dynamics, i.e., $\omega_0 \ll \Gamma$.

Experimental realization

The electromechanical coupling (1.8) is typically weak in experiments. For this reason, only a precursor of the classical current blockade has been seen in two recent experiments on suspended carbon nanotube quantum dots [41, 42], but the full current blockade has not yet been observed.

We estimate that for the suspended carbon nanotubes of Ref. [41], the energy scale below which current is blocked in absence of any compression force is of the order of $E_E^0 \simeq 3\text{--}5 \mu\text{eV}$, while for those of Ref. [42], we get $E_E^0 \simeq 20 \mu\text{eV}$ [19].

We now use these numbers to estimate the possible enhancement of the current blockade near the Euler buckling instability. Based on Eq. (1.20), the parameters extracted from the experimental data [41, 42] yield a possible increase of the mechanically-induced gap by three orders of magnitude, leading to a maximal Δ_v (converted into a dimensionful quantity using the energy scale E_E^0) of the order of 3 to 5 meV. Such large gaps would be much more easily observable in experiment.

The implementation of our proposal could be performed by the method routinely employed to control break junctions through a force pushing the substrate of the device. An important point to investigate towards its experimental realization is the noise level, which can be particularly large in the vicinity of the mechanical instability. This is the purpose of the next section.

1.2.4 Large current noise

In this section we investigate the current noise in the vicinity of a mechanical instability, using the Euler buckling instability as a paradigmatic model. We find that the current noise (which contains valuable information about the dynamics of the nanomechanical system [66, 73–78]) is strongly enhanced in the vicinity of the Euler instability. The underlying source of noise arises from the stochastic nature of the charge transfer processes. These are producing current-induced stochastic forces acting on the mechanical degrees of freedom, so that the deflection of the nanotube exhibits a Langevin dynamics described by Eq. (1.9) which, due to the backaction of the nanoresonator on the SET, produces large super-Poissonian current noise [54, 66, 73, 75–78]. This effect is particularly strong close to the Euler buckling instability, where the nanoresonator becomes extremely soft ($k \rightarrow 0$).

In the following, we will first present our numerical results for the noise based on the Fokker-Planck equation (1.15). We will then study in detail the role played by thermal fluctuations on the current noise and propose an analytical model based on telegraph noise that reproduces most of our numerical findings. The role played by the full nonequilibrium fluctuations will finally be discussed.

Current noise at the Euler buckling instability

We start by discussing the two contributions to the current noise, i.e., the usual shot noise and the mechanically-induced noise. It is the latter contribution to the noise which we find to be dramatically enhanced close to the mechanical instability.

The noise power spectrum is defined as [79]

$$S(\Omega) = 2 \int_{-\infty}^{+\infty} dt e^{i\Omega t} \langle \Delta \hat{I}(t_0 + t) \Delta \hat{I}(t_0) \rangle, \quad (1.25)$$

where $\Delta \hat{I}(t) = \hat{I}(t) - \langle \hat{I} \rangle$ denotes the time-dependent fluctuations of the current operator. In Eq. (1.25), the brackets $\langle \dots \rangle$ indicate an ensemble average or, equivalently, an average over the initial time t_0 . Due to the separation of timescales between fast electronic dynamics and slow vibrational motion ($\omega \ll \Gamma$), one can identify two additive contributions to the noise power spectrum (1.25), $S = S_{\text{sh}} + S_{\text{m}}$ [54, 66, 67, 78]. The first one, S_{sh} , corresponds to the (thermal) Nyquist-Johnson and shot noise. The second contribution to Eq. (1.25), the

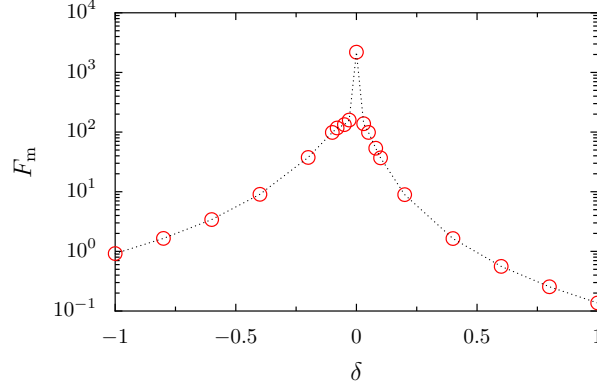


Figure 1.7: Fano factor as a function of the reduced compression force $\delta = F/F_c - 1$. In the figure, $\gamma_e = \omega_0/\Gamma = 10^{-2}$, $\tilde{T} = 3$, $\tilde{\alpha} = 10^{-6}$, $v = \Delta_v$ and $v_g = v_g^{\min}$. The red circles correspond to the data points, while the dotted line serves as a guide to the eye.

mechanically-induced noise S_m (referred to as “mechanical noise” in the sequel), is induced by the fluctuations of the nanobeam deflection $x(t)$. These occur on a much longer timescale (of the order of $1/\omega$) than the shot noise (the corresponding current-current correlator decaying in that case on the short timescale $1/\Gamma$). The mechanically-induced noise therefore dominates the noise power spectrum at low frequencies, and can exceed the shot noise by orders of magnitude [54, 66, 67, 78].

The mechanical noise reads

$$S_m(\Omega) = 2 \int \frac{d\tau}{\omega_0} e^{i\Omega\tau/\omega_0} \int dx dp dx_0 dp_0 \Delta\mathcal{I}(x)\mathcal{P}(x, p, \tau|x_0, p_0, \tau_0)\Delta\mathcal{I}(x_0)\mathcal{P}_{\text{st}}(x_0, p_0) \quad (1.26)$$

where $\mathcal{P}(x, p, \tau|x_0, p_0, \tau_0)$ is the conditional probability that the nanobeam is at phase-space point (x, p) at time τ , provided it was at (x_0, p_0) at time $\tau_0 \equiv 0$. In Eq. (1.26), $\Delta\mathcal{I}(x) = \mathcal{I}(x) - I$ is the quasistationary current fluctuation, with $\mathcal{I}(x)$ and I given by Eqs. (1.18) and (1.17), respectively. The conditional probability $\mathcal{P}(x, p, \tau|x_0, p_0, \tau_0)$ can be obtained from the time-dependent solution of the Fokker-Planck equation (1.15) with the initial condition $\mathcal{P}(x, p, \tau_0|x_0, p_0, \tau_0) = \delta(x-x_0)\delta(p-p_0)$. Equation (1.26) can then be re-expressed by exploiting the above initial condition and performing the Laplace transform of the Fokker-Planck equation (1.15). This procedure yields [54]

$$S_m(\Omega) = -\frac{4}{\omega_0} \int dx dp \Delta\mathcal{I}(x) \left[\mathcal{L}^2 + \left(\frac{\Omega}{\omega_0} \right)^2 \right]^{-1} \mathcal{L} [\Delta\mathcal{I}(x)\mathcal{P}_{\text{st}}(x, p)], \quad (1.27)$$

with \mathcal{L} the Fokker-Planck operator defined in Eq. (1.16). In the form of Eq. (1.27), the mechanical noise can be straightforwardly computed numerically, since it only requires the knowledge of the stationary probability distribution \mathcal{P}_{st} corresponding to the Fokker-Planck equation (1.15), as it is the case for the average current (1.17).

In Fig. 1.7, we present our numerical results for the Fano factor $F_m = S_m(0)/2e|I|$, where the zero-frequency noise $S_m(0)$ and the average current I , Eqs. (1.27) and (1.17), respectively, are computed for typical parameters as a function of the reduced force δ . In Fig. 1.7, the bias and gate voltages correspond to the apex of the Coulomb diamond [$v = \Delta_v$ and $v_g = v_g^{\min}$, cf.

Eqs. (1.20) and (1.22), respectively]. As envisioned above, there is a dramatic increase of the mechanically-induced current noise in the vicinity of the Euler buckling instability ($\delta \approx 0$ in Fig. 1.7) as compared to the noise far away from the instability. Moreover, the Fano factor can take, depending on the compression force δ , super-Poissonian values ($F_m > 1$) that are well above the shot noise contribution, $F_{\text{sh}} = 1/2$ [21].

The results of Fig. 1.7 can essentially be understood in terms of telegraph noise in the effective potential (1.19) (see also Fig. 1.3). Indeed, unlike the energy gap (1.20) which varies algebraically with the force δ as $\sim 1/|\delta|$, the numerical results of Fig. 1.7 indicate that the noise (or Fano factor) depends *exponentially* on $1/|\delta|$ (notice the logarithmic scale in Fig. 1.7), suggesting telegraph noise. As the compression force increases towards the instability at $\delta = 0$, the height of the barriers separating the three metastable minima (for $v = \Delta_v$) grows as the gap (1.20), such that the waiting time of the system in one of these minima increases exponentially. Thus, the probability for the system to switch to another minimum is drastically reduced, subsequently increasing the telegraph noise. As the height of the potential barriers near the Euler instability is very large, scaling as $1/\tilde{\alpha}^{1/3}$ with $\tilde{\alpha} \ll 1$ [see Fig. 1.3(f)], and the energy gap (1.20) is maximal at the instability, this leads to a current noise which is also maximal at the Euler instability.

This interpretation is confirmed by Fig. 1.8, which shows the result of a simulation [80] of the deflection of the nanobeam x as a function of time (see blue lines in the figure) as obtained from the Langevin equation (1.9) for the same parameters as in Fig. 1.7. We also show the resulting quasistationary current (1.18) as a function of time by red lines in Fig. 1.8. Far from the instability [Figs. 1.8(a) and 1.8(e)], the dynamics of the nanobeam follows qualitatively the behavior of a Brownian particle in a harmonic potential. Indeed, for the temperature used in Figs. 1.7 and 1.8, the effective potential (1.19) far from the instability has a single minimum [21]. For temperatures \tilde{T} which are large compared to the gap (1.20), the current shown in Figs. 1.8(a) and 1.8(e) switches rapidly between values which are small as compared to the maximal current $e\Gamma/4$. Hence, the resulting Fano factor is relatively small (cf. Fig. 1.7). As one approaches the Euler instability from below [Fig. 1.8(b)] or above [Fig. 1.8(d)], the dynamics of the nanobeam becomes slower. Then the behavior of the current as a function of time starts to resemble telegraph noise, as the effective potential starts developing metastable minima for this value of the temperature as compared to the energy gap (1.20). At the instability [Fig. 1.8(c)], the dynamics of the nanobeam becomes very slow, and the behavior of the current as a function of time is completely stochastic and uncorrelated, with long waiting times between vanishing and maximal current. The corresponding Fano factor is thus extremely large and super-Poissonian ($F_m > 10^3$ in Fig. 1.7), and much larger than far from the Euler instability.

In order to understand the features of our main numerical results presented in Figs. 1.7 and 1.8 in more detail, we will first consider in the next paragraph the role played by thermal fluctuations alone.

Telegraph noise

We consider here the fully adiabatic limit $\omega_0/\Gamma \rightarrow 0$. We neglect the current-induced fluctuations and dissipation in the Fokker-Planck equation (1.15) [cf. Eqs. (1.13) and (1.14)] and consider the role played by thermal fluctuations alone. We present a simplified analytical model based on standard telegraph noise, that was substantiated by numerical calculations based on Eq. (1.27) [21]. Our simplified model relies on thermally-induced telegraph noise [81] and on

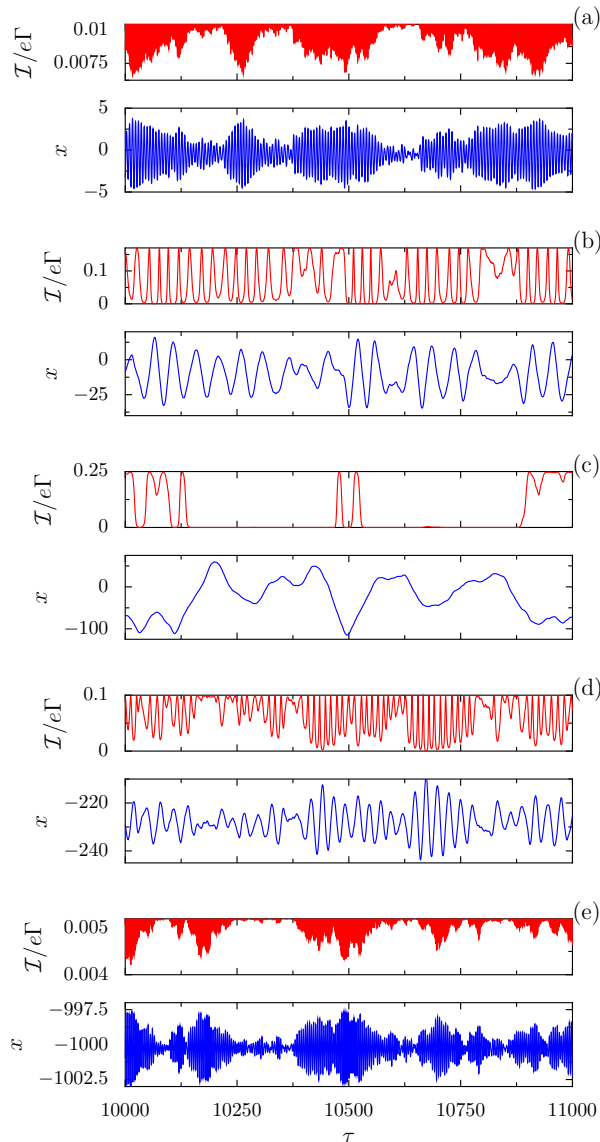


Figure 1.8: Deflection x (in blue) and quasistationary current \mathcal{I} (in red) as a function of time simulated by the Langevin equation (1.9). In the figure, the compression force increases from (a) to (e): (a) $\delta = -1$, (b) $\delta = -0.05$, (c) $\delta = 0$, (d) $\delta = 0.05$, and (e) $\delta = 1$. The parameters used in the figure are the same as in Fig. 1.7.

an estimate of the escape rates based on Kramers reaction rate theory [72, 82, 83].

In what follows, we work in the low-temperature regime $\tilde{T} \ll \Delta_v$, with the gap Δ_v given in Eq. (1.20). Moreover, we focus on the case where the nanobeam is far below the Euler instability ($-\delta \gg \tilde{\alpha}^{1/3}$), as the results presented below should stay qualitatively the same for larger compression forces. We thus approximate the effective potential (1.19) by its zero-temperature counterpart, which is shown in Fig. 1.3(c) for a gate voltage $v_g = v_g^{\min}$ [cf. Eq. (1.22)]. As one can see from Fig. 1.3(c), the effective potential has three metastable minima for $0 < v < 2\Delta_v$: two of them are equivalent (located symmetrically at $x_1 = 1/\delta$ and $x_0 = 0$ about

the line $x = 1/2\delta$) and correspond to a state in which the current vanishes [see Fig. 1.3(b)], while the one at $x_{1/2} = 1/2\delta$ corresponds to a current-carrying state. This suggests to write a rate equation for the probabilities P_c and P_b that the system is in a conducting or blocked state, respectively. Denoting $\Gamma_{\text{in}} = (\Gamma_{x_0 \rightarrow x_{1/2}} + \Gamma_{x_1 \rightarrow x_{1/2}})/2$ and $\Gamma_{\text{out}} = \Gamma_{x_{1/2} \rightarrow x_1} + \Gamma_{x_{1/2} \rightarrow x_0}$ the transition rates in and out of the conducting state ($\Gamma_{x_i \rightarrow x_j}$ is here the transition rate from the minimum located at x_i to the one at x_j), we have $\dot{P}_c = -\dot{P}_b = -\Gamma_{\text{out}}P_c + \Gamma_{\text{in}}P_b$. Following Ref. [81], the average current and the noise power spectrum are readily obtained from the above rate equation. They read

$$I = \frac{e\Gamma}{4} \frac{\Gamma_{\text{in}}}{\Gamma_{\text{in}} + \Gamma_{\text{out}}} \quad (1.28)$$

and

$$S_m(\Omega) = \frac{e^2\Gamma^2}{4} \frac{\Gamma_{\text{in}}\Gamma_{\text{out}}}{\Gamma_{\text{in}} + \Gamma_{\text{out}}} \frac{1}{\Omega^2 + (\Gamma_{\text{in}} + \Gamma_{\text{out}})^2}, \quad (1.29)$$

respectively. Notice that for bias voltages $v \geq 2\Delta_v$, the effective potential (1.19) has a single minimum [see Fig. 1.3(c)], and the telegraph noise model presented above does not apply. Instead, the system's dynamics is characterized in that case by standard Brownian noise.

The transition rates entering Eqs. (1.28) and (1.29) can be easily calculated using Kramers theory [72, 82, 83], yielding approximate analytical forms for the average current and noise [21]. At a bias voltage corresponding to the energy gap (1.20) ($v = \Delta_v$), these results yield the Fano factor

$$F_m = \frac{16\Gamma}{3\omega_0} \gamma_e^{-1} \frac{\tilde{T}}{\Delta_v} \exp\left(\frac{\Delta_v}{16\tilde{T}}\right). \quad (1.30)$$

Although this result is based on a simplified model and despite the fact that it does not include the full nonequilibrium dynamics of the nanoresonator induced by the charge fluctuations on the dot, it qualitatively captures our main finding depicted in Fig. 1.7. Indeed, as one approaches the Euler instability from below, the gap Δ_v increases algebraically as $\sim 1/|\delta|$ [cf. Eq. (1.20)], resulting in an exponential increase of the Fano factor.

The result of Eq. (1.30) also applies for compression forces far above the Euler instability ($\delta \gg \tilde{\alpha}^{1/3}$). Since the energy gap Δ_v is, in that case, half of the gap far below the instability [$-\delta \gg \tilde{\alpha}^{1/3}$, cf. Eq. (1.20)], this explains the asymmetry of the Fano factor for negative and positive δ in Fig. 1.7. In the vicinity of the buckling instability ($|\delta| \ll \tilde{\alpha}^{1/3}$), the exponential dependence of the Fano factor as a function of the gap (1.20) (which here scales with $\tilde{\alpha} \ll 1$ as $1/\tilde{\alpha}^{1/3}$) should stay qualitatively the same. This results in a Fano factor which saturates at its maximal value at the Euler instability (cf. Fig. 1.7).

The analytical results [21] for the average current and the zero-frequency noise are shown in Figs. 1.9(a) and 1.9(b), respectively. As one can see from Fig. 1.9(b), our analytical results capture the following trends for the mechanical noise: (i) it only depends on the compression force δ through the ratio \tilde{T}/Δ_v , (ii) the noise is maximal close to $v = \Delta_v$ and its maximum shifts towards higher bias voltages when one increases the temperature, and (iii) the noise is inversely proportional to the extrinsic damping constant (i.e., proportional to the quality factor). All of these features based on our simplified telegraph-noise model were confirmed in Ref. [21] by means of numerical calculations based on Eq. (1.27). Moreover, we have checked numerically that the frequency dependence of the noise shows a $1/f^2$ dependence, typical of telegraph noise [cf. Eq. (1.29)], thus confirming the appropriateness of such a model to capture the underlying physics.

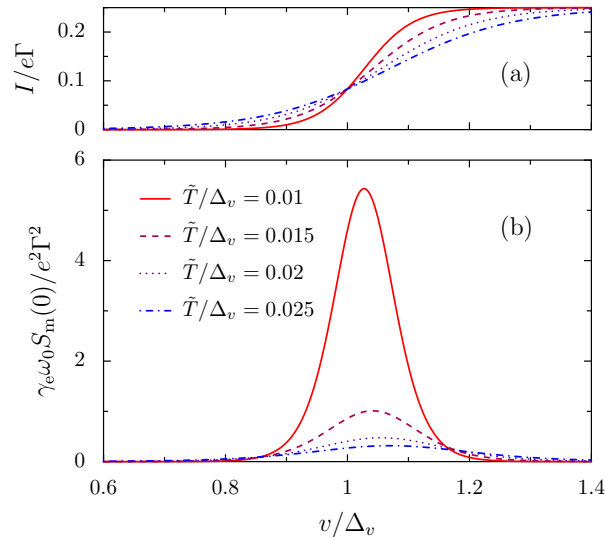


Figure 1.9: (a) Current and (b) zero-frequency noise from the analytical telegraph noise model as a function of bias voltage for increasing temperature.

Nonequilibrium fluctuations

We now investigate the mechanical noise in the presence of the current-induced fluctuations and dissipation, Eqs. (1.13) and (1.14). Our numerical results for the current and the zero-frequency noise are shown in Figs. 1.10(a) and 1.10(b), respectively, when the nanobeam is at the Euler instability (the insets in Fig. 1.10 consider the case $\delta = -1$). As one can see from Fig. 1.10, the effect of an increasing adiabaticity parameter ω_0/Γ , which controls the strength of the current-induced fluctuations (1.13) and dissipation (1.14), is qualitatively similar to the effect of an increasing temperature (cf. Fig. 1.9). Indeed, the overall noise level is reduced and the maximum of the noise is shifted towards larger bias voltages for increasing ω_0/Γ [see Fig. 1.10(b)]. Moreover, the current blockade gets less pronounced for increasing ω_0/Γ [see Fig. 1.10(a)].

The results of Fig. 1.10 can be qualitatively understood in terms of the effective temperature (1.23). The estimate (1.24) explains why both the current and the zero-frequency noise are quite insensitive to the ratio ω_0/Γ for $v < \Delta_v$ and are similar to the case $\omega_0/\Gamma = 0$, i.e., the fully adiabatic limit. On the contrary, for $v > \Delta_v$, the effective temperature increases with increasing ω_0/Γ , explaining the similarity of the behavior of the current and noise in Figs. 1.10 and 1.9.

We have numerically checked that the frequency dependence of the noise power spectrum also follows a $1/f^2$ behavior when one takes into account current-induced fluctuations. This confirms that the noise is dominated by a telegraph noise at low-enough temperatures even in presence of nonequilibrium fluctuations.

1.2.5 Role of cotunneling on the current blockade

The results of Sec. 1.2.3 where the enhancement of the current blockade at the Euler instability was predicted were obtained in the sequential-tunneling regime of weak coupling to the electron

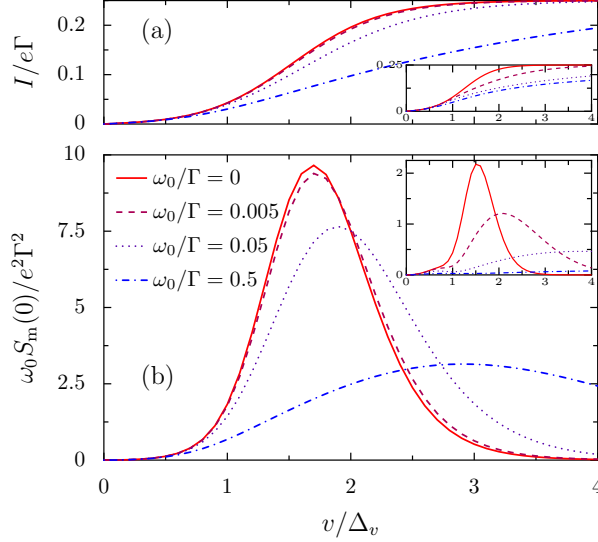


Figure 1.10: (a) Current and (b) zero-frequency noise as a function of bias voltage for increasing values of the adiabaticity parameter ω_0/Γ . In the figure, $\delta = 0$, $v_g = v_g^{\min}$, $\gamma_e = 10^{-2}$, $\tilde{T}/\Delta_v = 0.1$ and $\tilde{\alpha} = 10^{-6}$. Inset: Same as the main figure with $\delta = -1$.

reservoirs, i.e., $\hbar\Gamma \ll k_B T$, where cotunneling currents are exponentially suppressed. In this section, we investigate the role played by cotunneling that dominates the current inside the Coulomb diamond and which becomes relevant in the opposite regime of strong coupling to the leads, i.e., $\hbar\Gamma \gg k_B T$. We show that the current blockade survives for hybridization to the leads smaller than the energy scale E_E set by the bias voltage below which current is suppressed.

In the low-temperature regime $k_B T \ll \hbar\Gamma$ where cotunneling becomes relevant, the coefficients entering the Langevin and Fokker-Planck equations [see Eqs. (1.9) and (1.15)] have to be replaced by their strong-coupling counterpart [54, 67–70]. In particular, the average occupation of the dot for fixed deflection x entering the effective force (1.10) reads³

$$n_0(x) = \frac{1}{2} + \sum_{\sigma=\pm} \frac{1}{2\pi} \arctan\left(\frac{\sigma v/2 + v_g - x}{\tilde{\Gamma}/2}\right), \quad (1.31)$$

where $\tilde{\Gamma} = \hbar\Gamma/E_E^0$ measures the hybridization to the leads in units of the energy scale $E_E^0 = F_e^2/m\omega_0^2$. The corresponding quasistationary current for fixed x , from which the average current is obtained from Eq. (1.17), reads

$$\mathcal{I}(x) = \frac{e\Gamma}{4\pi} \sum_{\sigma=\pm} \sigma \arctan\left(\frac{\sigma v/2 + v_g - x}{\tilde{\Gamma}/2}\right). \quad (1.32)$$

³ Notice that we consider in this section a single-level quantum dot and spinless electrons, as the inclusion of spin and onsite Coulomb repulsion should not qualitatively change our results.

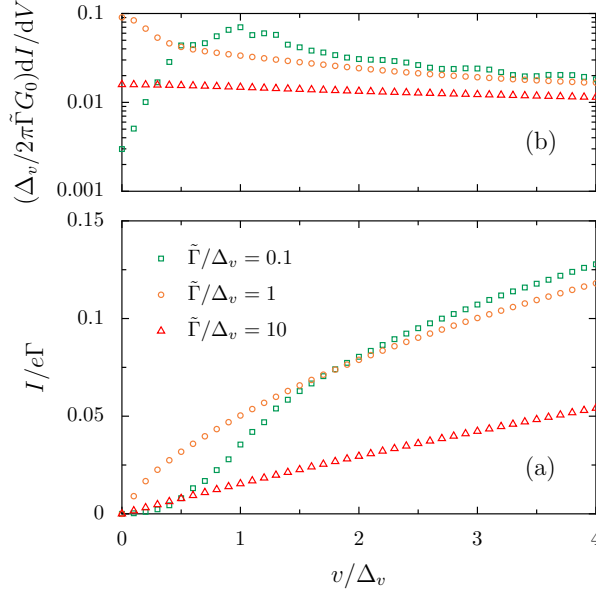


Figure 1.11: (a) Current I including the nonequilibrium Langevin dynamics as a function of bias v at the Euler buckling instability ($\delta = 0$) for a gate voltage $v_g = v_g^{\min}$ corresponding to the apex of the conducting region, see Eq. (1.22). (b) Corresponding differential conductance dI/dV , where $G_0 = e^2/2\pi\hbar$ denotes the conductance quantum. In the figure, $\tilde{\alpha} = 10^{-6}$, $\tilde{\omega}_0 = 10^{-3}$, and $\gamma_e = 0$ (no extrinsic dissipation).

The current-induced dissipation and fluctuations are given by [54, 69]

$$\gamma(x) = \frac{\tilde{\omega}_0 \tilde{\Gamma}^2}{8\pi} \sum_{\sigma=\pm} \frac{1}{[(\sigma v/2 + v_g - x)^2 + (\tilde{\Gamma}/2)^2]}, \quad (1.33)$$

$$d(x) = \frac{\tilde{\omega}_0}{2\pi\tilde{\Gamma}} \sum_{\sigma=\pm} \theta(\sigma v) \left[\arctan z + \frac{z}{1+z^2} \right] \frac{\frac{\sigma v/2 + v_g - x}{\tilde{\Gamma}/2}}{\frac{-\sigma v/2 + v_g - x}{\tilde{\Gamma}/2}}, \quad (1.34)$$

respectively, with $\tilde{\omega}_0 = \hbar\omega_0/E_E^0$.

In what follows, we focus on the system at the Euler instability ($\delta = 0$) where the current blockade is, at mean-field level, maximal [cf. Eq. (1.20)]. Since the stationary solution of the Fokker-Planck equation (1.15) is, for $\tilde{\omega}_0 \ll 1$, independent of the actual value of $\tilde{\omega}_0$ [19], we set $\tilde{\omega}_0 = 10^{-3}$ in what follows.

Our results for the average current based on the numerical solution to the Fokker-Planck equation (1.15) are shown in Fig. 1.11(a) for increasing hybridization to the leads $\tilde{\Gamma}$ which controls, in the cotunneling regime, the range of the current-induced dissipation (1.33) and fluctuations (1.34). For $\tilde{\Gamma}$ smaller than the energy gap Δ_v (see green squares and orange circles in the figure), the current-induced fluctuations have a dramatic effect on the I - V characteristics for bias voltages larger than Δ_v , suppressing totally the current blockade. However, for $\tilde{\Gamma} \leq 0.1\Delta_v$ and $v < \Delta_v$, cotunneling does not suppress the current blockade at low bias. We expect that for smaller $\tilde{\Gamma}$ (which is numerically very difficult to tackle), the current blockade should

be even more pronounced. As close to the mechanical instability, the gap (1.20) is very large, we foresee that the current blockade should be clearly visible in an experiment even in the regime of strong coupling to the electron reservoirs where cotunneling can be significant.

The above results are confirmed by the behavior of the differential conductance dI/dV shown in Fig. 1.11(b): For a hybridization to the leads small as compared to the energy gap (green squares in the figure), the differential conductance is clearly suppressed at low bias voltage, while for larger $\tilde{\Gamma}$, the conductance acquires a finite value which is almost constant as a function of the bias voltage [orange circles and red triangles in Fig. 1.11(b)].

We conclude this section by noticing that the features of the classical current blockade in the vicinity of a mechanical instability are qualitatively the same in the sequential-tunneling and cotunneling transport regimes [20]. In the former case, the electronic temperature defines the relevant energy scale below which the current blockade is observable (see Sec. 1.2.3), while in the latter case, it is the hybridization to the electron reservoirs that plays a similar role. The enhancement of the current blockade at the Euler instability is thus a universal phenomenon that does not depend on the transport regime one considers.

1.3 Current-induced discontinuous Euler instability

In this second part of Chapter 1, we now focus on the role played by the electron-phonon coupling *intrinsic* to the nanoresonator. As in Sec. 1.2, the electronic degrees of freedom couple to the vibronic motion through the occupation n_d of excess electrons on the metallic island forming the SET.⁴ Specifically, we assume that the electron-vibron coupling does not break the underlying parity symmetry of the vibronic dynamics under $X \rightarrow -X$. This follows naturally when the coupling emerges from the electron-phonon coupling intrinsic to the nanobeam [61] and implies that the coupling depends only on even powers of the vibronic mode coordinate X . The dominant coupling is thus now quadratic in X , and Eq. (1.8) is replaced by

$$H_c = \frac{g}{2} X^2 n_d, \quad (1.35)$$

with a coupling constant $g > 0$ [61]. When there is a significant contribution to the electron-vibron coupling originating from the electrostatic dot-gate interaction, we envision a symmetric gate setup consistent with Eq. (1.35).

The current-induced force $-gXn_0(X)$ resulting from the coupling (1.35), with $n_0(X)$ the average occupation of the quantum dot for fixed deflection X , has dramatic effects, as follows from a stability analysis of the vibrational motion [15]. The (meta)stable positions of the nanobeam are obtained by setting the new effective force

$$f_{\text{eff}}(x) = \epsilon x - x^3 - x n_0(x) \quad (1.36)$$

to zero. Here and below, we employ dimensionless variables by introducing characteristic scales $E_o = g^2/\alpha$ of energy, $l_o = \sqrt{g/\alpha}$ of length, and $\omega_o = \sqrt{g/m}$ of frequency (or time t) from a comparison of the quartic vibron potential in Eq. (1.2) and the electron-vibron coupling (1.35). Specifically, we introduce the reduced variables $x = X/l_o$, $p = P/m\omega_o l_o$, $\tau = \omega_o t$, $v = V/E_o$,

⁴ In this section, we consider a metallic quantum dot, i.e., presenting a large number of electronic levels. The problem of a semiconducting (molecular) quantum dot has been analyzed in Ref. [84], where it was shown that the results presented in this section do not change qualitatively.

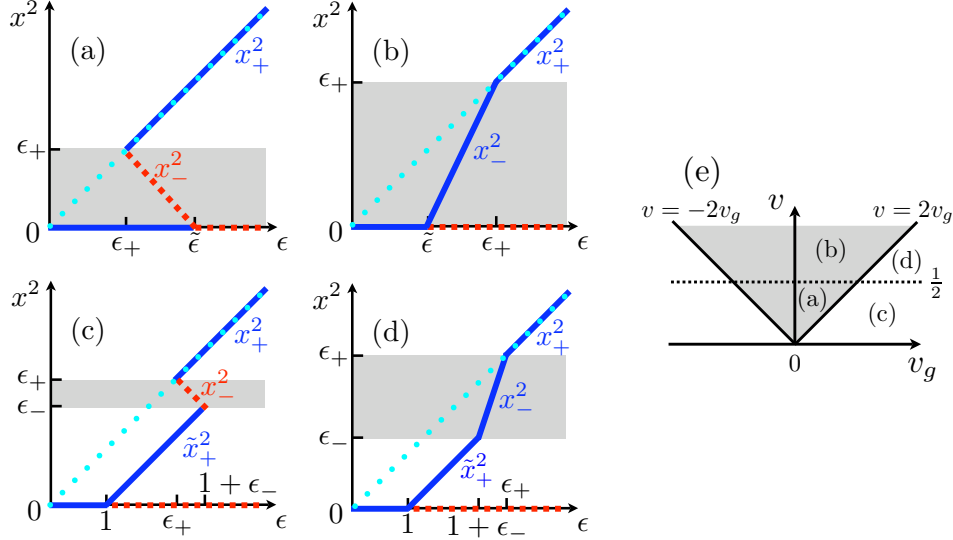


Figure 1.12: (Meta)stable (solid blue lines) and unstable (dashed red lines) positions of the nanobeam vs. scaled force ϵ for (a) $|v_g| < v/2$, $v < 1/2$, (b) $|v_g| < v/2$, $v > 1/2$, (c) $v_g > v/2$, $v < 1/2$ (for $\epsilon_+ > 1$; a similar plot holds for $\epsilon_+ < 1$), (d) $v_g > v/2$, $v > 1/2$, as indicated in the v_g - v plane in (e). The dotted blue line is the result without electron-vibron coupling. Notation: $\epsilon_{\pm} = 2v_g \pm v$, $\tilde{\epsilon} = 1/2 + v_g/v$, $x_+^2 = \epsilon$, $\tilde{x}_+^2 = \epsilon - 1$, and $x_-^2 = (\epsilon - \tilde{\epsilon})/(1 - 1/2v)$. Grey indicates conducting regions.

$v_g = V_g/E_o$ and the reduced compressional force $\epsilon = -m\omega^2/g$. In Eq. (1.36), the average occupation of the dot reads for $v > 0$ as

$$n_0(x) = \begin{cases} 1, & v_g(x) > v/2, \\ \frac{1}{2} + \frac{v_g(x)}{v}, & -v/2 \leq v_g(x) \leq v/2, \\ 0, & v_g(x) < -v/2, \end{cases} \quad (1.37)$$

with $v_g(x) = v_g - x^2/2$. Our results are summarized in the stability diagrams in Fig. 1.12. The most striking results of this analysis are: (i) The current flow renormalizes the critical force required for buckling towards larger values. (ii) At low biases, the buckled state can appear via a discontinuous transition.

These results can be understood most directly in terms of the potential $v_{\text{eff}}(x)$ associated with $f_{\text{eff}}(x)$. Focusing on the current-carrying region (shown in grey in Fig. 1.12 and delineated by $\max\{0, \epsilon_-\} < x^2 < \epsilon_+$ with $\epsilon_{\pm} = 2v_g \pm v$), we find

$$v_{\text{eff}}(x) = \frac{1}{2} \left(-\epsilon + \frac{v + 2v_g}{2v} \right) x^2 + \frac{1}{4} \left(1 - \frac{1}{2v} \right) x^4. \quad (1.38)$$

The quadratic term shows that the current indeed stabilizes the unbuckled state, renormalizing the critical force to $\tilde{\epsilon} = 1/2 + v_g/v$ when $\epsilon_- < 0 < \epsilon_+$ [Figs. 1.12(a) and 1.12(b)]. Remarkably, however, the current-induced contribution to the quartic term is negative at small x^2 and thus *destabilizes* the unbuckled state. According to Eq. (1.38), the quartic term in the current-induced potential becomes increasingly significant as the bias voltage v decreases and we find

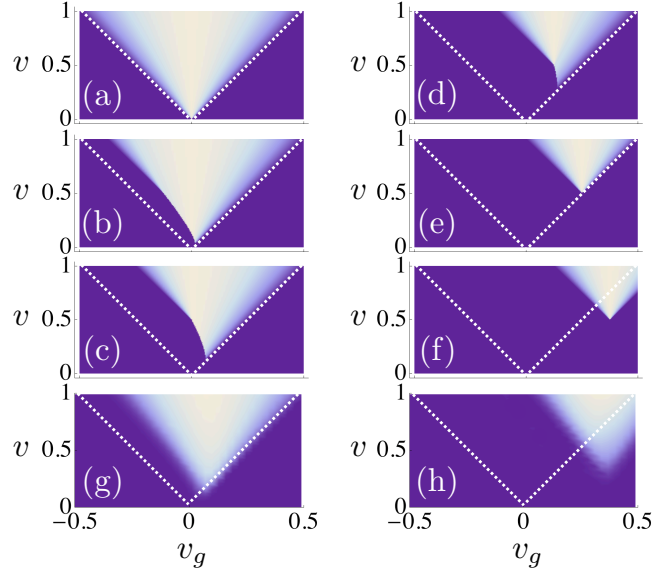


Figure 1.13: Conductance $G = RI/V$ in the v_g - v plane for applied force (a) $\epsilon \leq 0$, (b) $\epsilon = 0.25$, (c),(g) $\epsilon = 0.5$, (d) $\epsilon = 0.75$, (e) $\epsilon = 1$, (f),(h) $\epsilon = 1.25$, within (a)–(f) stability analysis and (g),(h) full Langevin dynamics [15]. Color scale: $G = 0 \rightarrow 1/4$ from dark blue to white. Dotted lines delineate the Coulomb diamond for $g = 0$.

that the overall prefactor of the quartic term becomes *negative* when $v < 1/2$. It is important to note that this does not imply a globally unstable potential since the current-induced force contributes only for small x^2 . A sign reversal of the quartic term is also a familiar occurrence in the Landau theory of tricritical points which connect between second- and first-order transition lines [85]. In close analogy, the sign reversal of the quartic term in the effective potential (1.38) signals a discontinuous Euler instability which reverts to a continuous transition at biases $v > 1/2$ where the prefactor of the quartic term remains positive.

Specifically, when $v > 1/2$ [Figs. 1.12(b) and 1.12(d)], the current-induced potential renormalizes the parameters of the vibronic Hamiltonian but leaves the quartic term positive. This modifies how the position of the minimum depends on the applied force in the conducting region $\max\{0, \epsilon_-\} < x^2 < \epsilon_+$, but the Euler instability remains continuous. When $v < 1/2$, the equilibrium position at finite x becomes unstable within the entire current-carrying region. This leads to a discontinuous Euler transition when $\epsilon_- < 0 < \epsilon_+$ [Fig. 1.12(a)] and to multistability in the region $\epsilon_- < x^2 < \epsilon_+$ when $\epsilon_- > 0$ [Fig. 1.12(c)].

At the level of the stability analysis, we can also obtain the current I by evaluating the rate-equation result [86] $RI(x)/V = 1/4 - [v_g(x)/v]^2$ at the position of the most stable minimum (here, $R \gg h/e^2$ denotes the tunneling resistance). Corresponding results in the v_g - v plane are shown in Figs. 1.13(a)–(f) for various values of the applied force ϵ . By comparison with the Coulomb diamond in the absence of the electron-vibron coupling (dotted lines in Fig. 1.13), we see that the Euler instability leads to a current blockade over a significant parameter range. For $v > 1/2$, the blockade is a manifestation of the classical current blockade (see Sec. 1.2) caused by the induced linear electron-vibron coupling when expanding Eq. (1.35) about the buckled state. In contrast, for $v < 1/2$, the current blockade is a direct consequence of the

discontinuous Euler instability. We have seen above that in this regime, the buckled state becomes unstable throughout the entire current-carrying region. As a result, the current-induced force will always drive the system out of the current-carrying region, explaining the current blockade. An intriguing feature of this novel tricritical current blockade is the curved boundary of the apparent Coulomb-blockade diamond (Fig. 1.13), a behavior which is actually observed in nanoelectromechanical systems [87].

To investigate the robustness of the stability analysis presented above against fluctuations, we turn to the complete vibronic Langevin dynamics. Numerical results for the scaled linear conductance $G = RI/V$ are shown in Figs. 1.13(g) and 1.13(h), using the same parameters as in Figs. 1.13(c) and 1.13(f). We observe that the fluctuations reduce the size of the blocked region and blur the edges of the conducting regions as the system can explore more conducting states in phase space. Nevertheless, the conclusions of the stability analysis clearly remain valid qualitatively.

1.4 Conclusion

In this chapter, we have presented a general approach to the interplay between continuous mechanical instabilities and current flow in nanoelectromechanical systems in terms of a nonequilibrium Born-Oppenheimer approach, and have applied our general framework to the Euler buckling instability. In particular we have investigated the consequences of a capacitive electromechanical coupling in a suspended single-electron transistor when the supporting beam is brought close to the Euler buckling instability by a lateral compression force. Our main result is that the low-bias current blockade originating from the coupling between the electronic degrees of freedom and the classical resonator can be enhanced by several orders of magnitude in the vicinity of the instability. We showed that both the mechanical as well as the electronic properties of this regime can be described in an asymptotically *exact* manner based on a Langevin equation. These results are a direct consequence of the continuous nature of the Euler buckling instability and the associated “critical slowing down” of the fundamental bending mode of the beam at the instability. In fact, more generally our results frequently have close and instructive analogies with the mean-field theory of second-order phase transitions [15, 19]. We focused on the sequential-tunneling transport regime of single-level quantum dots, but we have shown that our results remain qualitatively valid also in the resonant transport regime.

We also have investigated the current noise in NEMS close to a continuous mechanical instability. We have predicted a drastic enhancement of the current noise when the nanobeam supporting the quantum dot is brought to the Euler instability, resulting in very large Fano factors that are well above the Poisson limit. This exponential enhancement at the buckling instability is directly related to the (algebraic) enhancement of the current blockade. We developed a rather detailed picture of the underlying physics in terms of a telegraph-noise model. While such large Fano factors may make the observation of the low-bias current blockade more challenging, the large noise levels predicted in this work would serve also as a clear experimental signature of the interplay between electronic and mechanical degrees of freedom in NEMS close to continuous mechanical instabilities.

Finally, we have studied the role played by the electron-phonon coupling intrinsic to the nanoresonator. Remarkably, the current flow in this case modifies *qualitatively* the nature of the Euler buckling instability from a continuous to a tricritical transition. Likewise, the instability induces a novel tricritical current blockade at low bias.

While Secs. 1.2 and 1.3 have considered the effects of the capacitive and intrinsic couplings independently, it will be interesting to investigate in the future how the dynamics of the nanoresonator and its transport properties behave when both couplings have the same order of magnitude and are both taken into account.

Our results apply most directly to quantum dots situated on nanobeams or carbon nanotubes. Applying strain to the nanobeam in a controlled manner could, in principle, be experimentally performed with the help of a break junction. In fact, it is quite conceivable that, e.g., some carbon nanotube structures happen to be close to the Euler instability due to specifics in the fabrication of individual nanostructures. Our predictions may be helpful to identify such “anomalous” (and potentially interesting) samples.

Related publications

- F. Elste, G. Weick, C. Timm, F. von Oppen
Current-induced conformational switching in single-molecule junctions
[Appl. Phys. A **93**, 345 \(2008\)](#)
- G. Weick, F. Pistolesi, E. Mariani, F. von Oppen
Discontinuous Euler instability in nanoelectromechanical systems
[Phys. Rev. B **81**, 121409\(R\) \(2010\)](#)
- G. Weick, F. von Oppen, F. Pistolesi
Euler buckling instability and enhanced current blockade in suspended single-electron transistor
[Phys. Rev. B **83**, 035420 \(2011\)](#)
- G. Weick, D. M.-A. Meyer
Cotunneling, current blockade, and backaction forces in nanobeams close to the Euler buckling instability
[Phys. Rev. B **84**, 125454 \(2011\)](#)
- J. Brüggemann, G. Weick, F. Pistolesi, F. von Oppen
Large current noise in nanoelectromechanical systems close to continuous mechanical instabilities
[Phys. Rev. B **85**, 125441 \(2012\)](#)

Chapter 2

A plasmonic analogue of graphene

2.1 Introduction

Light has been the source of inspiration for scientific thinking for millennia. Ancient Assyrians developed the first lenses in order to bend the trajectory of light and control its propagation. In contrast to the macroscopic scale, the use of light to observe microscopic structures poses difficulties due to the diffraction limit [88]. In an attempt to overcome this limit and observe subwavelength structures, plasmonic nanostructures have been created [89, 90], like isolated metallic nanoparticles [91]. The evanescent field at the surface of the nanoparticle, associated to the localized surface plasmon resonance [92], produces strong optical field enhancement in the subwavelength region, allowing one to overcome the diffraction limit and achieve resolution at the molecular level [93].

While the field of plasmonics mostly focuses on single or few structures, the creation of ordered arrays of nanoparticles constitutes a bridge to the realm of metamaterials. Plasmonic metamaterials exhibit unique properties beyond traditional optics, like negative refractive index [94–96], perfect lensing [97, 98], the exciting perspective of electromagnetic invisibility cloaking [99–101], “trapped rainbow” slow light exploiting the inherent broadband nature of plasmonics [102], and the ability to perform mathematical operations (“metamaterial analog computing”) [103]. Indeed, in plasmonic metamaterials the interaction between localized surface plasmons on individual nanoparticles generates extended plasmonic modes involving all plasmons at once, as has been explored experimentally in one- and two-dimensional arrays of gold [104–106] and silver nanoparticles [107–109] and studied theoretically by means of classical electromagnetic calculations [110–115]. Understanding the nature and properties of these plasmonic modes (referred to as “collective plasmons” in what follows) is of crucial importance as they are the channel guiding electromagnetic radiation with strong lateral confinement over macroscopic distances.

Collective plasmons in periodic arrays of metallic nanoparticles are an active area of research in plasmonics [116] because the interaction of the localized surface plasmon resonances can lead to dramatic changes in the overall optical response of such structures. For example, it was both predicted [117, 118] and observed [119–121] that the plasmonic response of a periodic array of nanoparticles could be significantly narrowed with respect to the single particle response if the interparticle separation was of the order of the resonant wavelength of the localized surface plasmon. Further work has shown that these coupled resonances are relevant to applications in light emission [122]. Arrays of metallic nanoparticles may be designed to exhibit stop-gaps and band-edges [123] and are also being intensively investigated in the context of light harvesting for photovoltaic devices [124].

The dispersion of collective plasmons and their physical nature crucially depend on the lattice structure of the metamaterial and on the microscopic interaction between the localized

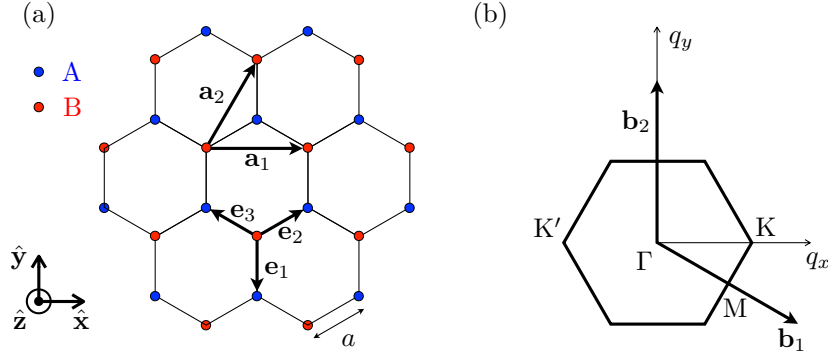


Figure 2.1: (a) Honeycomb lattice with lattice constant a and lattice vectors $\mathbf{a}_1 = a(\sqrt{3}, 0)$ and $\mathbf{a}_2 = a(\frac{\sqrt{3}}{2}, \frac{3}{2})$. The three vectors $\mathbf{e}_1 = a(0, -1)$, $\mathbf{e}_2 = a(\frac{\sqrt{3}}{2}, \frac{1}{2})$ and $\mathbf{e}_3 = a(-\frac{\sqrt{3}}{2}, \frac{1}{2})$ connect the A and B inequivalent lattice sites (blue/light gray and red/dark gray dots in the figure). (b) First Brillouin zone in reciprocal space with primitive vectors $\mathbf{b}_1 = \frac{2\pi}{3a}(\sqrt{3}, -1)$ and $\mathbf{b}_2 = \frac{4\pi}{3a}(0, 1)$.

surface plasmons. A lattice which recently generated remarkable interest in the condensed matter community is the honeycomb structure exhibited by graphene, a two-dimensional (2D) monolayer of carbon atoms (see Fig. 2.1) [125]. In the case of graphene, the hopping of electrons between neighboring atoms gives rise to a rich band structure characterized by the presence of fermionic massless Dirac quasiparticles close to zero energy [126,127]. The chirality associated with pseudo-relativistic Dirac fermions results in several of the remarkable properties of graphene, such as a nontrivial Berry phase accumulated in parallel transport [128,129] and the suppression of electronic backscattering from smooth scatterers [130]. Undoubtedly, it would be exciting to harvest the remarkable physical properties of electrons in graphene in suitably designed plasmonic metamaterials by analyzing the Hamiltonian and the consequent nature of collective plasmon eigenmodes in 2D honeycomb lattices of metallic nanoparticles. This is the purpose of the present chapter.

In Sec. 2.2, we study in detail the properties of extended plasmonic modes in a honeycomb array of nanoparticles and show that these modes represent chiral massless Dirac-like plasmons. As the damping of such modes, which will limit their propagation in the array, is of crucial interest for potential applications, we study in Sec. 2.3 the decay of plasmons in a somewhat simpler system which however constitutes the building block of any plasmonic array, that is, a nanoparticle dimer. Another point of crucial interest in view of possible applications of Dirac-like plasmonic excitations is their coupling to light, which may trigger the plasmons. Motivated by this issue, we study in Sec. 2.4 how plasmons couple to light, hence forming plasmon polaritons.

2.2 Dirac plasmons in honeycomb arrays of metallic nanoparticles

In this section, we analytically show how the problem of interacting localized surface plasmons in the honeycomb structure can be mapped to the kinetic problem of electrons hopping in graphene, yielding massless Dirac-like bosonic collective plasmons in the vicinity of two Dirac points in the Brillouin zone. The conical dispersion of classical plasmons in a honeycomb lattice

of nanoparticles has been discussed numerically in the past for out-of-plane or purely in-plane polarization [131]. In quite different physical systems (e.g., photonic crystals [132–137], acoustic waves in periodic hole arrays [138], cold atoms [139], microwaves in dielectric resonator arrays [140,141], exciton-polaritons [142,143]), conical dispersions were also found in “artificial graphene” due to the honeycomb symmetry [144]. Here we unveil the full Dirac Hamiltonian of quantum collective plasmons as well as the pseudospin structure of the corresponding eigenmodes for dipolar localized surface plasmons with arbitrary orientation. The existence of Dirac points is robust for a small in-plane component of the polarization, where the system maps to strained graphene [145,146], while band gaps can emerge for increasing in-plane polarization. At energies away from the Dirac point, van Hove singularities emerge in the collective plasmon density of states, associated with Lifshitz transitions in the topology of equipotential lines [147]. Our analysis highlights the physical nature of collective plasmon eigenmodes as well as the tunability of their band structure and of the corresponding density of states with the polarization of light, which can be crucial for enhancing the coupling of light with the plasmonic metamaterial at different wavelengths.

2.2.1 Model

We consider an ensemble of identical spherical metallic nanoparticles of radius r forming a 2D honeycomb lattice with lattice constant a embedded in a dielectric medium with dielectric constant ϵ_m (see Fig. 2.1). The nanoparticles are located at positions \mathbf{R}_s , with $s = A, B$ a sublattice index which distinguishes the inequivalent lattice sites. Each individual nanoparticle supports a localized surface plasmon resonance which can be triggered by an oscillating external electric field with wavelength λ much larger than r . Under such a condition, the localized surface plasmon is a dipolar collective electronic excitation at the Mie frequency $\omega_0 = \omega_p / \sqrt{1 + 2\epsilon_m}$, which typically lies in the visible or near-infrared part of the spectrum [92]. Here, $\omega_p = \sqrt{4\pi n_e e^2 / m_e}$ is the plasma frequency, with n_e , $-e$ and m_e the electron density, charge, and mass, respectively. The localized surface plasmon corresponding to the electronic center-of-mass excitation can be generally considered as a quantum bosonic mode, particularly when the size of the nanoparticle is such that quantization effects are important [4, 5, 7–9, 148–151]. The noninteracting part of the Hamiltonian describing the independent localized surface plasmons on the honeycomb lattice sites reads

$$H_0 = \sum_{s=A,B} \sum_{\mathbf{R}_s} \left[\frac{\Pi_s^2(\mathbf{R}_s)}{2M} + \frac{M}{2} \omega_0^2 h_s^2(\mathbf{R}_s) \right], \quad (2.1)$$

where $h_s(\mathbf{R})$ is the displacement field associated with the electronic center of mass at position \mathbf{R} , $\Pi_s(\mathbf{R})$ its conjugated momentum and $M = N_e m_e$ its mass, with N_e the number of valence electrons in each nanoparticle [4, 150].

The nature of the coupling between localized surface plasmons in different nanoparticles depends on their size and distance. Provided that the wavelength associated with each localized surface plasmon is much larger than the interparticle distance a and that $r \lesssim a/3$ [111, 112], each plasmon can be considered as a point dipole with dipole moment $\mathbf{p} = -e N_e h_s(\mathbf{R}) \hat{\mathbf{p}}$ which interacts with the neighboring ones through dipole-dipole interaction. Moreover, it has been numerically shown [131] that a quasistatic approximation which only takes into account the near field generated by each dipole qualitatively reproduces the results of more sophisticated simulations in which retardation effects are included. Within such a quasistatic approximation,

the interaction between two dipoles \mathbf{p} and \mathbf{p}' located at \mathbf{R} and \mathbf{R}' , respectively, reads

$$V_{\text{d-d}} = \frac{\mathbf{p} \cdot \mathbf{p}' - 3(\mathbf{p} \cdot \mathbf{n})(\mathbf{p}' \cdot \mathbf{n})}{\epsilon_{\text{m}} |\mathbf{R} - \mathbf{R}'|^3} \quad (2.2)$$

with $\mathbf{n} = (\mathbf{R} - \mathbf{R}')/|\mathbf{R} - \mathbf{R}'|$. In what follows, we assume that in a collective plasmon eigenmode all nanoparticles are polarized in the same direction $\hat{\mathbf{p}} = \sin \theta (\sin \varphi \hat{\mathbf{x}} - \cos \varphi \hat{\mathbf{y}}) + \cos \theta \hat{\mathbf{z}}$, where θ is the angle between $\hat{\mathbf{p}}$ and $\hat{\mathbf{z}}$, and φ the angle between the projection of $\hat{\mathbf{p}}$ in the xy plane and \mathbf{e}_1 [see Fig. 2.1(a)]. This can be achieved by an external electric field associated with light of suitable polarization. We thus write the total Hamiltonian of our system of coupled localized surface plasmons as

$$H = H_0 + H_{\text{int}}, \quad (2.3)$$

where H_0 is given by Eq. (2.1) and where the dipole-dipole interaction term reads

$$H_{\text{int}} = \frac{(eN_e)^2}{\epsilon_{\text{m}} a^3} \sum_{\mathbf{R}_B} \sum_{j=1}^3 \mathcal{C}_j h_B(\mathbf{R}_B) h_A(\mathbf{R}_B + \mathbf{e}_j). \quad (2.4)$$

Here, $\mathcal{C}_j = 1 - 3 \sin^2 \theta \cos^2(\varphi - 2\pi[j-1]/3)$, and the vectors \mathbf{e}_j connect the A and B sublattices [see Fig. 2.1(a)]. In Eq. (2.4), we only consider the dipole-dipole interaction between nearest neighbors, as the effect of interactions beyond nearest neighbors does not qualitatively change the plasmonic spectrum [26].

2.2.2 Analogy with massless Dirac fermions in graphene

The analogy between the plasmonic structure of Fig. 2.1 and the electronic properties of graphene becomes transparent by introducing the bosonic ladder operators

$$a_{\mathbf{R}} = \sqrt{\frac{M\omega_0}{2\hbar}} h_A(\mathbf{R}) + i \frac{\Pi_A(\mathbf{R})}{\sqrt{2\hbar M\omega_0}}, \quad (2.5a)$$

$$b_{\mathbf{R}} = \sqrt{\frac{M\omega_0}{2\hbar}} h_B(\mathbf{R}) + i \frac{\Pi_B(\mathbf{R})}{\sqrt{2\hbar M\omega_0}}, \quad (2.5b)$$

which satisfy the commutation relations $[a_{\mathbf{R}}, a_{\mathbf{R}'}^\dagger] = [b_{\mathbf{R}}, b_{\mathbf{R}'}^\dagger] = \delta_{\mathbf{R}, \mathbf{R}'}$ and $[a_{\mathbf{R}}, b_{\mathbf{R}'}^\dagger] = 0$. As we will show in the following, the introduction of such operators not only gives access to the plasmon dispersion (which can be calculated classically as well [26]), but also unveils the Dirac nature of the collective plasmon quantum states. The harmonic Hamiltonian (2.1) can be written in terms of the bosonic operators (2.5) as

$$H_0 = \hbar\omega_0 \sum_{\mathbf{R}_A} a_{\mathbf{R}_A}^\dagger a_{\mathbf{R}_A} + \hbar\omega_0 \sum_{\mathbf{R}_B} b_{\mathbf{R}_B}^\dagger b_{\mathbf{R}_B}, \quad (2.6)$$

while Eq. (2.4) transforms into

$$H_{\text{int}} = \hbar\Omega \sum_{\mathbf{R}_B} \sum_{j=1}^3 \mathcal{C}_j b_{\mathbf{R}_B}^\dagger \left(a_{\mathbf{R}_B + \mathbf{e}_j} + a_{\mathbf{R}_B + \mathbf{e}_j}^\dagger \right) + \text{h.c.} \quad (2.7)$$

In Eq. (2.7), $\Omega = \omega_0(r/a)^3(1 + 2\epsilon_{\text{m}})/6\epsilon_{\text{m}}$, such that $\Omega \ll \omega_0$. The first term on the right-hand side of Eq. (2.7) resembles the electronic tight-binding Hamiltonian of graphene [126, 127], except for three major differences: (i) The Hamiltonian of graphene describes fermionic particles

(electrons), while we deal here with *bosonic* excitations (localized surface plasmons). (ii) In graphene, an electron “hops” from one lattice site to a neighboring one, i.e., the underlying mechanism linking the two inequivalent sublattices is purely kinetic. In the present case, the mechanism coupling the two sublattices is purely induced by near-field (dipolar) *interactions*, leading to the creation of a localized surface plasmon excitation at lattice site \mathbf{R}_B and the annihilation of another localized plasmon at a nearest neighbor located at $\mathbf{R}_B + \mathbf{e}_j$. (iii) In (unstrained) graphene, the hopping matrix element between two neighboring atoms is the same for all three bonds. In contrast, in our case the three energy scales $\hbar\Omega\mathcal{C}_j$ in Eq. (2.4) are in general different and can be tuned by the direction of the polarization $\hat{\mathbf{p}}$ of the collective plasmon eigenmode, which can be controlled by means of an external light field. For $0 < \theta \leq \theta_0$ and $\pi - \theta_0 \leq \theta < \pi$ with $\theta_0 = \arcsin \sqrt{1/3}$, the coefficients \mathcal{C}_j are all positive for any φ and have different values, resulting in different couplings between the bonds, thus mimicking the effect of strain in the lattice [146]. For $\theta_0 < \theta < \pi - \theta_0$, the signs of the coefficients \mathcal{C}_j depend on φ , and the analogy with strained graphene is no longer valid. In the special case where $\mathcal{C}_1 = \mathcal{C}_2 = \mathcal{C}_3$ (for $\theta = 0$ or π), we expect the collective plasmon spectrum to resemble that of the electronic band structure in graphene, since the Bloch theorem does not depend on the quantum statistics of the particles one considers, but only on the structure of the periodic lattice. This fact is also responsible for the conical dispersion presented by other systems with honeycomb symmetry [132, 138, 139]. As we will now show, two slight differences appear in the collective plasmon dispersion as compared to the graphene band structure, i.e., the effect of the Hamiltonian H_0 [Eq. (2.6)] is to produce a global energy shift (by an amount $\hbar\omega_0$), while the “anomalous” term $\propto b_{\mathbf{R}_B}^\dagger a_{\mathbf{R}_B + \mathbf{e}_j}^\dagger$ in Eq. (2.7) introduces corrections of order $(\Omega/\omega_0)^2$ to the spectrum.

2.2.3 Collective plasmon dispersion

Introducing the bosonic operators in momentum space $a_{\mathbf{q}}$ and $b_{\mathbf{q}}$ through

$$a_{\mathbf{R}} = \frac{1}{\sqrt{\mathcal{N}}} \sum_{\mathbf{q}} e^{i\mathbf{q}\cdot\mathbf{R}} a_{\mathbf{q}}, \quad b_{\mathbf{R}} = \frac{1}{\sqrt{\mathcal{N}}} \sum_{\mathbf{q}} e^{i\mathbf{q}\cdot\mathbf{R}} b_{\mathbf{q}}, \quad (2.8)$$

with \mathcal{N} the number of unit cells of the honeycomb lattice, the Hamiltonian (2.3) transforms into

$$H = \hbar\omega_0 \sum_{\mathbf{q}} (a_{\mathbf{q}}^\dagger a_{\mathbf{q}} + b_{\mathbf{q}}^\dagger b_{\mathbf{q}}) + \hbar\Omega \sum_{\mathbf{q}} [f_{\mathbf{q}} b_{\mathbf{q}}^\dagger (a_{\mathbf{q}} + a_{-\mathbf{q}}^\dagger) + \text{h.c.}] \quad (2.9)$$

with

$$f_{\mathbf{q}} = \sum_{j=1}^3 \mathcal{C}_j \exp(i\mathbf{q} \cdot \mathbf{e}_j). \quad (2.10)$$

The latter Hamiltonian is diagonalized by two successive Bogoliubov transformations. First, we introduce the two bosonic operators

$$\alpha_{\mathbf{q}}^\pm = \frac{1}{\sqrt{2}} \begin{pmatrix} f_{\mathbf{q}} \\ |f_{\mathbf{q}}| \end{pmatrix} a_{\mathbf{q}} \pm b_{\mathbf{q}} \quad (2.11)$$

in terms of which we obtain

$$H = \sum_{\tau=\pm} \sum_{\mathbf{q}} \left[(\hbar\omega_0 + \tau\hbar\Omega|f_{\mathbf{q}}|) \alpha_{\mathbf{q}}^{\tau\dagger} \alpha_{\mathbf{q}}^\tau + \tau \frac{\hbar\Omega|f_{\mathbf{q}}|}{2} (\alpha_{\mathbf{q}}^{\tau\dagger} \alpha_{-\mathbf{q}}^{\tau\dagger} + \text{h.c.}) \right]. \quad (2.12)$$

Second, we define two new bosonic modes

$$\beta_{\mathbf{q}}^{\pm} = \cosh \vartheta_{\mathbf{q}}^{\pm} \alpha_{\mathbf{q}}^{\pm} - \sinh \vartheta_{\mathbf{q}}^{\pm} \alpha_{-\mathbf{q}}^{\pm \dagger}, \quad (2.13)$$

with

$$\cosh \vartheta_{\mathbf{q}}^{\pm} = \frac{1}{\sqrt{2}} \left[\frac{1 \pm \Omega |f_{\mathbf{q}}| / \omega_0}{\sqrt{1 \pm 2\Omega |f_{\mathbf{q}}| / \omega_0}} + 1 \right]^{1/2}, \quad (2.14a)$$

$$\sinh \vartheta_{\mathbf{q}}^{\pm} = \mp \frac{1}{\sqrt{2}} \left[\frac{1 \pm \Omega |f_{\mathbf{q}}| / \omega_0}{\sqrt{1 \pm 2\Omega |f_{\mathbf{q}}| / \omega_0}} - 1 \right]^{1/2}, \quad (2.14b)$$

which diagonalize the Hamiltonian (2.12) as

$$H = \sum_{\tau=\pm} \sum_{\mathbf{q}} \hbar \omega_{\mathbf{q}}^{\tau} \beta_{\mathbf{q}}^{\tau \dagger} \beta_{\mathbf{q}}^{\tau}, \quad (2.15)$$

with the collective plasmon dispersion

$$\omega_{\mathbf{q}}^{\pm} = \omega_0 \sqrt{1 \pm 2 \frac{\Omega}{\omega_0} |f_{\mathbf{q}}|}. \quad (2.16)$$

The two collective plasmon branches reduce to $\omega_{\mathbf{q}}^{\pm} \simeq \omega_0 \pm \Omega |f_{\mathbf{q}}|$ to first order in $\Omega/\omega_0 \ll 1$, for which we have $\beta_{\mathbf{q}}^{\pm} \simeq \alpha_{\mathbf{q}}^{\pm}$.

The dispersion (2.16) is shown in Fig. 2.2 in the case of a polarization $\hat{\mathbf{p}}$ perpendicular to the plane of the honeycomb lattice [$\theta = 0$, Fig. 2.2(a)], in the case of an in-plane polarization [$\theta = \pi/2$, $\varphi = 0$, Fig. 2.2(b)], and for the special case $\theta = \arcsin \sqrt{1/3}$, $\varphi = 0$ [Fig. 2.2(c)]. In the first case [Fig. 2.2(a)], we have gapless modes with two inequivalent Dirac cones centered at the K and K' points located at $\pm \mathbf{K} = \frac{4\pi}{3\sqrt{3}a} (\pm 1, 0)$ in the first Brillouin zone [cf. Fig. 2.1(b)], while in the second case, the modes are gapped [Fig. 2.2(b)]. The dispersion shown in Fig. 2.2(c) corresponds to a polarization for which $\mathcal{C}_1 = 0$ in Eq. (2.4), i.e., the bonds linked by \mathbf{e}_1 [cf. Fig. 2.1(a)] are ineffective and the system is effectively translationally invariant along one direction. Hence, the collective plasmon dispersion in Fig. 2.2(c) does not depend on q_y and presents Dirac ‘‘lines’’.

2.2.4 Dirac-like collective plasmons

The analogy between the dispersion shown in Fig. 2.2(a) and the electronic band structure of graphene [126] is striking. Close to the two inequivalent Dirac points K and K' [see Fig. 2.1(b)], the function $f_{\mathbf{q}}$ defined in Eq. (2.10) expands as $f_{\mathbf{q}} \simeq -\frac{3a}{2} (\pm k_x + i k_y)$ with $\mathbf{q} = \pm \mathbf{K} + \mathbf{k}$ ($|\mathbf{k}| \ll |\mathbf{K}|$), such that the dispersion (2.16) is linear and forms a Dirac cone, $\omega_{\mathbf{k}}^{\pm} \simeq \omega_0 \pm v |\mathbf{k}|$, with group velocity $v = 3\Omega a/2$. Moreover, by expanding Eq. (2.15) in the vicinity of the Dirac points, we can identify the Hamiltonian $H^{\text{eff}} = \sum_{\mathbf{k}} \hat{\Psi}_{\mathbf{k}}^{\dagger} \mathcal{H}_{\mathbf{k}}^{\text{eff}} \hat{\Psi}_{\mathbf{k}}$ that effectively describes the collective plasmons. Here $\hat{\Psi}_{\mathbf{k}} = (a_{\mathbf{k},\text{K}}, b_{\mathbf{k},\text{K}}, b_{\mathbf{k},\text{K}'}, a_{\mathbf{k},\text{K}'})$ is a spinor operator, where K and K' denote the valley indices associated with the inequivalent Dirac points, and the 4×4 Hamiltonian reads

$$\mathcal{H}_{\mathbf{k}}^{\text{eff}} = \hbar \omega_0 \mathbf{1} - \hbar v \tau_z \otimes \boldsymbol{\sigma} \cdot \mathbf{k}. \quad (2.17)$$

In this notation, $\mathbf{1}$ corresponds to the identity matrix, τ_z to the Pauli matrix acting on the valley space (K/K'), while $\boldsymbol{\sigma} = (\sigma_x, \sigma_y)$ is the vector of Pauli matrices acting on the sublattice

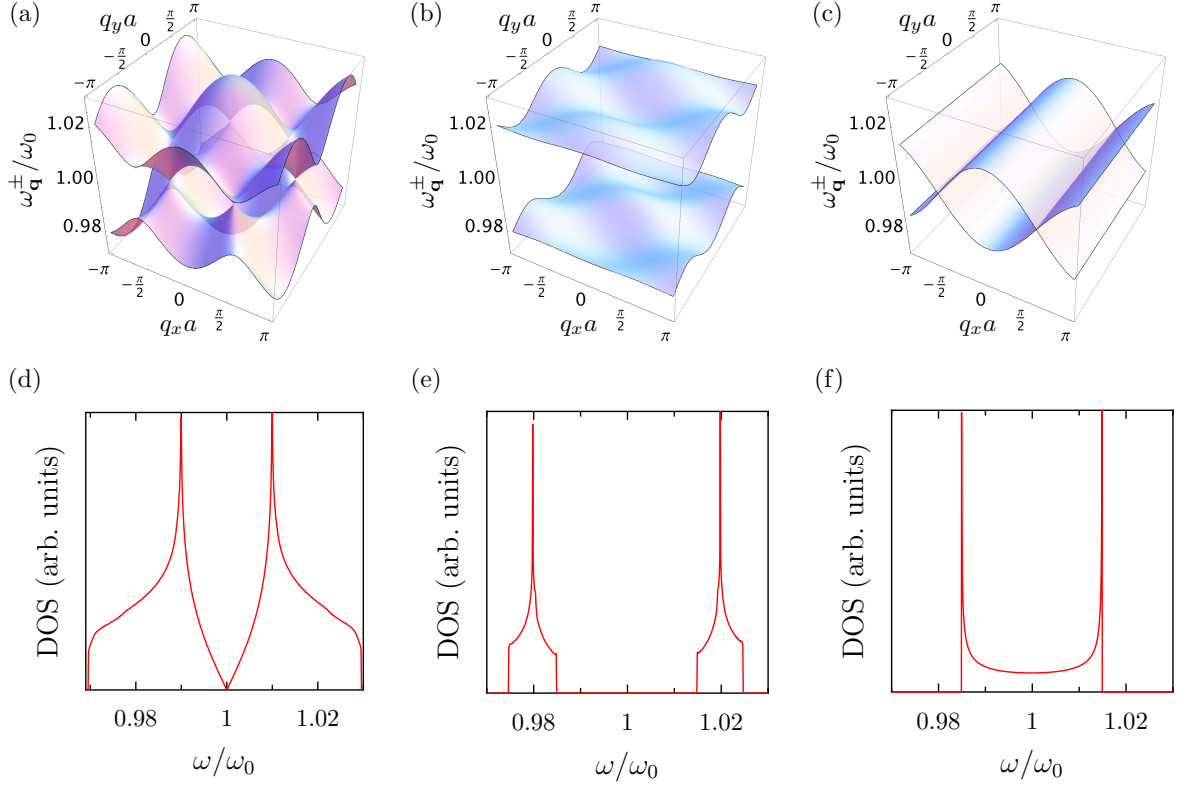


Figure 2.2: (a)–(c) Collective plasmon dispersion relation from Eq. (2.16) and (d)–(f) corresponding density of states for (a),(d) the out-of-plane mode ($\theta = 0$), (b),(e) one in-plane mode ($\theta = \pi/2$), and (c),(f) $\theta = \arcsin \sqrt{1/3}$. In the figure, $\varphi = 0$ and $\Omega/\omega_0 = 0.01$.

space (A/B). Up to a global energy shift of $\hbar\omega_0$, Eq. (2.17) corresponds to a *massless Dirac Hamiltonian* that is fulfilled by collective plasmons, in complete analogy with electrons in graphene [126,127]. The collective plasmon eigenstates of Eq. (2.17), $\psi_{\mathbf{k},K}^{\pm} = \frac{1}{\sqrt{2}}(1, \mp e^{i\xi_{\mathbf{k}}}, 0, 0)$ and $\psi_{\mathbf{k},K'}^{\pm} = \frac{1}{\sqrt{2}}(0, 0, 1, \pm e^{i\xi_{\mathbf{k}}})$ with $\xi_{\mathbf{k}} = \arctan(k_y/k_x)$, are characterized by chirality $\boldsymbol{\sigma} \cdot \hat{\mathbf{k}} = \pm 1$. As a consequence, collective plasmons will show similar effects to electrons in graphene like a Berry phase of π [128] and the absence of backscattering off smooth inhomogeneities [130]. This could have crucial implications for the efficient plasmonic propagation in array-based metamaterials.

In Fig. 2.2, the panels (d)–(f) show the density of states corresponding to the spectrum illustrated in the panels (a)–(c). It is interesting to notice the tunability of the density of states with the direction of the polarization, as well as the emergence of van Hove singularities. The latter are associated with Lifshitz transitions [147] in the topology of equipotential lines that percolate at specific energies. The tunability of van Hove singularities in the spectrum could be of crucial importance to increase the coupling of light of different wavelengths with extended collective plasmon modes.

For an arbitrary polarization of the localized surface plasmons, we can determine if the collective plasmon dispersion is gapless by imposing $|f_{\mathbf{q}}| = 0$ in Eq. (2.16), which leads to the

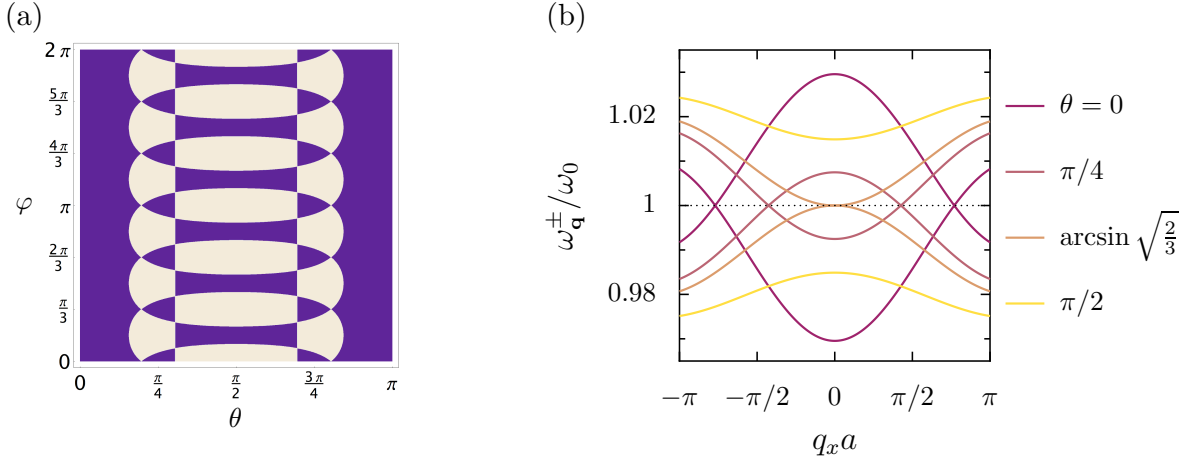


Figure 2.3: (a) Polarization angles (θ, φ) for which the collective plasmon dispersion is gapless (dark blue regions) and gapped (white regions). (b) Collective plasmon dispersion along the K'ΓK direction ($q_y = 0$) for different orientations θ of the dipoles and for $\varphi = 0$. In the figure, $\Omega/\omega_0 = 0.01$.

condition

$$0 \leq \frac{(\mathcal{C}_2 + \mathcal{C}_3)^2 - \mathcal{C}_1^2}{4\mathcal{C}_2\mathcal{C}_3} \leq 1 \quad (2.18)$$

for having gapless plasmonic modes [26]. In Fig. 2.3(a), we show in dark blue the regions of stability of a massless Dirac spectrum in the (θ, φ) parameter space for which one has gapless plasmon modes, an example of which is shown in Fig. 2.2(a). In Fig. 2.3(a), the white regions correspond to polarizations for which the collective plasmon dispersion is gapped [as an example, see Fig. 2.2(b)]. Thus, changing the polarization allows one to *qualitatively* change the collective plasmon spectrum. This is further illustrated in Fig. 2.3(b) where we show the collective plasmon dispersion along the K'ΓK direction [see Fig. 2.1(b)] for different angles θ of the polarization (in the figure, $\varphi = 0$). As one can see from Fig. 2.3(b), the two inequivalent Dirac points located at K and K' for $\theta = 0$ drift as one increases θ and they merge at $\mathbf{q} = 0$ for $\theta = \arcsin \sqrt{2/3}$, forming parabolic bands, to finally open a gap for $\theta > \arcsin \sqrt{2/3}$ (exemplified by $\theta = \pi/2$ in the figure).

2.2.5 Concluding remarks

In conclusion, we demonstrated in this section the strong analogies between the physical properties of electrons in graphene and those of collective plasmon modes in a 2D honeycomb lattice of metallic nanoparticles. Whereas the electronic states of graphene can be described by massless Dirac fermions, the collective plasmon eigenstates correspond to massless Dirac-like bosonic excitations. The spectrum of the latter can be fully tuned by the polarization of an external light field, opening exciting new possibilities for controlling the propagation of electromagnetic radiation with subwavelength lateral confinement in plasmonic metamaterials.

A limitation on the experimental observability of Dirac-like collective plasmons is plasmonic damping, which tends to blur the resonance frequencies. We tackle this important issue in Sec. 2.3 by considering the damping mechanisms in a nanoparticle dimer, which constitute

the building block to more complex plasmonic metamaterials, such as the honeycomb array of metallic nanoparticles that we have considered in this section. Another important issue in the view of the possible experimental realization of our proposal is how collective plasmons couple to light. The latter is the usual mean to trigger collective plasmons, resulting in plasmon polaritons. We address this crucial point in Sec. 2.4.

2.3 How do the dark and bright plasmonic modes decay in a metallic nanoparticle dimer?

The intense recent activity concerning nanoparticle dimers stems from the fact that it is the simplest system sustaining coupled plasmonic excitations. The near-field interaction (2.2) between the localized surface plasmons of two nanoparticles results in a bright mode (coupled to the electromagnetic field associated with visible light) and a dark one (weakly coupled to light due to its minute associated dipole moment). Both of these modes have been experimentally observed [152–158] and theoretically investigated [159–166]. On the one hand, the bright mode has been observed using laser excitation in various experimental systems [152–155]. On the other hand, the dark mode is difficult to excite in symmetric, homogeneous dimers with interparticle distance much smaller than the laser wavelength. However, this difficulty is less severe in heterogeneous dimers. The alternative experimental technique of electron energy loss spectroscopy (EELS) has recently provided an unambiguous detection of the dark mode [156–158].

The damping of these coupled modes is a crucial limiting factor for their experimental observation as well as for potential applications in the field of nanoplasmonics [90]. While the bright mode radiates in the far-field and hence has a radiative decay, the dark mode is obviously immune to radiation damping. It is then of paramount interest to understand the nonradiative decay channels at the origin of the experimentally-observed finite linewidth of the dark mode [156–158].

In this section we show that for sufficiently small nanoparticles, the main decay channel for the dark mode corresponds to Landau damping, which dominates over absorption losses. In the present context, the Landau damping is a purely quantum mechanical effect that leads to the decay of the collective excitation through the creation of electron-hole pairs [167]. We develop a general quantum theory of plasmonic excitations coupled to the environment of electron-hole excitations in a heterogeneous dimer of interacting metallic nanoparticles. Using bosonic Bogoliubov transformations and semiclassical techniques, we provide analytical expressions for the frequencies and lifetimes of the coupled plasmonic modes.

2.3.1 Model

For a single metallic nanoparticle, the separation of the electronic coordinates into center-of-mass and relative motion [5, 150] amounts to a description typical for an open quantum system. The dipolar localized surface plasmon (i.e., the center-of-mass coordinate) is coupled to an electronic environment (i.e., the bath of electron-hole pairs represented by the relative coordinates) and leads to the nonradiative decay of the collective excitations (Landau damping). The coupling between the two subsystems is a consequence of the breaking of Kohn's theorem [168, 169] due to the non-harmonicity of the confining potential, the latter arising from the positive ionic background. In addition, radiative damping arises from the coupling of the

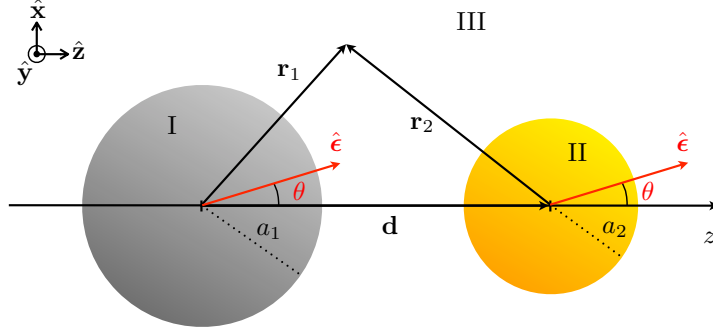


Figure 2.4: Sketch of a nanoparticle dimer formed by two spherical nanoparticles of radii a_1 and a_2 separated by a distance d , together with the coordinate system used in the text. The polarization $\hat{\epsilon}$ of the localized surface plasmons forming an angle θ with the z axis is also shown.

localized surface plasmon with electromagnetic field modes, while absorption (Ohmic) losses occur due to the finite resistivity of the metal.

Extending this approach to the case of a nanoparticle dimer (sketched in Fig. 2.4), the resulting electronic Hamiltonian can be written as [30]

$$H = H_{\text{pl}} + H_{\text{eh}} + H_{\text{pl-eh}}. \quad (2.19)$$

The plasmonic part reads

$$H_{\text{pl}} = \sum_{n=1}^2 \hbar \tilde{\omega}_n b_n^\dagger b_n + \hbar \Omega f(\theta) \left(b_1^\dagger b_2 + b_1^\dagger b_2^\dagger + \text{h.c.} \right), \quad (2.20)$$

where the index n is used to identify within the dimer the two spherical, neutral nanoparticles of radius a_n (each containing N_n electrons). The localized surface plasmon frequency $\tilde{\omega}_n = \omega_n (1 - N_{\text{out},n}/N_n)^{1/2}$ is redshifted with respect to the Mie frequency $\omega_n = [3N_n e^2 / m_e a_n^3 (\epsilon_d^{(n)} + 2\epsilon_m)]^{1/2}$ due to the $N_{\text{out},n}$ electrons spilling out of nanoparticle n [92]. Here, $-e$ and m_e denote the electron charge and mass, respectively. The dielectric constant $\epsilon_d^{(n)}$ takes into account the screening provided, in the case of noble metals, by the d electrons in nanoparticle n , and ϵ_m is the dielectric constant of the matrix in which the nanoparticles are embedded. In Eq. (2.20), the bosonic operator b_n (b_n^\dagger) annihilates (creates) a localized surface plasmon in nanoparticle n . The two plasmons interact through their near fields, giving rise to the second term in the right-hand side of Eq. (2.20), where $\Omega = \frac{1}{2} \prod_{n=1}^2 [\tilde{\omega}_n / (1 - N_{\text{out},n}/N_n)]^{1/2} (a_n/d)^{3/2}$ and $f(\theta) = 1 - 3\cos^2\theta$. Here, d is the center-to-center nanoparticle distance and θ is the angle formed by the polarization $\hat{\epsilon}$ of the localized surface plasmons and the z axis joining the two nanoparticles (see Fig. 2.4). In writing Eq. (2.20), we adopted as in Sec. 2.2 a quasistatic dipole-dipole approximation [cf. Eq. (2.2)] valid for $3a_n \lesssim d \ll c/\tilde{\omega}_n$, where c is the speed of light [30, 111, 112]. We further assumed that in each eigenmode, the two localized plasmons are polarized in the same direction $\hat{\epsilon}$.

Electron-hole excitations within each nanoparticle provide the electronic environment described by [5]

$$H_{\text{eh}} = \sum_{n=1}^2 \sum_{\alpha} \varepsilon_{n\alpha} c_{n\alpha}^\dagger c_{n\alpha}, \quad (2.21)$$

2.3 How do the dark and bright plasmonic modes decay in a metallic nanoparticle dimer?

where $c_{n\alpha}$ ($c_{n\alpha}^\dagger$) annihilates (creates) an electron in the n th nanoparticle associated with the one-body state $|n\alpha\rangle$ with energy $\varepsilon_{n\alpha}$ in the self-consistent potential V . Note that the form (2.21) implicitly assumes that tunneling of electrons between the two nanoparticles is neglected, which is justified by the interparticle distance that we consider here. Similarly to the case of a single nanoparticle discussed above, the coupling of the plasmon to the electronic environment comes from the non-harmonicity of the single-particle confinement, which in the jellium approximation with $\epsilon_d^{(n)} = \epsilon_m = 1$ reads

$$U_n(r_n) = \frac{N_n e^2}{2a_n^3} (r_n^2 - 3a_n^2) \Theta(a_n - r_n) - \frac{N_n e^2}{r_n} \Theta(r_n - a_n), \quad (2.22)$$

where r_n is the radial coordinate with respect to the center of nanoparticle n . Hence, the Hamiltonian $H_{\text{pl-eh}}$ in Eq. (2.19) can be written as [170]

$$H_{\text{pl-eh}} = \sum_{n=1}^2 \sqrt{\frac{\hbar}{2N_n m_e \tilde{\omega}_n}} (b_n + b_n^\dagger) \sum_{\alpha\beta} \langle n\alpha | \hat{\epsilon} \cdot \nabla U_n(r_n) | n\beta \rangle c_{n\alpha}^\dagger c_{n\beta}. \quad (2.23)$$

2.3.2 Coupled plasmonic modes

The quadratic Hamiltonian (2.20) representing the two coupled localized surface plasmons is diagonalized as

$$H_{\text{pl}} = \sum_{\sigma=\pm} \hbar \omega_\sigma B_\sigma^\dagger B_\sigma \quad (2.24)$$

by introducing the bosonic operators

$$B_\pm = \sum_{n=1}^2 (u_{n,\pm} b_n + \bar{u}_{n,\pm} b_n^\dagger). \quad (2.25)$$

For the general case of unequal frequencies $\tilde{\omega}_n$, following Tsallis' prescription for Bogoliubov transformations [171], we find [30]

$$\omega_\pm = \sqrt{\frac{\tilde{\omega}_1^2 + \tilde{\omega}_2^2}{2}} \pm \sqrt{4\Omega^2 \tilde{\omega}_1 \tilde{\omega}_2 f^2(\theta) + \left(\frac{\tilde{\omega}_1^2 - \tilde{\omega}_2^2}{2}\right)^2}, \quad (2.26)$$

$$u_{n,\pm} = [\pm \text{sign}\{f(\theta)\}]^{n-1} \frac{\omega_\pm + \tilde{\omega}_n}{2\sqrt{\tilde{\omega}_n \omega_\pm}} \sqrt{\frac{\omega_\pm^2 - \tilde{\omega}_n^2}{2\omega_\pm^2 - \tilde{\omega}_1^2 - \tilde{\omega}_2^2}}, \quad (2.27)$$

where $\bar{u}_{n,\pm}$ is obtained from $u_{n,\pm}$ by changing $\omega_\pm + \tilde{\omega}_n$ by $\omega_\pm - \tilde{\omega}_n$. In Eq. (2.27), $\hat{n} = 1(2)$ for $n = 2(1)$. The two plasmonic eigenmodes correspond to the coherent oscillation of the two localized surface plasmons. For $\theta = 0$, the low-energy (high-energy) mode with frequency ω_- (ω_+) can be thought of as the in-phase (anti-phase) motion of the two localized surface plasmons. Vice versa, for $\theta = \pi/2$, the $-$ and $+$ modes correspond to the anti-phase and in-phase motions, respectively. Figure 2.5(a) shows the transition between these two previous extreme cases as a function of the polarization angle θ . In the special case $\tilde{\omega}_1 = \tilde{\omega}_2$ [i.e., identical nanoparticles, thin solid and dashed lines in Fig. 2.5(a)], the in-phase mode (with nonvanishing dipole moment) can be excited by dipolar light and thus receives the name of "bright mode". It corresponds to the $-$ ($+$) eigenmode for polarization angles $\theta < (>)\theta_0$,

where $\theta_0 = \arccos(1/\sqrt{3})$ is the angle for which the dipole-dipole interaction in Eq. (2.20) vanishes. Conversely, the anti-phase mode (with vanishing dipole moment) corresponds to the $+$ ($-$) eigenmode for $\theta < (>)\theta_0$. Since it cannot be triggered by visible light, it is referred to as the “dark mode”. When $\tilde{\omega}_1 \neq \tilde{\omega}_2$ [thick, solid and dashed lines in Fig. 2.5(a)], the difference between bright and dark modes is less stringent, as both the $+$ and $-$ modes have a finite dipole moment for any θ . In this case the usage of bright (dark) modes refers to the larger (smaller) total dipole moment. Notice, moreover, that the dependence on the interparticle distance d of the \pm frequencies is encapsulated in Eq. (2.26) in the definition of Ω , so that $\omega_{\pm} - [(\tilde{\omega}_1^2 + \tilde{\omega}_2^2)/2]^{1/2} \sim \pm 1/d^3$.¹ Such a behavior, which directly follows from the form of the dipole-dipole interaction (2.2), has also been unveiled both theoretically [159, 161] and experimentally [153] in the case of nanoparticles of equal size and formed of the same material.

2.3.3 Landau damping

The modes previously described can be understood as resulting from the coupling of classical dipoles, as has been extensively discussed in the literature [92, 152–163]. Our quantum description is nevertheless crucial for the evaluation of the Landau damping of the two coupled plasmonic modes. The coupling Hamiltonian (2.23) associated with this decay channel can be expressed in terms of the bosonic operators (2.25) as

$$H_{\text{pl-eh}} = \sum_{n=1}^2 \sum_{\sigma=\pm} \Lambda_n \Delta u_{n,\sigma} \left(B_{\sigma} + B_{\sigma}^{\dagger} \right) \sum_{\alpha\beta} \hat{\epsilon} \cdot \mathbf{d}_{\alpha\beta}^{(n)} c_{n\alpha}^{\dagger} c_{n\beta}, \quad (2.28)$$

where $\Lambda_n = (\hbar m_e \omega_n^3 / 2N_n)^{1/2}$ and $\Delta u_{n,\sigma} = u_{n,\sigma} - \bar{u}_{n,\sigma}$. An explicit expression of the dipole matrix element $\mathbf{d}_{\alpha\beta}^{(n)} = \langle n\alpha | \mathbf{r} | n\beta \rangle$ can be found in Refs. [23, 30]. Equation (2.28) is obtained under the assumption that the self-consistent potential V is constant inside the nanoparticles and infinite outside. Such an assumption, which neglects the spill-out, is justified by density functional calculations for the one-particle case [5], as well as for dimers [164].

The zero-temperature Fermi’s golden rule decay rate of the $+$ and $-$ plasmonic modes from the Landau damping channel is then given from Eq. (2.28) by

$$\gamma_{\pm}^{\text{L}} = \frac{2\pi}{\hbar} \sum_{n=1}^2 \sum_{eh} |\Lambda_n \Delta u_{n,\pm} \mathbf{d}_{eh}^{(n)} \cdot \hat{\epsilon}|^2 \delta(\hbar\omega_{\pm} - E_e + E_h), \quad (2.29)$$

where $|ne\rangle$ and $|nh\rangle$ represent, respectively, electron and hole states in the self-consistent potential V for the n th nanoparticle. For spherically symmetric nanoparticles, the sum over e and h states is performed by introducing the density of states $\varrho_l^{(n)}(E)$ with fixed angular momentum l at energy E in nanoparticle n . The angular momentum selection rules lead to

$$\begin{aligned} \gamma_{\pm}^{\text{L}} = & \frac{16\pi}{3\hbar m_e^2 \omega_{\pm}^4} \sum_{n=1}^2 \frac{\Lambda_n^2 \Delta u_{n,\pm}^2}{a_n^2} \int_{\max\{E_{\text{F}}^{(n)}, \hbar\omega_{\pm}\}}^{E_{\text{F}}^{(n)} + \hbar\omega_{\pm}} dE E(E - \hbar\omega_{\pm}) \\ & \times \sum_l \varrho_l^{(n)}(E) \left[(l+1) \varrho_{l+1}^{(n)}(E - \hbar\omega_{\pm}) + l \varrho_{l-1}^{(n)}(E - \hbar\omega_{\pm}) \right], \end{aligned} \quad (2.30)$$

¹ This dependence on d strictly holds in the regime $|\tilde{\omega}_1^2 - \tilde{\omega}_2^2|/2\tilde{\omega}_1\tilde{\omega}_2 \ll 2\Omega|f(\theta)|/(\tilde{\omega}_1\tilde{\omega}_2)^{1/2} \ll 1$. In the case $2\Omega|f(\theta)|/(\tilde{\omega}_1\tilde{\omega}_2)^{1/2} \ll |\tilde{\omega}_1^2 - \tilde{\omega}_2^2|/2\tilde{\omega}_1\tilde{\omega}_2 \ll 1$, we have $\omega_+ \simeq \max\{\tilde{\omega}_1, \tilde{\omega}_2\}$ and $\omega_- \simeq \min\{\tilde{\omega}_1, \tilde{\omega}_2\}$.

2.3 How do the dark and bright plasmonic modes decay in a metallic nanoparticle dimer?

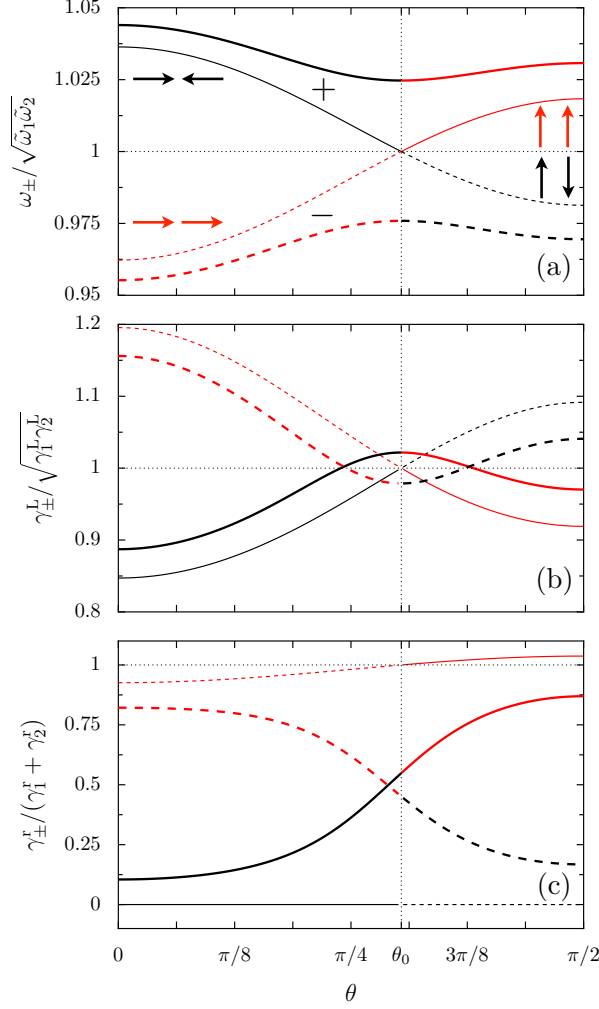


Figure 2.5: (a) Frequencies ω_{\pm} , (b) Landau damping linewidths γ_{\pm}^L and (c) radiative damping linewidths γ_{\pm}^R of the + (solid lines) and - (dashed lines) coupled plasmonic modes as a function of the polarization angle θ for $\tilde{\omega}_1/\tilde{\omega}_2 = 1$ (thin lines) and $\tilde{\omega}_1/\tilde{\omega}_2 = 1.05$ (thick lines). The bright (dark) modes for which the two localized surface plasmons are in phase (in anti-phase) are represented by red/gray (black) curves. In the figure, the parameters are $a_1 = a_2 = a$, $d = 3a$, $\hbar\tilde{\omega}_1/E_F^{(1)} = 1$, and spill-out is neglected.

where $E_F^{(n)}$ ($v_F^{(n)}$) stands for the Fermi energy (velocity) in nanoparticle n . Using the semiclassical leading order form [4] of $\rho_l^{(n)}$, the Landau damping decay rates read [172]

$$\gamma_{\pm}^L = \sum_{n=1}^2 \frac{3v_F^{(n)}}{4a_n} \left(\frac{\omega_n}{\omega_{\pm}}\right)^3 g\left(\frac{\hbar\omega_{\pm}}{E_F^{(n)}}\right) \Delta u_{n,\pm}^2, \quad (2.31)$$

where an explicit expression of the function g can be found in Refs. [30, 149], thus yielding an analytical expression for the Landau damping decay rates.

The linewidths from Eq. (2.31) are represented as a function of the polarization angle θ in Fig. 2.5(b) for the case $\tilde{\omega}_1/\tilde{\omega}_2 = 1$ (thin lines) and $\tilde{\omega}_1/\tilde{\omega}_2 = 1.05$ (thick lines). The dark (black) and bright modes (red/gray lines) show a modulation with respect to the Landau damping linewidth of isolated nanoparticles $\gamma_n^L = 3v_F^{(n)}g(\hbar\omega_n/E_F^{(n)})/4a_n$ (used as normalization). This anisotropy represents a qualitative difference as compared to the single nanoparticle case, stemming from the nonlocality of the coupled plasmonic modes. The expected tunability of $\pm 20\%$ obtained for $d = 3a$ [Fig. 2.5(b)] should be detectable in optical experiments for the bright mode. When $\tilde{\omega}_1/\tilde{\omega}_2 = 1$, the higher energy + mode is less damped than the lower-energy – one. This energy dependence is analogous to the single nanoparticle case, where higher mode frequencies correspond to lower values of the damping rates [8].

2.3.4 Absorption and radiation losses

In order to assess the relevance of Landau damping, we have to quantify the additional damping mechanisms not described by the Hamiltonian (2.19). The absorption losses given by the bulk conductivity of the metal lead to a size-independent decay rate γ^a (which has a weak frequency dependence). The radiation damping rate γ_{\pm}^r relates the power P_{\pm}^r radiated with the energy E_{\pm} stored in the mode \pm as

$$P_{\pm}^r = \gamma_{\pm}^r E_{\pm}. \quad (2.32)$$

In the limit where the interparticle distance is much smaller than the wavelength associated with each localized plasmon [173], one has $P_{\pm}^r = 2\omega_{\pm}^4 p_{\pm}^2 / 3c^3$, where p_{\pm} is the dipole moment corresponding to the \pm mode oscillating at the frequency ω_{\pm} given by Eq. (2.26). Averaging Eq. (2.32) on a period $2\pi/\omega_{\pm}$ much shorter than the decay time $1/\gamma_{\pm}^r$ leads to

$$\gamma_{\pm}^r = \frac{2\omega_{\pm}^3}{3c^3} \left(\sum_{n=1}^2 \sqrt{\tilde{\omega}_n a_n^3} \Delta u_{n,\pm} \right)^2. \quad (2.33)$$

The radiation damping linewidths above are shown in Fig. 2.5(c) as a function of polarization for $\tilde{\omega}_1/\tilde{\omega}_2 = 1$ (thin lines) and $\tilde{\omega}_1/\tilde{\omega}_2 = 1.05$ (thick lines). The normalization factor $\gamma_1^r + \gamma_2^r$ used in the figure corresponds to the radiation damping of two independent nanoparticles, with $\gamma_n^r = 2\tilde{\omega}_n^4 a_n^3 / 3c^3$. For $\tilde{\omega}_1/\tilde{\omega}_2 = 1$, the dark mode has a vanishing radiative linewidth [thin black curve in Fig. 2.5(c)] as it does not couple to the electromagnetic field, while the radiation damping of the bright mode can be modulated with the light polarization (thin red/gray curve). Choosing $\tilde{\omega}_1/\tilde{\omega}_2 \neq 1$ opens the way to the optical detection of the dark mode, as its linewidth becomes finite [thick black curve in Fig. 2.5(c)].

2.3.5 Discussion

The relative importance of the three above-described damping mechanisms, as well as those arising from the nature of the embedding matrix (chemical interface damping and conduction band in the matrix [92]) depends on a variety of physical parameters that should be settled in order to achieve a meaningful comparison. We focus from now on on noble metal nanoparticles,² since they constitute the dimers experimentally studied [152–158]. We show in Fig.

² The Mie frequency described after Eq. (2.20), depending on the dielectric constants inside and outside the nanoparticle, provides in general a good approximation to the experimentally obtained values (though deviations may appear in the presence of interband transitions close to the resonance frequency). The

2.3 How do the dark and bright plasmonic modes decay in a metallic nanoparticle dimer?

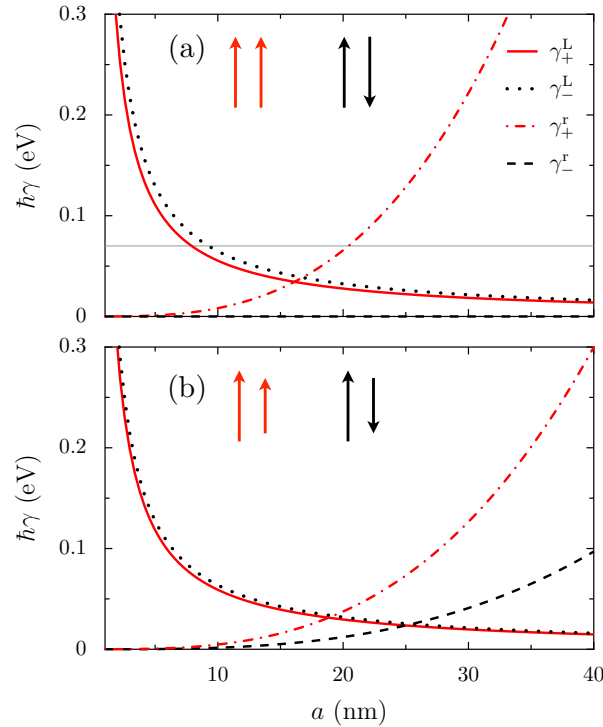


Figure 2.6: Landau damping (solid and dotted lines) and radiation damping (dashed and dashed-dotted lines) linewidths for transverse polarization $\theta = \pi/2$ as a function of nanoparticle radius a of the bright (+, light gray/red lines) and dark (–, black lines) mode. (a) Homogeneous dimer composed of two Ag nanoparticles. The thin gray line in the figure corresponds to the absorption losses measured in Ref. [174]. (b) Heterogeneous Ag-Au dimer. In the figure, $d = 3a$ and $\epsilon_m = 4$.

2.6 the competition of γ_{\pm}^L and γ_{\pm}^R of the bright (light gray/red lines) and dark (black lines) plasmonic modes as a function of nanoparticle radius a (assumed to be the same for both particles) for homogeneous [Ag-Ag, Fig. 2.6(a)] and heterogeneous [Ag-Au, Fig. 2.6(b)] dimers with $d = 3a$. A matrix with $\epsilon_m = 4$ is assumed, which leads to localized surface plasmon resonances $\omega_{\text{Ag}} = 2.6 \text{ eV}/\hbar$ and $\omega_{\text{Au}} = 2.2 \text{ eV}/\hbar$ [92]. We consider the transverse polarization ($\theta = \pi/2$), so that the + (–) mode corresponds to the bright (dark) mode (see Fig. 2.5). As can be seen from Fig. 2.6(a), for the bright mode the Landau damping [Eq. (2.31) scaling with the nanoparticle size as $1/a$, solid line] dominates over radiation damping [Eq. (2.33) scaling as a^3 , dashed-dotted line] for $a \lesssim 15 \text{ nm}$. On the contrary, for the dark mode, Landau damping [dotted line in Fig. 2.6(a)] dominates for sizes up to which it becomes negligible as compared to the absorption losses, since the radiative contribution to the linewidth vanishes [see dashed line in Fig. 2.6(a)]. In the case of a heterogeneous dimer [Fig. 2.6(b)], the difference between the bright and dark plasmonic modes is less stringent, as the dark mode acquires a finite dipole moment due to the difference in sizes and/or in densities between the two nanoparticles.

precise value of the Landau damping rate in noble metals is difficult to determine since in the case of very small nanoparticles, it depends on the softness of the self-consistent confining potential. This is due to the dielectric mismatch at the nanoparticle boundary, see Ref. [5].

The agreement of our analytical theory with microscopic numerical calculations [164] is excellent. Using the time-dependent local-density approximation for Ag dimers with $a = 1.2\text{ nm}$, $d = 3a$ and $\theta = 0$, a resonance linewidth of 0.43 eV is obtained, while the Landau damping mechanism, dominating in this regime, yields [Eq. (2.31)] $\hbar\gamma_{\pm}^L = 0.46\text{ eV}$.

The existing experimental data exhibit tendencies that are consistent with our theoretical calculations. In Ag dimers excited by EELS [157] the bright and dark modes have both an increasing damping rate when passing from homogeneous to heterogeneous dimers, due to the larger dipole moments of the latter and the fact that the inhomogeneous dimers are achieved by using larger nanoparticles. Homogeneous dimers with $a = 12\text{ nm}$ have a larger damping rate for the bright mode than for the dark one, due to the radiation damping contribution on the former. However, a quantitative comparison of the damping rates is handicapped by the limited resolution ($\sim 0.2\text{ eV}$) of these EELS experiments.³ Another difficulty for the quantitative comparison with the experiment is that the employed nanoparticles are very close to each other, taking the setup outside the validity of the dipole-dipole approximation used in our theoretical approach. Moreover, the absorption losses, estimated [174] to be about $\hbar\gamma^a \simeq 70\text{ meV}$ in optically excited Ag nanoparticles [see the thin gray line in Fig. 2.6(a)], are expected to be considerably larger in EELS experiments. This is due to the strong heating induced by the electron beam that might explain the value of the observed [157] total linewidths ($\sim 0.5\text{ eV}$). In addition, the nature and dielectric properties of the material coating the nanoparticles are not well controlled.

2.3.6 Concluding remarks

In conclusion, we have presented in this section a general quantum theory of coupled plasmonic modes in a heterogeneous metallic nanoparticle dimer. We have provided analytical expressions for the frequencies, Landau damping and radiative linewidths of these plasmonic modes. The role of nonradiative damping for collective excitations of interacting metallic nanoparticles has been explored and quantified. In particular, we have shown that the Landau damping is an unavoidable decay channel that can be dominant for the dark plasmonic mode consistent with the tendencies of the experimentally-observed linewidths [156–158]. At the experimental level, this should motivate systematic measurements for different particle sizes.

The work presented in this section constitutes a first step of crucial importance towards the understanding of the damping mechanisms limiting plasmon propagation in technologically promising quantum metamaterials [176] based on one- and two-dimensional arrays of nanoparticles [90], such as the honeycomb lattice supporting chiral massless Dirac-like plasmons that we have discussed in Sec. 2.2. Preliminary results towards this direction seem to indicate the preponderant role of Landau damping for short-wavelength modes in nanoparticle chains [177].

2.4 Coupling of collective plasmons to light: plasmon polaritons

Understanding how the collective Dirac plasmons sustained by a honeycomb array of metallic nanoparticles couple to light is of crucial interest, since the latter is, besides EELS, one of the possible mean of exciting such collective modes. This constitutes in fact quite a challenging problem to solve due to the inherent three-dimensional nature of light which couples

³ Notice that a considerably higher resolution (10 meV) within the EELS technique has been recently reported on in Ref. [175].

to quantum-mechanical collective modes that are two-dimensional by essence. In this section, we thus study the somewhat simpler problem of a three-dimensional array of metallic nanoparticles, which represents a first step towards the understanding of the regime of strong light-matter interaction in plasmonic arrays of nanoparticles.

The optical response of plasmonic metamaterials is determined by their dielectric function, which results in the reflection and transmission coefficients. In order to calculate the dielectric function it is crucial to identify the eigenmodes responsible for transporting electromagnetic radiation in arrays of metallic nanoparticles. These modes, stemming from the coupling between light and plasmons, have been extensively investigated in one- and two-dimensional nanoparticle arrays in the weak coupling regime [104–115], where the semiclassical theory of radiation provides a satisfactory description of the optical properties. In contrast, it is well established [178,179] that this semiclassical picture is inadequate for studying the fundamental nature of absorption processes in periodic systems that require a full quantum treatment of the strong coupling regime between light and matter, taking into account the conservation of crystal momentum between photons and polarization fields. This treatment gives rise to new quasiparticles — termed polaritons — that were first studied in the late 1950’s by Fano [178] and Hopfield [179] in the context of excitons in bulk solids. Polaritons are coherent superpositions of light and matter quantum fields and represent the natural quasiparticles involved in absorption processes in periodic systems. In the light of this analysis, the exploration of three-dimensional arrays of interacting metallic nanoparticles thus requires a full quantum analysis of the strong coupling regime between photons and collective plasmons that is expected to give rise to *plasmon polaritons*. This is the purpose of the present section.

As a proof of concept, we hence explore plasmon polaritons in a simple cubic array of metallic nanoparticles. By means of a fully quantum-mechanical approach, we analytically unveil the plasmon polariton band structure, modelling the localized surface plasmon in each nanoparticle as a point dipole interacting with the neighboring ones through a near-field interaction, as we did in Secs. 2.2 and 2.3. Such an interaction results in a plasmon polariton band structure that is highly tunable with the polarization of light, giving rise to dramatic effects which would otherwise be absent in noninteracting systems. Remarkably, we show that the plasmon polariton band gap can be tuned by about 50% by changing the plasmon polarization. Our prediction should thus be clearly observable in the frequency- and wavevector-dependent dielectric function of the metamaterial, resulting in an *interaction-driven birefringence* despite the symmetric lattice structure of the array. Our analytical treatment can be easily generalized to other three-dimensional lattices that are thus expected to exhibit a similar tunable optical response. Our theoretical proposal could be experimentally realized in self-organized arrays of metallic nanoparticles capped with molecular linkers such as thiol chains [37] and DNA [180].

2.4.1 Arrays of interacting metallic nanoparticles

We consider an ensemble of identical spherical metallic nanoparticles of radius r and forming a simple cubic lattice with \mathcal{N} lattice sites and lattice constant a . Each nanoparticle supports a localized surface plasmon with Mie frequency ω_0 . The noninteracting part of the Hamiltonian describing the independent localized surface plasmons on the cubic lattice sites hence reads

$$H_0 = \sum_{\mathbf{R}} \left[\frac{\Pi^2(\mathbf{R})}{2M} + \frac{M}{2} \omega_0^2 h^2(\mathbf{R}) \right], \quad (2.34)$$

where $h(\mathbf{R})$ denotes the electronic center-of-mass displacement corresponding to a nanoparticle located at position \mathbf{R} , $\Pi(\mathbf{R})$ is the conjugated momentum to $h(\mathbf{R})$ and $M = N_e m_e$ is the total electronic mass per nanoparticle. The point dipole corresponding to each localized surface plasmon has thus a dipole moment $\mathbf{p} = -Qh(\mathbf{R})\hat{\mathbf{p}}$, with $\hat{\mathbf{p}}$ the unit vector indicating its direction and $Q = N_e e$ the total electronic charge.

Adopting the same model as in Sec. 2.2, i.e., localized surface plasmons interacting through their near field, the dipole-dipole interaction Hamiltonian reads

$$H_{\text{int}} = \frac{Q^2}{8\pi\epsilon_0 a^3} \sum_{\mathbf{R}} \sum_{j=1}^3 \mathcal{C}_j h(\mathbf{R}) [h(\mathbf{R} + \mathbf{e}_j) + h(\mathbf{R} - \mathbf{e}_j)], \quad (2.35)$$

with

$$\mathcal{C}_j = 1 - 3 [\sin^2 \theta (\delta_{j1} \cos^2 \varphi + \delta_{j2} \sin^2 \varphi) + \delta_{j3} \cos^2 \theta] \quad (2.36)$$

and where $\mathbf{e}_1 = a\hat{\mathbf{x}}$, $\mathbf{e}_2 = a\hat{\mathbf{y}}$ and $\mathbf{e}_3 = a\hat{\mathbf{z}}$ are the vectors joining nearest neighboring nanoparticles on the simple cubic lattice. Only interactions between nearest neighbors are taken into account in the Hamiltonian (2.35) since, as detailed in Ref. [29], the interactions beyond nearest neighbors do not qualitatively change the collective plasmon dispersion, as is also the case for metallic nanoparticle arrays with other geometries, such as the linear chain [111] or the honeycomb lattice (see Sec. 2.2 and Ref. [26]).

2.4.2 Collective plasmon dispersion

Introducing the bosonic operator

$$b_{\mathbf{R}} = \sqrt{\frac{M\omega_0}{2\hbar}} h(\mathbf{R}) + i \frac{\Pi(\mathbf{R})}{\sqrt{2M\hbar\omega_0}} \quad (2.37)$$

which annihilates a localized surface plasmon at lattice site \mathbf{R} and its momentum space representation $b_{\mathbf{q}}$ through $b_{\mathbf{R}} = \mathcal{N}^{-1/2} \sum_{\mathbf{q}} \exp(i\mathbf{q} \cdot \mathbf{R}) b_{\mathbf{q}}$, the Hamiltonian representing the collective plasmons,

$$H_{\text{pl}} = H_0 + H_{\text{int}}, \quad (2.38)$$

with H_0 and H_{int} defined in (2.34) and (2.35), respectively, transforms into

$$H_{\text{pl}} = \hbar \sum_{\mathbf{q}} \left[(\omega_0 + 2\Omega f_{\mathbf{q}}) b_{\mathbf{q}}^\dagger b_{\mathbf{q}} + \Omega f_{\mathbf{q}} (b_{\mathbf{q}}^\dagger b_{-\mathbf{q}}^\dagger + b_{-\mathbf{q}} b_{\mathbf{q}}) \right], \quad (2.39)$$

with $\Omega = \omega_0(r/a)^3/2 \ll \omega_0$ and

$$f_{\mathbf{q}} = \sum_{j=1}^3 \mathcal{C}_j \cos(\mathbf{q} \cdot \mathbf{e}_j). \quad (2.40)$$

As in Sec. 2.2, the purely plasmonic problem represented by the Hamiltonian (2.39) can be diagonalized by a Bogoliubov transformation. The introduction of the new bosonic operators

$$\beta_{\mathbf{q}} = \cosh \vartheta_{\mathbf{q}} b_{\mathbf{q}} - \sinh \vartheta_{\mathbf{q}} b_{-\mathbf{q}}^\dagger, \quad (2.41)$$

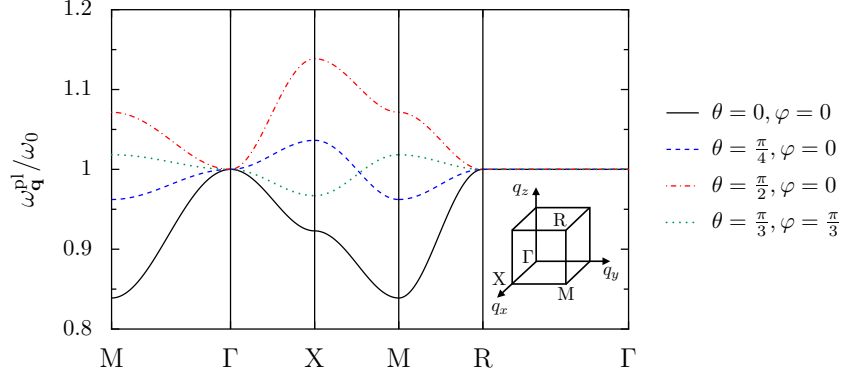


Figure 2.7: Collective plasmon dispersion relation (2.45) along the high symmetry axes in the first Brillouin zone, for various polarization angles (θ, φ) . In the figure, $a = 3r$. The inset shows one eighth of the cubic first Brillouin zone together with the high symmetry points.

with

$$\cosh \vartheta_{\mathbf{q}} = \frac{1}{\sqrt{2}} \left(\frac{1 + 2\Omega f_{\mathbf{q}}/\omega_0}{\sqrt{1 + 4\Omega f_{\mathbf{q}}/\omega_0}} + 1 \right)^{1/2}, \quad (2.42)$$

$$\sinh \vartheta_{\mathbf{q}} = -\frac{\text{sign}(f_{\mathbf{q}})}{\sqrt{2}} \left(\frac{1 + 2\Omega f_{\mathbf{q}}/\omega_0}{\sqrt{1 + 4\Omega f_{\mathbf{q}}/\omega_0}} - 1 \right)^{1/2}, \quad (2.43)$$

leads to

$$H_{\text{pl}} = \sum_{\mathbf{q}} \hbar \omega_{\mathbf{q}}^{\text{pl}} \beta_{\mathbf{q}}^{\dagger} \beta_{\mathbf{q}}, \quad (2.44)$$

with the collective plasmon dispersion

$$\omega_{\mathbf{q}}^{\text{pl}} = \omega_0 \sqrt{1 + 4 \frac{\Omega}{\omega_0} f_{\mathbf{q}}}. \quad (2.45)$$

It is important to realize that the dispersion (2.45) can be tuned by the polarization of the localized surface plasmons which enters the function $f_{\mathbf{q}}$ in (2.40). This is illustrated in Fig. 2.7 which shows the collective plasmon dispersion (2.45) along the high symmetry axes in the first Brillouin zone. As can be seen from the figure, the collective plasmon dispersion can be dramatically changed by the polarization of the localized surface plasmons. As will be shown in Sec. 2.4.4, this feature is at the very heart of the tunability of the polaritonic band gap, of the dielectric function and thus of the resulting reflection and transmission coefficients of the metamaterial with the polarization of light.

2.4.3 Coupling to light

The collective plasmons discussed above can be triggered by light. As realized by Fano [178] and Hopfield [179], an adequate description of the strong coupling of elementary excitations to light in periodic systems can be achieved by quantizing electromagnetic modes in a cavity that

has the same size as the crystal. This is a direct consequence of the translational invariance of the nanoparticle array and the subsequent conservation of photonic and plasmonic crystal momenta. As a result, energy oscillates back and forth between the two subsystems, such that the semiclassical view of absorption processes is not appropriate. Hence, we describe the photonic modes in the cavity of volume $\mathcal{V} = \mathcal{N}a^3$ by the Hamiltonian

$$H_{\text{ph}} = \sum_{\mathbf{q}} \hbar\omega_{\mathbf{q}}^{\text{ph}} c_{\mathbf{q}}^{\dagger} c_{\mathbf{q}}, \quad (2.46)$$

where $c_{\mathbf{q}}$ ($c_{\mathbf{q}}^{\dagger}$) annihilates (creates) a photon with momentum \mathbf{q} and transverse polarization $\hat{\epsilon}$ ($\mathbf{q} \cdot \hat{\epsilon} = 0$) and where $\omega_{\mathbf{q}}^{\text{ph}} = c|\mathbf{q}|$ is the photon dispersion with c the speed of light [181]. Notice that in (2.46), the summation over photon polarizations has been made implicit in order to simplify the notation in the sequel of the paper.

In the long-wavelength limit (dipolar approximation), the localized surface plasmons interact with the light modes through the Hamiltonian

$$H_{\text{pl-ph}} = \sum_{\mathbf{R}} \left[\frac{Q}{M} \boldsymbol{\Pi}(\mathbf{R}) \cdot \mathbf{A}(\mathbf{R}) + \frac{Q^2}{2M} \mathbf{A}^2(\mathbf{R}) \right], \quad (2.47)$$

where

$$\mathbf{A}(\mathbf{R}) = \sum_{\mathbf{q}} \hat{\epsilon} \sqrt{\frac{\hbar}{2\epsilon_0 \mathcal{V} \omega_{\mathbf{q}}^{\text{ph}}}} \left(c_{\mathbf{q}} e^{i\mathbf{q} \cdot \mathbf{R}} + c_{\mathbf{q}}^{\dagger} e^{-i\mathbf{q} \cdot \mathbf{R}} \right) \quad (2.48)$$

is the vector potential at the location \mathbf{R} of the nanoparticles. Expressing the conjugate momentum $\boldsymbol{\Pi}(\mathbf{R}) = \Pi(\mathbf{R})\hat{\mathbf{p}}$ in (2.48) in terms of the creation and annihilation operators associated with localized surface plasmons [see Eq. (2.37)], going to Fourier space and using $\hat{\mathbf{p}} \cdot \hat{\epsilon} = 1$, we obtain for (2.47) the expression

$$H_{\text{pl-ph}} = \hbar\omega_0 \sum_{\mathbf{q}} \left[i\xi_{\mathbf{q}} \left(b_{\mathbf{q}}^{\dagger} c_{\mathbf{q}} - c_{\mathbf{q}}^{\dagger} b_{\mathbf{q}} + b_{\mathbf{q}}^{\dagger} c_{-\mathbf{q}}^{\dagger} - c_{-\mathbf{q}} b_{\mathbf{q}} \right) + \xi_{\mathbf{q}}^2 \left(c_{\mathbf{q}}^{\dagger} c_{\mathbf{q}} + c_{\mathbf{q}} c_{\mathbf{q}}^{\dagger} + c_{\mathbf{q}}^{\dagger} c_{-\mathbf{q}}^{\dagger} + c_{-\mathbf{q}} c_{\mathbf{q}} \right) \right], \quad (2.49)$$

with $\xi_{\mathbf{q}} = (\pi\omega_0/\omega_{\mathbf{q}}^{\text{ph}})^{1/2}(r/a)^{3/2}$. In terms of the Bogoliubov modes (2.41) diagonalizing the purely plasmonic problem, and using the inverse transform $b_{\mathbf{q}} = \cosh \vartheta_{\mathbf{q}} \beta_{\mathbf{q}} + \sinh \vartheta_{\mathbf{q}} \beta_{-\mathbf{q}}^{\dagger}$, equation (2.49) thus reads

$$H_{\text{pl-ph}} = \hbar\omega_0 \sum_{\mathbf{q}} \left[i\xi_{\mathbf{q}} (\cosh \vartheta_{\mathbf{q}} - \sinh \vartheta_{\mathbf{q}}) \left(\beta_{\mathbf{q}}^{\dagger} c_{\mathbf{q}} - c_{\mathbf{q}}^{\dagger} \beta_{\mathbf{q}} + \beta_{\mathbf{q}}^{\dagger} c_{-\mathbf{q}}^{\dagger} - c_{-\mathbf{q}} \beta_{\mathbf{q}} \right) + \xi_{\mathbf{q}}^2 \left(c_{\mathbf{q}}^{\dagger} c_{\mathbf{q}} + c_{\mathbf{q}} c_{\mathbf{q}}^{\dagger} + c_{\mathbf{q}}^{\dagger} c_{-\mathbf{q}}^{\dagger} + c_{-\mathbf{q}} c_{\mathbf{q}} \right) \right]. \quad (2.50)$$

2.4.4 Plasmon polariton dispersion

The total Hamiltonian

$$H = H_{\text{pl}} + H_{\text{ph}} + H_{\text{pl-ph}} \quad (2.51)$$

with H_{pl} , H_{ph} and $H_{\text{pl-ph}}$ given, respectively, in (2.44), (2.46) and (2.50), can now be diagonalized by introducing the annihilation operator associated with plasmon polaritons

$$\gamma_{\mathbf{q}} = w_{\mathbf{q}} c_{\mathbf{q}} + x_{\mathbf{q}} \beta_{\mathbf{q}} + y_{\mathbf{q}} c_{-\mathbf{q}}^{\dagger} + z_{\mathbf{q}} \beta_{-\mathbf{q}}^{\dagger}, \quad (2.52)$$

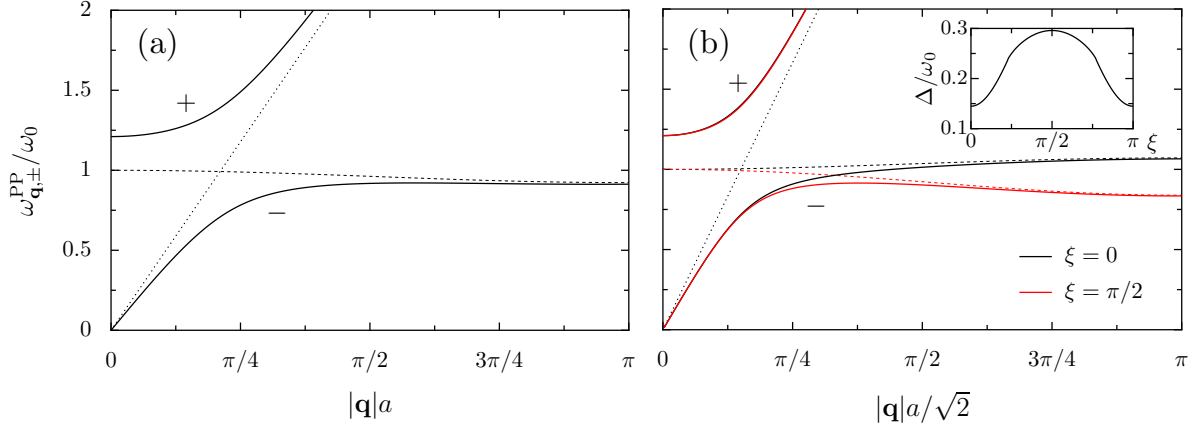


Figure 2.8: Solid lines: plasmon polariton dispersion (2.54) along (a) the ΓX and (b) the ΓM direction in the first Brillouin zone (see the inset in Fig. 2.7), (a) for any transverse light polarization and (b) for two transverse light polarizations characterized by the angle ξ (see text). Dotted line: dispersion $\omega_{\mathbf{q}}^{\text{pl}}$ of free light. Dashed line: collective plasmon dispersion (2.45). Inset: polaritonic band gap as a function of polarization angle. In the figure, $a = 3r$ and $c/\omega_0 = 3a/2$.

with $w_{\mathbf{q}}$, $x_{\mathbf{q}}$, $y_{\mathbf{q}}$ and $z_{\mathbf{q}}$ complex numbers. As detailed in Ref. [29], imposing the diagonal form of the Heisenberg equation of motion $[\gamma_{\mathbf{q}}, H] = \hbar\omega_{\mathbf{q}}^{\text{PP}}\gamma_{\mathbf{q}}$ yields the frequency- and wavevector-dependent dielectric function

$$\epsilon(\mathbf{q}, \omega) = \frac{c^2 \mathbf{q}^2}{\omega^2} = 1 + \frac{8\pi\Omega\omega_0}{\omega_{\mathbf{q}}^{\text{pl}2} - \omega^2}. \quad (2.53)$$

The spatial dispersion of the dielectric function (i.e., its dependence on \mathbf{q}) stems from the interaction between localized surface plasmons leading to the plasmonic dispersion $\omega_{\mathbf{q}}^{\text{pl}}$ in our system. This is reminiscent of the case of exciton polaritons in bulk semiconductors [182]. A crucial difference of our system, however, is that the dielectric function of the metamaterial in Eq. (2.53) is strongly sensitive to the polarization of incoming light, which quantitatively affects the collective plasmon dispersion $\omega_{\mathbf{q}}^{\text{pl}}$. This effect is a direct consequence of the anisotropic dipolar interaction between the metallic nanoparticles, resulting in a birefringence of the plasmonic metamaterial despite the symmetric lattice structure of our array. This is in stark contrast with conventional birefringence observed in crystals, which is usually associated with strongly asymmetric lattice structures [88].

The dielectric function (2.53) results in the plasmon polariton dispersion

$$\omega_{\mathbf{q},\pm}^{\text{PP}} = \frac{1}{\sqrt{2}} \left[\omega_{\mathbf{q}}^{\text{pl}2} + \omega_{\mathbf{q}}^{\text{ph}2} + 8\pi\Omega\omega_0 \pm \sqrt{\left(\omega_{\mathbf{q}}^{\text{pl}2} + \omega_{\mathbf{q}}^{\text{ph}2} + 8\pi\Omega\omega_0 \right)^2 - 4\omega_{\mathbf{q}}^{\text{pl}2}\omega_{\mathbf{q}}^{\text{ph}2}} \right]^{1/2} \quad (2.54)$$

which is shown in Fig. 2.8(a) along the ΓX direction in the first Brillouin zone for transverse light polarization (i.e., in the yz plane, see the inset in Fig. 2.7). For wavenumbers close to the edge of the first Brillouin zone, the $+$ and $-$ branches of the plasmon polariton dispersion (2.54) asymptotically approach the light and the collective plasmon dispersion, respectively.

When $|\mathbf{q}| \rightarrow 0$, however, the $-$ branch goes to $\omega_{\mathbf{q}}^{\text{ph}} \rightarrow 0$, while the $+$ branch tends to $\omega_{|\mathbf{q}| \rightarrow 0,+}^{\text{PP}} \simeq \omega_0(1 + 8\pi\Omega/\omega_0)^{1/2}$. Thus the strong plasmon-photon coupling results in a gap of the order of $\Delta \simeq 4\pi\Omega$ in the plasmon polariton dispersion. This has important consequences on the optical properties of our simple cubic array of nanoparticles. Indeed, for frequencies within the band gap, no plasmon polariton can propagate in the metamaterial, such that the reflectivity of the latter is equal to one. We estimate that for an interparticle distance $a = 3r$, the polaritonic gap Δ is about 25 % of the Mie frequency ω_0 . For noble-metal nanoparticles, the latter usually lies in the visible range ($\omega_0 \simeq 2 - 3 \text{ eV}/\hbar$), yielding a polaritonic gap of about $\Delta \simeq 0.5 - 0.75 \text{ eV}/\hbar$.

Remarkably, the plasmon polariton dispersion (2.54) can be tuned by the polarization of light through the modification of the collective plasmon dispersion (2.45) (see Fig. 2.7). This is illustrated in Fig. 2.8(b), which shows the plasmon polariton dispersion along the ΓM direction in the first Brillouin zone (see the inset in Fig. 2.7) for two polarization angles ξ defined through the transverse polarization $\hat{\mathbf{e}} = \cos\xi \hat{\mathbf{e}}_1 + \sin\xi \hat{\mathbf{e}}_2$, with $\hat{\mathbf{e}}_1 = \hat{\mathbf{z}} \times \hat{\mathbf{q}}/|\hat{\mathbf{z}} \times \hat{\mathbf{q}}|$ and $\hat{\mathbf{e}}_2 = \hat{\mathbf{q}} \times \hat{\mathbf{e}}_1/|\hat{\mathbf{q}} \times \hat{\mathbf{e}}_1|$. As can be seen from Fig. 2.8(b), the $-$ branch of the plasmon polariton is significantly modulated by the polarization of light. This effect results from the dependence on polarization of the collective plasmon dispersion (dashed lines in the figure). Consequently, the polaritonic band gap, defined as $\Delta = \omega_{|\mathbf{q}|=0,+}^{\text{PP}} - \max(\omega_{\mathbf{q},-}^{\text{PP}})$, can be significantly modulated (by about 50 %) by tilting the polarization of light, as shown in the inset of Fig. 2.8(b). Considering the amplitude of the effect, this feature should be clearly measurable in an experiment. Thus the dielectric function of the metamaterial in (2.53) is strongly sensitive to the polarization of incoming light. This effect is a direct consequence of the anisotropic dipolar interaction between the metallic nanoparticles, resulting in a birefringence of the plasmonic metamaterial despite the symmetric lattice structure of our array. This is in stark contrast with conventional birefringence observed in crystals, which is usually associated with strongly asymmetric lattice structures [88].

2.4.5 Concluding remarks

We have developed in this section an analytical quantum theory of the strong coupling regime between photons and collective plasmons in three-dimensional arrays of interacting metallic nanoparticles. Remarkably, the resulting plasmon polaritons present a band structure that can be significantly modulated by the polarization of light. Such a tunability crucially stems from the dipolar interactions between the localized surface plasmons in each nanoparticle. As a result, the dielectric function and thus the reflection and transmission coefficients of the metamaterial can be tuned by changing the polarization of light. The consequent optical birefringence is directly due to the anisotropic dipolar interactions between nanoparticles despite the symmetric lattice structure of the metamaterial.

Our results obtained for a simple cubic array can be straightforwardly extended to other types of three-dimensional metastructures, such as bcc or fcc lattices of metallic nanoparticles for which the physics described in this section does not change qualitatively [183, 184]. The present study also constitutes a first relevant step towards the understanding of the strong-coupling regime between light and two-dimensional plasmonic modes, such as the Dirac-like plasmons in honeycomb arrays of metallic nanoparticles described in Sec. 2.2 [185].

2.5 Conclusion

Motivated by the fascinating electronic properties of (real) graphene, we have in the present chapter studied a plasmonic analogue of graphene, constituted by a periodic honeycomb array of metallic nanoparticles. In particular, we have shown that such an array sustains extended collective plasmonic modes that mimic the unusual properties of electrons in graphene. Indeed, such plasmons in fact represent chiral massless Dirac bosonic excitations, and thus inherit of the peculiar properties of electrons in graphene, for instance the absence of backscattering off impurities. Moreover, these Dirac-like plasmons are fully tunable with the polarization of light, opening interesting perspectives for manipulating light at subwavelength scales.

Though these modes are chiral and hence they do not suffer from backscattering, damping will inevitably limit their propagation. In order to understand the different damping mechanisms at work (Ohmic, radiative and Landau damping), we have considered nanoparticle dimers that constitute the building block of any larger metasurface. Specifically, we have shown that the Landau damping decay channel is an unavoidable mechanism for understanding the observed linewidth of coupled plasmonic modes, in particular when these are dark, i.e., immune to radiation damping. Our results will be extended in the near future to larger systems [172], in particular to the honeycomb array considered in this chapter, so as to fully understand the properties of chiral massless Dirac plasmons.

Of great interest is also how purely plasmonic modes couple to light, which is the usual mean of triggering such excitations, although the EELS technique has been recently successfully used as well. We have hence explored the strong coupling regime between plasmons and light in a three-dimensional (simple cubic) array of metallic nanoparticles. Interestingly, we have shown that the resulting plasmon polaritons can be tuned by the polarization of incoming light. It will be interesting in the future to investigate how light can be used to trigger the Dirac plasmons on the honeycomb array placed, e.g., in a cavity so as to achieve a strong light-matter coupling.

Related publications

- G. Weick, D. Weinmann
Lifetime of the surface magnetoplasmons in metallic nanoparticles
[Phys. Rev. B **83**, 125405 \(2011\)](#)
- G. Weick, C. Woollacott, W.L. Barnes, O. Hess, E. Mariani
Dirac-like plasmons in honeycomb lattices of metallic nanoparticles
[Phys. Rev. Lett. **110**, 106801 \(2013\)](#)
- E. Mariani, G. Weick
A plasmonic analogue of graphene
[SPIE Newsroom, DOI:10.1117/2.1201411.005673 \(2014\)](#)
- G. Weick, E. Mariani
Tunable plasmon polaritons in arrays of interacting metallic nanoparticles
[Eur. Phys. J. B **88**, 7 \(2015\)](#)
- A. Brandstetter-Kunc, G. Weick, D. Weinmann, R.A. Jalabert
Decay of dark and bright plasmonic modes in a metallic nanoparticle dimer
[Phys. Rev. B **91**, 035431 \(2015\)](#)

- T.J. Sturges, C. Woollacott, G. Weick, E. Mariani
Dirac plasmons in bipartite lattices of metallic nanoparticles
[2D Mater. 2, 014008 \(2015\)](#); focus issue on artificial graphene

Chapter 3

Parametric resonances in many-body fermionic systems

3.1 Introduction

The swing is the best known example of a classical system showing parametric resonances [186]. The periodic modulation of the effective swing length induced by the motion of legs leads to the exponential amplification of the oscillations if the modulation frequency is chosen commensurately with the natural frequency of the swing. Quantizing this classical problem as a harmonic oscillator with modulated parabolic confinement leads to the appearance of an exponential divergence in the time evolution of the bosonic raising and lowering operators [22]. This effect is particularly strong if the modulation is around twice the natural oscillator frequency.

In a modulated system of many bosonic oscillators only those fulfilling the resonance condition will be amplified, making parametric resonance a spectroscopic tool in many-body quantum systems. These ideas acquired particular relevance since cold atom systems in optical lattices have been realized [187]. As the intensity of the lattice can be fully controlled by the laser power one can study parametric modulations in correlated quantum systems with current experimental tools [188]. From the theoretical point of view, parametric amplification of Bogoliubov quasiparticles for bosonic clouds in optical lattices have been already investigated in the past [189, 190]. In these systems, the bosonic nature of quasiparticles appears already when interactions are treated at mean-field level, and allows for the amplification to occur.

In this chapter we analyze parametric resonances in many-body *fermionic* systems, starting with the very question whether the amplification can occur at all. Indeed, in contrast to the bosonic case, in fermionic systems any mean-field treatment of interactions, including the presence of broken symmetries, preserves the fermionic nature of quasiparticles. The Pauli principle thus blocks their amplification, as can be easily checked by direct calculation [22]. Then the question rises if bosonic collective excitations of a fermionic many-body system can be subject to amplification by modulating a parameter in the microscopic Hamiltonian.

In order to address this fundamental question we need to treat correlations in a fermionic system beyond mean-field level. In Sec. 3.2 we thus confine our investigation to one-dimensional (1D) correlated fermions within the Luttinger liquid picture, in which interactions are treated (almost) exactly and the system is naturally diagonalized in terms of collective bosonic spin and charge density waves [191–193].

Extending the ideas above to 2D and 3D many-body fermionic systems is a formidable theoretical challenge, as one needs to capture the relevant correlations by treating interactions beyond mean field, which is a very difficult and nontrivial task to achieve. In Sec. 3.3, we focus on the case of *confined* many-body fermionic systems, where collective modes exist due to the finite size of the system [167]. Examples of such collective modes are plasmon excitations which

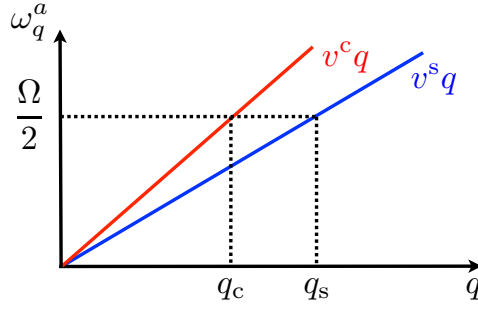


Figure 3.1: Sketch of the dispersions ω_q^a of the charge ($a = c$) and spin ($a = s$) density waves as a function of momentum q , with group velocities v^c and v^s , respectively. The pumping frequency Ω amplifies collective spin and charge modes in the vicinity of the momenta q_c and q_s .

correspond to the motion of the electronic center of mass in metallic nanoparticles [167] (see Chap. 2) and in quasi-two-dimensional semiconductor quantum dots [169, 194].

3.2 Parametric resonance in a one-dimensional interacting Fermi system

According to the Luttinger liquid theory, spin and charge collective modes in a 1D fermionic system disperse with two different group velocities, giving rise to the so-called spin-charge separation (see Fig. 3.1). This fundamental issue in condensed matter physics has been detected in transport experiments on quantum wires [195] and by angle-resolved photoemission spectroscopy of 1D SrCuO₂ [196] only recently. Due to their great tunability, cold atomic gases in optical lattices are also promising candidates for the experimental detection of spin-charge separation in 1D systems, as shown by several theoretical proposals [197–203].

In this section we show how a spatially homogeneous time-periodic modulation of the intensity of the optical lattice indeed leads to the amplification of charge and spin density waves of a 1D correlated cloud of ultracold fermionic atoms. If Ω is the modulation frequency, the charge and spin waves with energy $v^c q_c = v^s q_s = \Omega/2$ will be amplified (see Fig. 3.1). Due to the different group velocities v^c and v^s for the charge and spin channels, respectively, the resonant condition amplifies different wavenumbers for the two branches, q_c and q_s . On top of showing the feasibility of parametric amplification in correlated fermionic systems, we also propose this technique as a tool to systematically investigate the spin-charge separation in experiments. Indeed, we discuss the effect of the amplification above on the fermionic momentum distribution and show how the latter exhibits well defined shoulders directly related to the wavenumbers q_c and q_s . These structures are particularly evident after not too long modulation times. As the momentum distribution is the standard quantity measured in time-of-flight experiments on cold atomic clouds [187], our analysis has direct implications on investigations of correlated fermionic systems with current experimental tools.

3.2.1 Model

We consider interacting fermionic atoms with (pseudo-)spin 1/2 confined into 1D cigars (as, e.g., realized in optical lattices [187]), with a further periodic potential along the 1D axis. In order to obtain analytical results, we disregard trapping and finite size effects, as they will not qualitatively modify our results. The parametric excitation of the system is achieved by periodically modulating the intensity of the optical lattice along the 1D system, thereby shrinking the Wannier wavefunctions associated to each lattice site. This has the two-fold effect of modulating the hopping rate between neighboring sites (i.e., the kinetic energy) as well as the on-site repulsion for multiple occupancy. As the former is exponentially sensitive to the wavefunction overlap it is the dominant parametric modulation term in the problem and we will focus on this for simplicity.

Once translated into the Bloch-band language, and if we focus on the low-energy physics of the problem, the modulation in the kinetic term yields an effectively time-dependent Fermi velocity for the atoms close to the Fermi level, $v_F(t) = v_F + \delta v_F(t)$. Here $\delta v_F(t) = \eta v_F \sin(\Omega t)$, where v_F is the Fermi velocity at equilibrium (i.e., for times $t < 0$ before the modulation starts), and Ω and η are the frequency and intensity of the parametric modulation, respectively. Our focus on the low-energy sector of the many-body problem naturally suggests a Luttinger liquid approach [191–193] to the correlated system, which allows for an (almost) exact treatment of interactions. We thus linearize the single-particle spectrum in the vicinity of the Fermi level for momenta $||k| - k_F| < \Lambda$, with k_F the Fermi wavevector and Λ an ultraviolet cutoff. The time-dependent Hamiltonian describing the system of size L therefore reads¹

$$H(t) = v_F(t) \sum_{k\sigma\tau} f_{k\tau} c_{k\sigma\tau}^\dagger c_{k\sigma\tau} + \sum_{\substack{q \neq 0 \\ \tau\tau'\sigma\sigma'}} \frac{V_{\tau\tau',q}^{\sigma\sigma'}}{2L} \rho_{-q}^{\tau\sigma} \rho_q^{\tau'\sigma'} \quad (3.1)$$

with $f_{k\tau} = \tau k - k_F$. Here, $c_{k\sigma\tau}^\dagger$ ($c_{k\sigma\tau}$) creates (annihilates) a τ -moving fermion with momentum k and spin $\sigma = \uparrow, \downarrow$ [$\tau = 1$ (-1) corresponds to right (left) movers] while $\rho_q^{\tau\sigma} = \sum_k c_{k-q,\sigma,\tau}^\dagger c_{k,\sigma,\tau}$ is the corresponding fermionic density operator. In Eq. (3.1) we keep the general form of the interaction between fermionic densities with generic spin and branch indices. Within the standard Luttinger liquid theory we have $V_{\tau\tau,q}^{\sigma\sigma} = V_0^\parallel$, $V_{\tau\tau,q}^{\sigma,-\sigma} = V_0^\perp$, $V_{\tau,-\tau,q}^{\sigma\sigma} = V_0^\parallel - V_{2k_F}^\parallel$, $V_{\tau,-\tau,q}^{\sigma,-\sigma} = V_0^\perp$, where $V_q^{\parallel/\perp}$ is the Fourier transform of the microscopic interaction between fermions with parallel/antiparallel spins. This allows to treat short range interactions (like contact s -wave scattering for neutral fermions) where Pauli principle imposes $V_q^\parallel = 0$, as well as finite range spin-invariant ones (e.g., between charged fermions) with $V_q^\parallel = V_q^\perp$. Notice that Eq. (3.1) does not include backscattering between particles with opposite spins as well as umklapp scattering as those terms are usually negligible at equilibrium and away from half-filling [191, 192].

Introducing the bosonic operators for charge and spin density fluctuations

$$b_q^{c/s} = \sqrt{\frac{\pi}{L|q|}} \sum_{\tau} \Theta(\tau q) (\rho_q^{\tau\uparrow} \pm \rho_q^{\tau\downarrow}), \quad (3.2)$$

¹ In the remaining of Sec. 3.2, we set $\hbar = k_B = 1$.

Eq. (3.1) transforms into the separable Hamiltonian [191]

$$H(t) = \sum_{\substack{a=c,s \\ q \neq 0}} |q| \left[A_q^a(t) b_q^{a\dagger} b_q^a + B_q^a \left(b_q^{a\dagger} b_{-q}^{a\dagger} + b_{-q}^a b_q^a \right) \right], \quad (3.3)$$

with

$$A_q^{c/s}(t) = v_F(t) + \frac{V_0^{\parallel} \pm V_0^{\perp}}{2\pi}, \quad B_q^{c/s} = \frac{V_0^{\parallel} \pm V_0^{\perp} - V_{2k_F}^{\parallel}}{4\pi}. \quad (3.4)$$

The time-independent part in Eq. (3.3) can be diagonalized by means of the Bogoliubov transformation $b_q^a = \cosh \varphi_q^a \beta_q^a + \sinh \varphi_q^a \beta_{-q}^{a\dagger}$ in terms of the bosonic fields β_q^a , such that

$$H(t) = \sum_{a,q \neq 0} \left[(\omega_q^a + \delta v_F(t) |q| \cosh(2\varphi_q^a)) \beta_q^{a\dagger} \beta_q^a + \frac{\delta v_F(t)}{2} |q| \sinh(2\varphi_q^a) \left(\beta_q^{a\dagger} \beta_{-q}^{a\dagger} + \beta_{-q}^a \beta_q^a \right) \right] \quad (3.5)$$

with $\omega_q^a = v_q^a |q|$. The different charge and spin group velocities are $v_q^a = [A_q^a(0)^2 - 4B_q^{a2}]^{1/2}$. For short range interactions, one can neglect the momentum dependence of the group velocities such that $v_q^a \simeq v^a$, and the dispersion of the spin and charge density waves is linear (see Fig. 3.1). The coefficients of the Bogoliubov transformation read $\sinh \varphi_q^{c/s} = \mp [A_q^{c/s}(0)/2v_q^{c/s} - 1/2]^{1/2}$ and $\cosh \varphi_q^{c/s} = [A_q^{c/s}(0)/2v_q^{c/s} + 1/2]^{1/2}$.

The crucial point to notice at this level is that the parametric modulation introduces a time-dependent anomalous term in the Hamiltonian (3.5), creating and annihilating pairs of bosonic charge and spin density waves. As the modulation is homogeneous in space (i.e., at zero wavenumber), the new terms create or annihilate pairs of excitations with opposite wavenumber, as requested by momentum conservation [190]. In addition, the induced anomalous terms are proportional to $\sinh(2\varphi_q^a)$ and thus correctly vanish in the non-interacting limit $V_q^{\parallel/\perp} = 0$, where fermionicity forbids parametric amplification.

3.2.2 Parametric amplification

From the Hamiltonian (3.5) above, the time evolution of the operators β_q^a can now be easily obtained [18], showing that indeed parametric amplification of collective bosonic modes in a fermionic system is possible. With Eq. (3.5), we obtain from the Heisenberg equation of motion for the operator β_q^a in the limit of weak parametric modulation ($\eta \ll 1$) and retaining only slow terms near the resonance (rotating wave approximation, i.e., for Ω in the vicinity of $2\omega_q^a$) the time evolution

$$\beta_q^a(t) = \sum_{\alpha=\pm} \alpha e^{i(\omega_{q\alpha}^a - \omega_q^a)t} \left[\bar{\omega}_{q,-\alpha}^a \beta_q^a(0) + i \bar{\xi}_q^a \beta_{-q}^{a\dagger}(0) \right], \quad (3.6)$$

where

$$\omega_{q\pm}^a = \omega_q^a - \frac{\Omega}{2} \pm \sqrt{\left(\omega_q^a - \frac{\Omega}{2} \right)^2 - \xi_q^{a2}}. \quad (3.7)$$

In Eq. (3.6), we defined $\bar{\omega}_{q\pm}^a = \omega_{q\pm}^a / (\omega_{q-}^a - \omega_{q+}^a)$ and $\bar{\xi}_q^a = \xi_q^a / (\omega_{q-}^a - \omega_{q+}^a)$, with $\xi_q^a = \eta v_F |q| \sinh(2\varphi_q^a)/2$. Thus, in a narrow ‘‘resonant window’’ of energy $|\omega_q^a - \Omega/2| < |\xi_q^a|$, the

frequencies $\omega_{q\pm}^a$ acquire an imaginary part, leading to the exponential amplification of the corresponding bosonic modes. Outside this window, the modes evolve according to their coherent dynamics and are therefore not amplified. Indeed, out of Eq. (3.6), it is easy to verify that, on- and off-resonance, the evolution of the Bogoliubov operators reads

$$\beta_q^a(t) \simeq \begin{cases} e^{-i\Omega \frac{t}{2}} \left[\cosh(|\xi_q^a|t) \beta_q^a(0) + \text{sign}\{\xi_q^a\} \sinh(|\xi_q^a|t) \beta_{-q}^{a\dagger}(0) \right], & |\omega_q^a - \Omega/2| \ll |\xi_q^a|, \\ e^{-i\omega_q^a t} \beta_q^a(0), & |\omega_q^a - \Omega/2| \gg |\xi_q^a|. \end{cases} \quad (3.8)$$

3.2.3 Fermionic momentum distribution

The results above prove the possibility of amplifying bosonic collective modes (with different wavenumbers for charge and spin modes) while parametrically modulating the underlying 1D fermionic many-body Hamiltonian. However, the detection of this amplification is not necessarily easy from the experimental point of view. In the case of cold atoms in optical lattices this would require a (spin-resolved) measurement of the cloud density during the parametric modulation, without opening the trap. In view of this experimental challenge we now discuss the consequences of our analysis on the fermionic momentum distribution, which is the standard quantity measured in time-of-flight experiments [187]. Due to the different amplified momenta for charge and spin modes, we show that the fermionic momentum distribution shows clear signatures of spin-charge separation.

The momentum distribution function (per spin channel) for right-movers is defined as²

$$n_{kR}(t) = \int dx e^{ikx} \langle \psi_{R\sigma}^\dagger(x, t) \psi_{R\sigma}(0, t) \rangle, \quad (3.9)$$

where, within our perturbative treatment in $\eta \ll 1$, $\langle \dots \rangle$ represents a thermal average with respect to the *time-independent* part of the Hamiltonian (3.1), i.e., for $\eta = 0$. Expressing the fermionic field operators $\psi_{R\sigma}^\dagger(x, t)$ creating a right-mover with spin σ at position x and time t and its adjoint in terms of the bosonic operators $b_q^a(t)$ and $b_q^{a\dagger}(t)$ [191], we find after a lengthy but straightforward calculation [18] that the fermionic momentum distribution can be expressed as the convolution

$$n_{k,R}(t) = \int_{-\infty}^{+\infty} \frac{dq}{2\pi} n_{k-q,R}^0 \tilde{A}(q, t). \quad (3.10)$$

Here, $n_{k,R}^0$ is the fermionic momentum distribution in the absence of the parametric amplification. For $k > k_F$, it reads

$$n_{k,R}^0 = \frac{2^{1/2-\alpha}}{\sqrt{\pi}\Gamma(\alpha)} \int_0^\infty dQ' (Q + Q')^{\alpha-1/2} K_{\alpha-1/2}(Q + Q'), \quad (3.11)$$

with $\alpha = (\sinh^2 \varphi^c + \sinh^2 \varphi^s)/2$ and $Q = \lambda(k - k_F)$, $\Gamma(z)$ and $K_\nu(z)$ being the gamma and the modified Bessel functions, respectively. Here, λ is the screening length associated with the specific form of the interaction between the particles. In particular, $n_{k-k_F,R}^0 = 1 - n_{-k+k_F,R}^0$. The function $n_{k,R}^0$ is presented in Fig. 3.2 at time $t = 0$ for contact and finite-range interactions.

² As the problem is fully symmetric between right and left movers, we focus on the former without loss of generality.

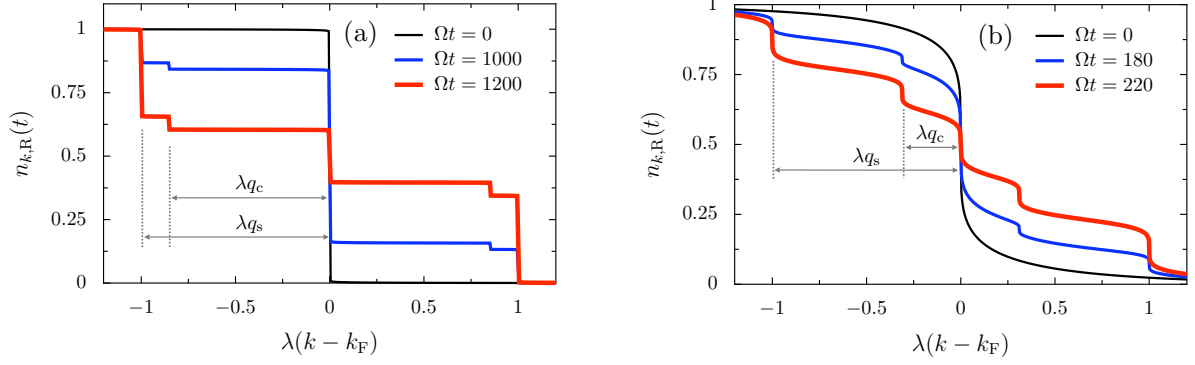


Figure 3.2: Fermionic momentum distribution for right movers $n_{k,R}(t)$ in the short-time regime (see Eq. 3.14) as a function of momentum k , scaled by the screening length λ . In the figure, $T = 0$, $\eta = 0.1$ and $\lambda q_s = 1$. (a) Case of contact s -wave scattering interaction, with $V_0^\perp/v_F = 0.5$ and $V_0^\parallel = V_{2k_F}^\parallel = 0$, such that $\lambda q_c = \lambda q_s v_s/v_c \simeq 0.85$. (b) Case of finite-range interactions, with $V_0^\perp/v_F = V_0^\parallel/v_F = 10$ and $V_{2k_F}^\parallel/v_F = 2$, such that $\lambda q_c = \lambda q_s v_s/v_c \simeq 0.31$.

The latter may be of relevance for the treatment of, e.g., trapped ions or cold polar molecules interacting through a power-law potential [204]. In Eq. (3.10), $\tilde{\mathcal{A}}(q, t)$ stands for the Fourier transform of the amplification factor

$$\mathcal{A}(x, t) = \exp \left(\sum_{a=c,s} h^a(t) [\cos(q_a x) - 1] \right), \quad (3.12)$$

where

$$h^a(t) = [1 + 2n_B(\Omega/2)] \kappa^a \cosh(2\varphi^a) [\cosh(\kappa^a \Omega t) - 1], \quad (3.13)$$

and $\kappa^a = \eta |\sinh(2\varphi^a)| v_F / 2v^a$. Here, $n_B(\omega) = (e^{\omega/T} - 1)^{-1}$ is the Bose distribution at temperature T . It is important to notice that the amplification factor equals 1 in the non-interacting limit [where $\sinh(\varphi^a) = 0$]. Once again, this highlights the importance of fermionic interactions as a necessary ingredient for the parametric amplification to occur.

Two qualitatively different regimes occur in the small- or large-time regimes, i.e., if $h^a(t) \ll 1$ or $h^a(t) \gg 1$ in Eq. (3.12). In the first case, the expansion of Eq. (3.12) leads to [18]

$$n_{k,R}(t) = n_{k,R}^0 + \sum_a h^a(t) \left(\frac{n_{k+q_a,R}^0 + n_{k-q_a,R}^0}{2} - n_{k,R}^0 \right). \quad (3.14)$$

Despite parametric amplification, the fermionic momentum distribution fulfills $n_{k-k_F,R} = 1 - n_{-k+k_F,R}$ as in the unperturbed case, guaranteeing particle-number conservation. For $k > k_F$ it shows two steps of size $h^{c/s}(t)/2$ involving fermionic states with momenta up to $q_{c/s}$ away from the Fermi level, as exemplified in Fig. 3.2.

These are direct signatures of the parametric amplification of the charge and spin density waves and their observation can thus be used to detect spin-charge separation in interacting 1D Fermi systems. By spanning the external modulation frequency Ω , the whole dispersion of

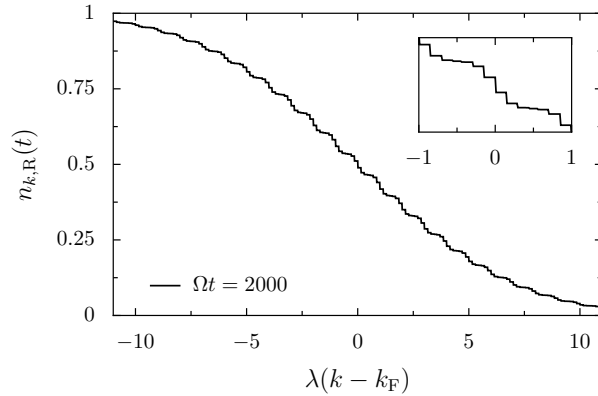


Figure 3.3: Momentum distribution for right movers $n_{k,R}(t)$ in the long-time regime [see Eq. (3.15)] as a function of momentum k . The parameters are the same as in Fig. 3.2(a). The inset presents the momentum distribution at a finer wavenumber scale close to the Fermi level.

the collective modes can be mapped. From the point of view of the measurement, our result is best visible in the “short-time regime” where the expansion above holds, leading to two well resolved steps of size up to about $1/2$. This fact is crucial in order to experimentally detect the amplification in the momentum distribution against other smoothening factors, like, e.g., trapping and finite temperatures.

Our analytical treatment allows formally the analysis of the “large-time regime” as well, where $h^a(t) \gg 1$. In this case we find [18]

$$n_{k,R}(t) = \sum_{m,n=-\infty}^{\infty} \frac{f_m^c(t) f_n^s(t)}{2\pi} n_{k-mq_c-nq_s,R}^0, \quad (3.15)$$

with $f_m^a(t) = (1/\sqrt{h^a(t)}) \exp(-m^2/2h^a(t))$. Thus, in the large-time limit the fermionic momentum distribution shows many small-size steps stemming from both the charge and the spin sectors (see Fig. 3.3). This will limit the experimental resolution of the structures in $n_{k,R}(t)$ in contrast to the short timescales. Moreover, at large times the exponential amplification of bosonic modes requires a treatment of their residual interaction beyond the Luttinger liquid model, associated to parabolic corrections to the linearized spectrum around the Fermi level [203, 205].

A final issue to be addressed in view of the experimental realization of our proposal is the role of finite temperatures, where our analysis above applies as well. The only differences are: (i) The presence of a non-vanishing Bose distribution in Eq. (3.13). This yields a thermal seed for the amplification on top of the pure quantum fluctuations at $T = 0$, and decreases the time needed for the formation of well-resolved steps in $n_{k,\tau}(t)$. (ii) The unperturbed momentum distribution $n_{k,R}^0$ in Eq. (3.10) has to be replaced with the finite temperature one, involving a thermal smearing of order T around the Fermi level (for $\alpha \ll 1$) on top of that purely induced by interactions. As thermal smearing involves wavenumbers up to order T/v_F around k_F , the shoulders in the final momentum distribution at short times are thus better visible if $v_F q_a \simeq \Omega/2 \gtrsim T$ ($a = c, s$), which can be guaranteed by choosing a sufficiently large Ω at a given temperature. In order for the Luttinger treatment to be reliable, the amplified q_a should

however be smaller than k_F , which restricts the best choice of Ω to the window $2T \lesssim \Omega \lesssim 4E_F$. The current experimental efforts to reach regimes of very low-temperatures $T \ll T_F$ with cold fermionic gases would then further improve the frequency range for the best visibility of the spin–charge separation.

3.2.4 Experimental realization

Our proposal could be experimentally realized with an equal mixture of quantum degenerate fermionic ^{40}K atoms confined into 1D cigars in the two hyperfine states $|F, m_F\rangle = |9/2, -9/2\rangle = |\downarrow\rangle$ and $|F, m_F\rangle = |9/2, -7/2\rangle = |\uparrow\rangle$. Here, F is the total angular momentum and m_F its projection along the quantization axis. It is important to realize that the atomic density corresponds to the charge channel, while the two hyperfine states above correspond to the (pseudo-)spin degree of freedom. Assuming the cigar of length $L = 0.1$ mm to be homogeneous and containing $N = 100$ atoms, we have $k_F = 3 \times 10^6 \text{ m}^{-1}$, which corresponds to a Fermi energy and temperature of order $E_F = 7$ kHz and $T_F = 60$ nK, respectively. For the interaction between neutral atoms, we assume contact s -wave scattering for which $V_0^{\parallel} = V_{2k_F}^{\parallel} = 0$ as required by the Pauli principle, and $V_0^{\perp}/v_F = \pi k_F a \omega_{\perp}/E_F$ [206]. Here, a is the 3D s -wave scattering length and ω_{\perp} the frequency of the transverse confining lasers creating the cigars. Notice that $E_F \ll \omega_{\perp}$ justifies the effective 1D treatment of the cigars. Assuming a scattering length of the order of $a = 10$ nm and $\omega_{\perp} = 40$ kHz, we obtain $V_0^{\perp}/v_F = 0.5$, which corresponds to the parameters in Fig. 3.2(a).

As our proposal is optimized in the regime $T \lesssim \Omega/2 \lesssim 2E_F$, and assuming $T/T_F \simeq 0.2$ [207], this corresponds to pumping frequencies in the range $3 \text{ kHz} \lesssim \Omega \lesssim 28 \text{ kHz}$. Measuring the fermionic momentum distribution by a time-of-flight experiment [187], one should thus obtain a clear signature of spin–charge separation for pumping times of the order of 100 ms (for $\Omega = 10$ kHz and $\eta = 0.1$), as exemplified in Fig. 3.2(a). Notice that longer pumping times would lead to a situation similar to the one depicted in Fig. 3.3 where spin–charge separation is much less clearcut and where temperature effects are likely to smear out most signatures of shoulders.

3.3 Parametric amplification of collective modes in a two-dimensional fermionic system

It is well known that a static magnetic field induces field-dependent collective modes termed magnetoplasmons [23, 169, 194]. These modes appear in particular in quasi-two-dimensional semiconductor quantum dots [208–210]. The magnetoplasmons, whose classical motion corresponds to an excitation of the electronic center of mass perpendicular to the magnetic field rotating clockwise and counterclockwise, have distinct frequencies that depend on the applied static magnetic field (see Fig. 3.4). In this section, we propose to trigger the parametric amplification of the magnetoplasmons by periodically modulating the magnetic field perpendicular to the nanostructure. Specifically, we focus on quasi-two-dimensional semiconductor quantum dots. We show that the parametric modulation of the magnetic field leads to an exponential growth of the occupation number of bosonic modes in the system. We further demonstrate how damping mechanisms and anharmonicities in the confinement of the quantum dot lead to the saturation of the parametric amplification.

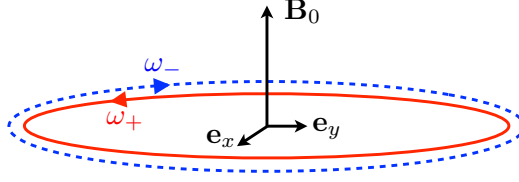


Figure 3.4: Sketch of the two independent center-of-mass motions associated to the surface magnetoplasmon modes perpendicular to the static magnetic field \mathbf{B}_0 .

3.3.1 Model

We consider N_e interacting electrons with effective mass m^* and charge $-e$ confined in a two-dimensional quantum dot. The quantum dot is subject to a spatially homogeneous perpendicular magnetic field $\mathbf{B}(t) = B(t)\mathbf{e}_z$ with

$$B(t) = B_0[1 + \eta \sin(\Omega t)] \quad (3.16)$$

which is periodically modulated at the frequency Ω . As in Sec. 3.2, we assume the strength of the periodic modulation η to be much smaller than one. The Hamiltonian of the system reads

$$H(t) = \sum_{i=1}^{N_e} \left[\frac{p_i^2}{2m^*} + U(r_i) + \frac{\omega(t)}{2} l_{z,i} + \frac{m^* \omega^2(t)}{8} r_i^2 \right] + \sum_{\substack{i,j=1 \\ (i \neq j)}}^{N_e} V_{e-e}(|\mathbf{r}_i - \mathbf{r}_j|), \quad (3.17)$$

with $\mathbf{r}_i = x_i\mathbf{e}_x + y_i\mathbf{e}_y$ the position of the i th electron and \mathbf{p}_i its momentum, $l_{z,i} = (\mathbf{r}_i \times \mathbf{p}_i)_z$ the z -component of the angular momentum, $\omega(t) = eB(t)/m^* = \omega_c[1 + \eta \sin(\Omega t)]$, and $\omega_c = eB_0/m^*$ the cyclotron frequency. The single-particle confinement $U(r)$ appearing in Eq. (3.17) is approximated by a parabolic potential with confining frequency ω_0 [169, 194]. Including also quartic corrections that will be relevant for the following analysis, we write it as

$$U(r) = \frac{m^* \omega_0^2}{2} r^2 + \frac{a_4}{4} r^4, \quad (3.18)$$

with $a_4 > 0$. Finally, V_{e-e} in Eq. (3.17) stands for the electron-electron interaction. As will be shown in the sequel of this section, the diamagnetic term $\propto \omega^2(t)$ in Eq. (3.17) is responsible for the parametric amplification of the magnetoplasmon collective modes.

Introducing the collective coordinate for the electronic center of mass $\mathbf{R} = X\mathbf{e}_x + Y\mathbf{e}_y = \sum_i \mathbf{r}_i/N$ and its conjugated momentum $\mathbf{P} = P_X\mathbf{e}_x + P_Y\mathbf{e}_y = \sum_i \mathbf{p}_i$, as well as the relative degrees of freedom $\mathbf{r}'_i = \mathbf{r}_i - \mathbf{R}$ and $\mathbf{p}'_i = \mathbf{p}_i - \mathbf{P}/N$, the Hamiltonian (3.17) separates into

$$H(t) = H_{\text{cm}}(t) + H_{\text{rel}}(t) + H_c, \quad (3.19)$$

with the center-of-mass Hamiltonian

$$H_{\text{cm}}(t) = \frac{P^2}{2M} + \frac{M}{2} \left(\omega_0^2 + \frac{\omega^2(t)}{4} \right) R^2 + \frac{\omega(t)}{2} L_Z + \frac{A_4}{4} R^4, \quad (3.20)$$

where $M = N_e m^*$, $A_4 = N_e a_4$, and $L_Z = XP_Y - YP_X$. The Hamiltonian $H_{\text{rel}}(t)$ for the relative coordinates has exactly the same form as in Eq. (3.17), provided one replaces $r_i \rightarrow r'_i$ and

$p_i \rightarrow p'_i$. Finally, the quartic part of the single-particle confinement (3.18) leads to the coupling between the center of mass and the relative coordinates in Eq. (3.19), with Hamiltonian

$$H_c = \frac{a_4}{4} \sum_i \left(|\mathbf{R} + \mathbf{r}'_i|^4 - R^4 - r_i'^4 \right). \quad (3.21)$$

If one assumes the single-particle confinement (3.18) to be purely harmonic ($a_4 = 0$), there is no coupling in Eq. (3.19) between the electronic center of mass and the relative coordinates, as requested by the generalized Kohn theorem [168, 169, 194]. The coupling (3.21) induces the damping of the center-of-mass excitations, and leads to a finite linewidth of the magnetoplasmon lines that can be observed in far infrared absorption spectroscopy experiments [169, 194].

The time-independent, quadratic part of the center-of-mass Hamiltonian (3.20) can be diagonalized by means of Fock-Darwin states in terms of two magnetoplasmon excitations [169]. Introducing the variable $\xi = (X + iY)/\sqrt{2}$ and the bosonic operators associated to the magnetoplasmons

$$b_+ = \frac{1}{\sqrt{2}} \left(\frac{\xi^*}{\ell} + \ell \frac{\partial}{\partial \xi} \right), \quad b_- = \frac{1}{\sqrt{2}} \left(\frac{\xi}{\ell} + \ell \frac{\partial}{\partial \xi^*} \right), \quad (3.22)$$

with the oscillator length $\ell = \sqrt{\hbar/M(\omega_0^2 + \omega_c^2/4)^{1/2}}$, we rewrite Eq. (3.20) as

$$\begin{aligned} H_{\text{cm}}(t) = & \sum_{\sigma=\pm} \hbar\omega_\sigma [1 + \sigma\delta f(t)] \left(b_\sigma^\dagger b_\sigma + \frac{1}{2} \right) + \alpha \frac{\hbar\omega_0}{4} (b_+^\dagger + b_-) (b_+ + b_-^\dagger)^2 \\ & + \frac{\hbar\omega_c}{2} \delta f(t) (b_+^\dagger b_-^\dagger + b_- b_+). \end{aligned} \quad (3.23)$$

In Eq. (3.23),

$$\delta f(t) = \eta \frac{\omega_c/2}{\sqrt{\omega_0^2 + \omega_c^2/4}} \sin(\Omega t), \quad (3.24)$$

and we introduced the dimensionless parameter $\alpha = A_4 \ell^4 / \hbar\omega_0 \ll 1$. The frequencies of the two magnetoplasmon collective modes read [169]

$$\omega_\pm = \sqrt{\omega_0^2 + \frac{\omega_c^2}{4}} \pm \frac{\omega_c}{2} \quad (3.25)$$

and are presented in Fig. 3.5 as a function of the cyclotron frequency ω_c . Without parametric modulation ($\eta = 0$), the center-of-mass motion associated with the magnetoplasmon with frequency ω_+ (ω_-) rotates counterclockwise (clockwise) in the plane perpendicular to the magnetic field (see Fig. 3.4). Notice that one has $\omega_+ > \omega_-$ due to the fact that the Lorentz force $-N_e e \dot{\mathbf{R}} \times \mathbf{B}_0$ increases (decreases) the effective harmonic confinement seen by the collective mode with frequency ω_+ (ω_-).

The last symmetry breaking term $\propto b_+^\dagger b_-^\dagger + b_+ b_-$ in the Hamiltonian (3.23) is triggered by the parametric modulation of the magnetic field [see Eq. (3.24)]. This term is responsible for the parametric amplification of the two magnetoplasmon collective modes, provided that the pumping frequency Ω is close to the resonance condition $\Omega = \omega_+ + \omega_-$ (see dotted line in Fig. 3.5). The quartic corrections proportional to the parameter α in the Hamiltonian (3.23) represent a residual interaction between the two bosonic modes, and lead to the saturation of the parametric amplification.

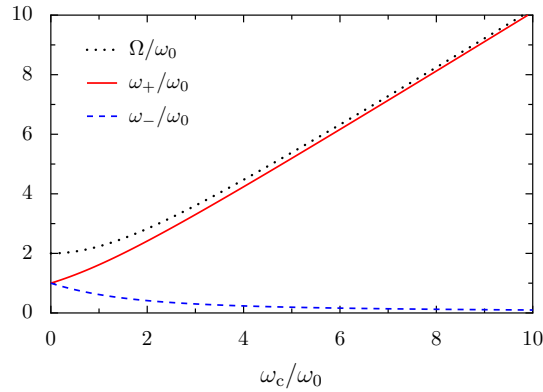


Figure 3.5: Frequencies ω_+ and ω_- [cf. Eq. (3.25)] of the two magnetoplasmon modes (rescaled by the confinement frequency ω_0) as a function of the cyclotron frequency ω_c . The pumping frequency exactly at resonance, $\Omega = \omega_+ + \omega_-$, is also shown as a dotted line.

In the absence of quartic corrections ($\alpha = 0$), the Hamiltonian (3.23) is similar to the one encountered in the quantum theory of parametric amplifiers in quantum optics [211–215]. In this context, a pump laser interacts with a nonlinear crystal. Due to the second-order susceptibility of the nonlinear media, a photon of the pump laser at frequency Ω splits into two photons at frequencies ω_+ and ω_- , a phenomenon called parametric down conversion. In a parametric amplifier, the two signals at frequencies ω_+ and ω_- are amplified by pumping the crystal at $\Omega = \omega_+ + \omega_-$.

3.3.2 Parametric resonance of the magnetoplasmons

We start our study of the possibility of parametrically amplifying the magnetoplasmon collective modes by neglecting the quartic part of the center-of-mass Hamiltonian, setting $\alpha = 0$ in Eq. (3.23). Furthermore, we neglect all other sources of dissipation on top of the one induced by the quartic confinement. Solving the corresponding Heisenberg equations of motion for the bosonic operators appearing in the center-of-mass Hamiltonian (3.23) in the limit of weak pumping ($\eta \ll 1$) and in the rotating wave approximation ($\Omega \simeq \omega_+ + \omega_-$) yields [22]

$$b_{\pm}(t) = \frac{e^{-i\omega_{\pm}t}}{\Omega_- - \Omega_+} \left[(\Omega_- e^{i\Omega_+t} - \Omega_+ e^{i\Omega_-t}) b_{\pm}(0) + i\frac{\epsilon}{2} (e^{i\Omega_+t} - e^{i\Omega_-t}) b_{\mp}^{\dagger}(0) \right], \quad (3.26)$$

with

$$\Omega_{\pm} = \frac{\omega_+ + \omega_- - \Omega}{2} \pm \frac{1}{2} \sqrt{(\Omega - \omega_+ - \omega_-)^2 - \epsilon^2}, \quad (3.27)$$

where we introduced the “driving” frequency

$$\epsilon = \eta \frac{(\omega_c/2)^2}{\sqrt{\omega_0^2 + \omega_c^2/4}}. \quad (3.28)$$

We thus see that tuning the pumping frequency Ω in the interval $|\Omega - \omega_+ - \omega_-| < \epsilon$, the frequencies Ω_{\pm} acquire an imaginary part, leading to the parametric amplification of the bosonic

magnetoplasmon collective modes. Indeed, close to resonance, i.e., for $|\Omega - \omega_+ - \omega_-| \ll \epsilon$, Eq. (3.26) simplifies to

$$b_{\pm}(t) = e^{-i\omega_{\pm}t} \left[\cosh\left(\frac{\epsilon t}{2}\right) b_{\pm}(0) + \sinh\left(\frac{\epsilon t}{2}\right) b_{\mp}^{\dagger}(0) \right], \quad (3.29)$$

showing that the two bosonic modes are exponentially amplified at a rate given by the frequency ϵ of Eq. (3.28). On the contrary, off resonance ($|\Omega - \omega_+ - \omega_-| \gg \epsilon$), the bosonic operators evolve in time according to their unitary evolution, $b_{\pm}(t) = e^{-i\omega_{\pm}t} b_{\pm}(0)$.

We assume that the center-of-mass subsystem is, prior to the parametric modulation that starts at $t = 0$, in thermal equilibrium at the temperature T and thus described by the density matrix $\rho_0 = e^{-H_{\text{cm}}(0)/k_{\text{B}}T} / \mathcal{Z}$ with $\mathcal{Z} = \text{tr}\{e^{-H_{\text{cm}}(0)/k_{\text{B}}T}\}$ the canonical partition function. Due to the fact that the magnetoplasmons are purely harmonic excitations of the electronic center of mass, $\langle R \rangle(t) = 0$, the fluctuations of the center-of-mass coordinate $\langle \delta R^2 \rangle(t) = \langle R^2 \rangle(t) - \langle R \rangle^2(t)$ reduce to

$$\langle \delta R^2 \rangle(t) = \ell^2 [N_+(t) + N_-(t) + 1 + \varphi(t) + \varphi^*(t)]. \quad (3.30)$$

Here, we introduced the average number of bosons in each mode $N_{\pm}(t) = \langle b_{\pm}^{\dagger} b_{\pm} \rangle(t)$, as well as the ‘‘anomalous’’ average $\varphi(t) = \langle b_+ b_- \rangle(t)$ where $\langle \mathcal{O} \rangle(t) = \text{tr}\{\rho_0 \mathcal{O}(t)\}$. Using Eq. (3.29), we obtain by averaging over a timescale long compared to Ω^{-1} , but short compared to ϵ^{-1} ($\epsilon \ll \Omega$)

$$\overline{\langle \delta R^2 \rangle}(t) = \ell^2 [1 + n_{\text{B}}(\omega_+) + n_{\text{B}}(\omega_-)] \cosh(\epsilon t) \quad (3.31)$$

when the pumping frequency is close to resonance. The fluctuations of the center-of-mass are thus exponentially amplified due to the parametric modulation of the magnetic field. Notice that even at zero temperature, where initially the two bosonic modes are unoccupied [$n_{\text{B}}(\omega_{\pm}) = 0$ in Eq. (3.31)], parametric amplification takes place, triggered by the quantum fluctuations of the center-of-mass coordinate.

3.3.3 Effects of damping and anharmonicities on the parametric resonance of the magnetoplasmons

In this section, we analyze the role played by dissipation and non-linearities on the parametric amplification of the magnetoplasmons. As we will show, these two effects are indeed limiting the exponential amplification of the bosonic modes presented in Sec. 3.3.2. It is therefore relevant to study them as they will inevitably affect experiments.

In what follows, we adopt a different strategy than the one used in Sec. 3.3.2, and focus on the time evolution of averaged quantities as we are primarily interested in the fluctuations of the center-of-mass coordinate, Eq. (3.30). To this end, we use the time evolution of the reduced density matrix ρ associated to the center-of-mass degrees of freedom,

$$\dot{\rho} = -\frac{i}{\hbar} [H_{\text{cm}}, \rho] + \sum_{\sigma=\pm} \frac{\gamma_{\sigma}}{2} \left(2b_{\sigma} \rho b_{\sigma}^{\dagger} - b_{\sigma}^{\dagger} b_{\sigma} \rho - \rho b_{\sigma}^{\dagger} b_{\sigma} \right). \quad (3.32)$$

The first term on the right-hand side of Eq. (3.32) accounts for the unitary dynamics of the center-of-mass density matrix that evolves according to the Hamiltonian (3.23). The second term accounts for dissipative processes coming from the anharmonicities [and hence from the coupling Hamiltonian (3.21)], as well as stemming from other sources of dissipation, such as radiative damping, interaction with phonons, Joule heating due to the eddy currents

3.3 Parametric amplification of collective modes in a two-dimensional fermionic system

generated by the electric field associated with the time-dependent magnetic field (3.16), etc. In Eq. (3.32), we take dissipation phenomenologically into account by assuming the Lindblad form for the reduced density matrix [216]. We denote γ_+ and γ_- the damping rates for the two magnetoplasmon modes. Notice that, in general, $\gamma_+ \neq \gamma_-$ due to the difference in energy of the two modes, as we recently demonstrated in the context of the Landau damping of the magnetoplasmon excitations in metallic nanoparticles [23].

From the master equation (3.32), the time evolution of the quantum average of an operator \mathcal{O} is determined using the identity $\langle \mathcal{O} \rangle(t) = \text{tr}\{\dot{\rho}(t)\mathcal{O}\}$. Introducing the notation $N = N_+ + N_-$, $\Delta N = N_+ - N_-$, $\gamma = (\gamma_+ + \gamma_-)/2$, and $\Delta\gamma = (\gamma_+ - \gamma_-)/2$, we find from Eqs. (3.23) and (3.32)

$$\begin{aligned} \dot{N} = & i\omega_c \delta f(t) (\varphi - \varphi^*) - \gamma N - \Delta\gamma \Delta N - i\alpha\omega_0 \left[2(\varphi^* - \varphi) + \langle b_+^\dagger b_+^\dagger b_-^\dagger b_-^\dagger \rangle + \langle b_+^\dagger b_+^\dagger b_-^\dagger b_+ \rangle \right. \\ & \left. + \langle b_+^\dagger b_+^\dagger b_-^\dagger b_- \rangle - \langle b_+^\dagger b_+ b_+ b_- \rangle - \langle b_-^\dagger b_+ b_- b_- \rangle - \langle b_+ b_+ b_- b_- \rangle \right], \end{aligned} \quad (3.33a)$$

$$\Delta \dot{N} = -\gamma \Delta N - \Delta\gamma N, \quad (3.33b)$$

$$\begin{aligned} \dot{\varphi} = & -i[\omega_+ + \omega_- + \omega_c \delta f(t)] \varphi - i\frac{\omega_c}{2} \delta f(t) (N + 1) - \gamma \varphi \\ & - i\frac{\alpha\omega_0}{2} \left(2 + 6\varphi + 2\varphi^* + 4N + \langle b_+^\dagger b_+^\dagger b_-^\dagger b_+ \rangle + \langle b_+^\dagger b_+^\dagger b_-^\dagger b_- \rangle + 4\langle b_+^\dagger b_-^\dagger b_+ b_- \rangle + \langle b_+^\dagger b_+^\dagger b_+ b_+ \rangle \right. \\ & \left. + \langle b_-^\dagger b_-^\dagger b_- b_- \rangle + 3\langle b_+^\dagger b_+ b_+ b_- \rangle + 3\langle b_-^\dagger b_+ b_- b_- \rangle + 2\langle b_+ b_+ b_- b_- \rangle \right). \end{aligned} \quad (3.33c)$$

The four-operator correlators appearing in Eq. (3.33) must be evaluated for $\alpha = 0$ since these terms are multiplied by α and we work in first order in this small anharmonicity parameter. Since for $\alpha = 0$, the Hamiltonian of Eq. (3.23) is quadratic in the bosonic operators, one can apply Wick's theorem. Introducing $\varphi(t) = \exp\left(-i\int_0^t ds [\omega_+ + \omega_- + \omega_c \delta f(s)]\right) \tilde{\varphi}(t)$, to first order in the parametric modulation amplitude $\eta \ll 1$ and within the rotating wave approximation close to resonance ($\Omega \simeq \omega_+ + \omega_-$), we then find [22]

$$\dot{N} = \epsilon \left[e^{i(\Omega - \omega_+ - \omega_-)t} \tilde{\varphi} + \text{c.c.} \right] - \gamma N - \Delta\gamma \Delta N - 2\alpha\omega_0 \frac{\epsilon}{\Omega} \left[e^{i(\Omega - \omega_+ - \omega_-)t} \tilde{\varphi} + \text{c.c.} \right] (N + 1), \quad (3.34a)$$

$$\Delta \dot{N} = -\gamma \Delta N - \Delta\gamma N, \quad (3.34b)$$

$$\begin{aligned} \dot{\tilde{\varphi}} = & \frac{\epsilon}{2} e^{-i(\Omega - \omega_+ - \omega_-)t} (N + 1) - \gamma \tilde{\varphi} - 3i\alpha\omega_0 \tilde{\varphi} (N + 1) \\ & - \alpha\omega_0 \frac{\epsilon}{\Omega} \left\{ e^{-i(\Omega - \omega_+ - \omega_-)t} \left[(N + 1)^2 + 2\tilde{\varphi}\tilde{\varphi}^* \right] - 2e^{i(\Omega - \omega_+ - \omega_-)t} \tilde{\varphi}^2 \right\}. \end{aligned} \quad (3.34c)$$

It is instructive to first analyze the effect of damping alone on the parametric resonance of the magnetoplasmon excitations. To this end, we set the anharmonicity parameter α to zero in Eq. (3.34). Using the initial conditions $N(0) = n_B(\omega_+) + n_B(\omega_-)$, $\Delta N(0) = n_B(\omega_+) - n_B(\omega_-)$, and $\tilde{\varphi}(0) = 0$, an analytical solution of Eq. (3.34) at resonance ($\Omega = \omega_+ + \omega_-$) can be obtained [22]. We display the result in Fig. 3.6. As can be seen from the figure, when $\epsilon > \sqrt{\gamma^2 - \Delta\gamma^2}$, the solutions to Eq. (3.34) are exponentially amplified (solid red lines). On the contrary, for $\epsilon < \sqrt{\gamma^2 - \Delta\gamma^2}$, the system reaches the stationary solution

$$N^{\text{st}} = \frac{\epsilon^2}{\gamma^2 - \Delta\gamma^2 - \epsilon^2}. \quad (3.35)$$

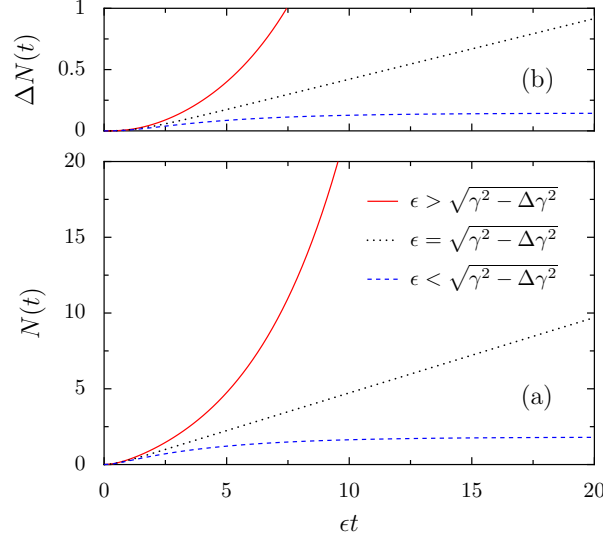


Figure 3.6: (a) Total number $N(t)$ and (b) difference $\Delta N(t)$ of bosonic excitations between the modes $+$ and $-$ as a function of time from the analytical solution of Eq. (3.34) for $\alpha = 0$ at resonance ($\Omega = \omega_+ + \omega_-$). In the figure, $T = 0$, $\Delta\gamma = -\epsilon/10$, and $\gamma = 3\epsilon/4$, $\sqrt{1.01}\epsilon$, and $5\epsilon/4$ for the solid red, dotted black, and dashed blue lines, respectively.

For the special case $\epsilon = \sqrt{\gamma^2 - \Delta\gamma^2}$, the analytical solution of Eq. (3.34) yields a linear behavior as a function of t (see dotted black lines in Fig. 3.6).

We now turn to the full solution of Eq. (3.34), including anharmonic terms, i.e., $\alpha \neq 0$. To this end, we concentrate on the case where the pumping frequency is at resonance, i.e., $\Omega = \omega_+ + \omega_-$. A numerical solution of Eq. (3.34) is presented in Fig. 3.7 for the case where $\epsilon > \sqrt{\gamma^2 - \Delta\gamma^2}$, i.e., when parametric amplification takes place in the absence of the anharmonic term ($\alpha = 0$), see Fig. 3.6. For short times, both the total number of bosonic modes $N(t)$ [Fig. 3.7(a)] and the difference between the occupation of the $+$ and $-$ modes, $\Delta N(t)$ [Fig. 3.7(b)] get exponentially amplified. This behavior is followed by a series of oscillations, to finally reach a stationary occupation due to the residual (anharmonic) interaction.

To better understand the numerical results of Fig. 3.7(a,b), we now search for the stationary solution of Eq. (3.34). Since we work to first order in the small parameters $\epsilon/\Omega \ll 1$ and $\alpha \ll 1$, we neglect the terms $\propto \alpha\epsilon/\Omega$ in Eq. (3.34), yielding

$$\left(1 - \frac{\Delta\gamma^2}{\gamma^2}\right) (3\alpha\omega_0)^2 N^{\text{st}} (N^{\text{st}} + 1)^2 - (\epsilon^2 + \Delta\gamma^2 - \gamma^2) N^{\text{st}} - \epsilon^2 = 0. \quad (3.36)$$

The solution to Eq. (3.36) is shown in Fig. 3.7(c) as a red solid line as a function of the driving frequency ϵ . For $\epsilon > \sqrt{\gamma^2 - \Delta\gamma^2}$ and $\alpha = 0$, we know from our previous study that $N(t)$ diverges exponentially, such that we can safely assume for that case $N^{\text{st}} \gg 1$ in Eq. (3.36). If on top of that, $(\epsilon^2 + \Delta\gamma^2 - \gamma^2)N^{\text{st}} \gg \epsilon^2$, we obtain

$$N^{\text{st}} \simeq \frac{\sqrt{\epsilon^2 + \Delta\gamma^2 - \gamma^2}}{3\alpha\omega_0 \sqrt{1 - \Delta\gamma^2/\gamma^2}}, \quad (3.37)$$

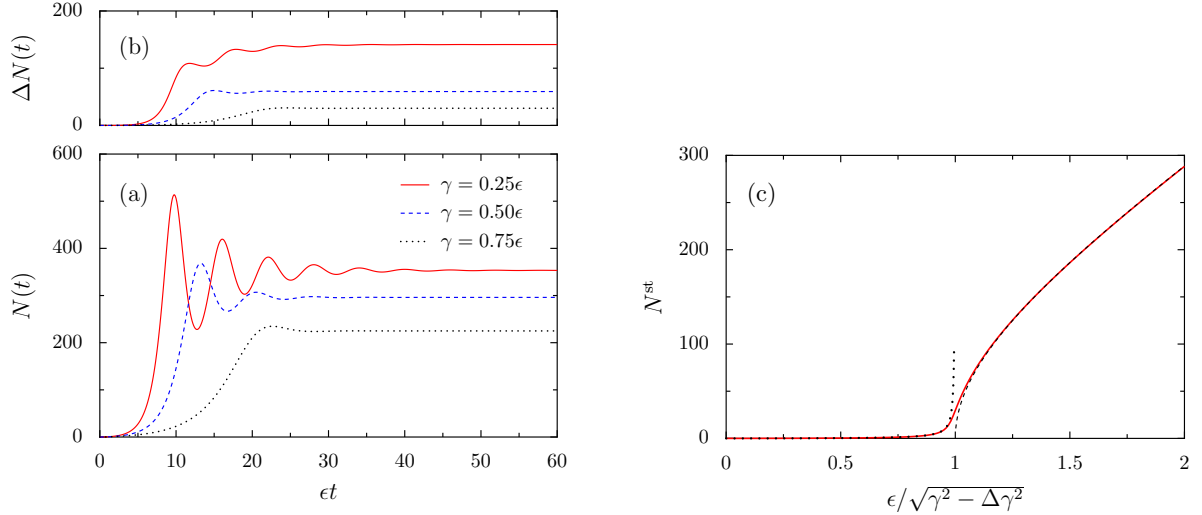


Figure 3.7: (a) Total number $N(t)$ and (b) difference $\Delta N(t)$ of bosonic excitations as a function of time from a numerical solution of Eq. (3.34) at resonance ($\Omega = \omega_+ + \omega_-$) for various values of the damping constant γ . Parameters: $T = 0$, $\Delta\gamma = -\epsilon/10$, $\omega_0 = 10^3\epsilon$, $\Omega = \sqrt{5}\omega_0$ (corresponding to $\omega_c = \omega_0$), and $\alpha = 10^{-6}$. (c) Stationary number of bosonic modes from Eq. (3.36) as a function of the driving frequency ϵ (solid red line). The asymptotic behaviors for $\epsilon < \sqrt{\gamma^2 - \Delta\gamma^2}$ [Eq. (3.35)] and $\epsilon > \sqrt{\gamma^2 - \Delta\gamma^2}$ [Eq. (3.37)] are shown as a dotted and a dashed line, respectively. Parameters: $\alpha = 10^{-6}$ and $\omega_0/\gamma = 2 \times 10^3$.

showing that the smaller α , the more efficient is the parametric amplification. The asymptotic behavior of Eq. (3.37) is shown as a dashed line in Fig. 3.7(c) and compares well with the full solution of Eq. (3.36) (solid red line). For the case $\epsilon < \sqrt{\gamma^2 - \Delta\gamma^2}$, we find that parametric amplification does not take place, and that the stationary number of bosonic modes is, to first order in α , given by Eq. (3.35), as shown in Fig. 3.7 by a dotted line.

3.3.4 Experimental consequences

Before presenting the various possible experimental consequences of our proposal, we start this section by discussing how one can trigger the parametric resonance of the magnetoplasmon collective modes in realistic quasi-two-dimensional semiconductor quantum dots. For a GaAs quantum dot with a confinement frequency $\omega_0 = 1.7$ THz ($\hbar\omega_0 = 1.1$ meV) in a static magnetic field of $B_0 = 2$ T, the eigenfrequencies (3.25) are given by $\omega_+ = 5.7$ THz and $\omega_- = 0.5$ THz [23]. The resonance condition $\Omega = \omega_+ + \omega_-$ for parametric amplification to occur [see Eq. (3.27)] thus requires in this case that the magnetic field is periodically modulated at the frequency $\Omega/2\pi = 0.99$ THz. The ongoing efforts towards the production of THz sources should allow one to attain such pumping frequencies in a near future [217–219]. As we have shown in Sec. 3.3.3, parametric amplification only occurs if the driving frequency ϵ of Eq. (3.28) is larger than the linewidth γ of the magnetoplasmons (assumed here to be the same for both collective modes). With a pumping strength $\eta = 0.1$, we obtain $\epsilon = 0.22$ THz. Assuming $\gamma \simeq \omega_0/10$ which is the typical value encountered in experiments [208], parametric amplification should

occur in this case at a rate given by $\epsilon - \gamma = 50$ GHz.

In what follows, we propose several ways of detecting the parametric amplification of the magnetoplasmons: First, these modes decay, among various processes, by radiative damping, emitting photons at the frequencies ω_+ and ω_- . Triggering the parametric resonance of the modes with the only help of a modulated magnetic field should thus result in the spontaneous emission of photons at these frequencies, *without* using an external light source, as usually employed in far infrared spectroscopy experiments.

Second, as we have shown in Sec. 3.3.2, the average fluctuations of the electronic center-of-mass coordinate are directly related to the total number of bosonic excitations N in the system, $\overline{\delta R^2} \sim N$. As the latter is exponentially amplified up to its stationary value (3.37) due to the anharmonicity, this should result in an expansion of the whole electronic cloud forming the quantum dot which can be measured by scanning tunneling microscopy [220].

Another measurable quantity [221, 222] related to the fluctuations of the center-of-mass coordinate is the magnetization of the quantum dot. Indeed, the magnetization operator for the electronic system described by the Hamiltonian (3.17) reads [22] $\mathbf{M} = \mathbf{M}_{\text{cm}} + \mathbf{M}_{\text{rel}}$, with

$$\mathbf{M}_{\text{cm}} = -\frac{e}{2m^*} \left(L_Z + \frac{N_e e B(t)}{2} R^2 \right) \mathbf{e}_z \quad (3.38)$$

the contribution from the center-of-mass dynamics, and

$$\mathbf{M}_{\text{rel}} = -\frac{e}{2m^*} \sum_i \left(l'_{z,i} + \frac{e B(t)}{2} r_i'^2 \right) \mathbf{e}_z \quad (3.39)$$

the one from the relative coordinates. Since the latter is induced by a bath of fermionic quasi-particles, the modulation of the magnetic field does not lead to their parametric amplification.³

In contrast, the magnetization (3.38) resulting from the center-of-mass dynamics and which can be conveniently rewritten in terms of the bosonic operators (3.22) can be parametrically amplified. Indeed, taking the expectation value of Eq. (3.38) and averaging over fastly oscillating terms, we find, to first order in the parametric modulation strength η ,

$$\overline{\langle \mathbf{M}_{\text{cm}} \rangle}(t) = -\mu_{\text{B}}^* \mathbf{e}_z \left\{ \Delta N(t) + \frac{\omega_c/2}{\sqrt{\omega_0^2 + \omega_c^2/4}} [N(t) + 1] \right\}, \quad (3.40)$$

with $\mu_{\text{B}}^* = e\hbar/2m^*$ the effective Bohr magneton ($\mu_{\text{B}}^* = 0.86$ meV/T for GaAs). As both the total number of bosonic excitations $N(t)$ and the difference $\Delta N(t)$ are exponentially amplified due to the parametric modulation to finally reach stationary values [see Fig. 3.7], the resulting magnetization of the dot should dramatically increase when the parametric amplification of the magnetoplasmons takes place as compared to its equilibrium value.

3.4 Conclusion

In this chapter, we have asked the question whether it is possible to parametrically amplify collective bosonic modes in many-body fermionic systems. The answer to this question is positive, as we have illustrated with two examples.

³ In fact, the only result of the modulation is a small periodic variation of the relative magnetization that averages to zero due to the fast modulation. As a consequence, the average magnetization resulting from the relative coordinates is constant in time and equals its value without parametric modulation, $\overline{\langle \mathbf{M}_{\text{rel}} \rangle}$.

In Sec. 3.2 we have shown the possibility of parametrically amplifying collective modes in a modulated 1D fermionic many-body system. The amplification is crucially affected by fermionic interactions which were exactly treated within the Luttinger liquid picture. Our analysis shows that the amplification of charge and spin density waves of the Luttinger liquid results in clear steps in the fermionic momentum distribution. The wavenumber extension of the steps directly reveals the different momenta of the excited charge and spin modes and thus offers a tool for the detection of spin–charge separation. In parallel, we have shown that the best resolution of the steps is achieved by modulations of relatively short times and that they survive thermal effects for large enough modulation frequencies.

Our proposal of detection of spin–charge separation is particularly suitable for systems of cold fermionic atoms in 1D optical lattices with modulated intensity. The fermionic momentum distribution is indeed the standard quantity measured in time-of-flight experiments. We stress that for our proposal no additional experimental setup is required on top of the already present tunable lasers creating the optical lattice.

In Sec. 3.3, we have studied the possibility of parametrically amplifying bosonic collective modes in finite-size fermionic systems beyond 1D. Specifically, we have shown that the magnetoplasmons in quasi-2D semiconductor quantum dots can be parametrically amplified by modulating the magnetic field perpendicular to the nanostructure. Moreover, we have quantified at which value the parametric amplification saturates due to damping mechanisms and anharmonicities of the confinement of the quantum dot. We have further discussed the implementation of our proposal in realistic experimental samples and suggested measurements that should present clear signatures of the parametric amplification of the magnetoplasmons.

Our predictions could in principle also apply to the magnetoplasmon modes in metallic nanoparticles. However, as the damping of these modes is much stronger than in quantum dots [23], it may be much more difficult to trigger the parametric amplification in metallic nanoparticles.

Related publications

- C. D. Graf, G. Weick, E. Mariani
Parametric resonance and spin-charge separation in 1D fermionic systems
[EPL **89**, 40005 \(2010\)](#)
- G. Weick, D. Weinmann
Lifetime of the surface magnetoplasmons in metallic nanoparticles
[Phys. Rev. B **83**, 125405 \(2011\)](#)
- G. Weick, E. Mariani
Parametric amplification of magnetoplasmons in semiconductor quantum dots
[Phys. Rev. B **84**, 125441 \(2011\)](#)

Chapter 4

Research project: Novel quantum metamaterials based on metallic nanoparticles

4.1 Scientific context at IPCMS

Due to their small sizes, metallic nanoparticles show spectacular quantum effects that are absent in the bulk. Most of these effects stem from the confinement of the electronic eigenstates, the latter being due to the relatively large surface-to-volume ratio in particles with nanometric sizes [223, 224]. The most striking evidence of the quantization of the electronic states in metallic nanoparticles is the electronic shell structure, first observed by Knight and coworkers in 1984 [225]. The resulting size effects show up in many of the physical properties of metallic clusters, e.g., in their abundance spectra, static dipole polarizabilities, ionization potentials, and optical properties [226, 227].

Once metallic nanoparticles are put together and interact among each other and/or with the surrounding environment, they form metamaterials with fascinating and intriguing properties that are different from those of individual, isolated nanoparticles. Such nanoparticle-based metamaterials are the subject of active experimental investigations at IPCMS and elsewhere, and our project aims at bringing theoretical support to these experiments.

Nanoparticle-based metamaterials present a wide range of peculiar properties that can be very different from those of the elementary building blocks. Our project focuses on two of these properties: the magnetic and optical ones. An aspect that attracted considerable attention over the last decade is the unusual magnetic behavior of ensembles of gold nanoparticles. Indeed, while gold is diamagnetic in the bulk, several experiments have shown that ensembles of gold nanoparticles capped with organic ligands can present a ferromagnetic-like behavior of the magnetization [35–38] (see Fig. 4.1). Other samples show a paramagnetic-like behavior, and some others a diamagnetism which is typically stronger than in the bulk.¹ These different magnetic properties that vary from sample to sample, as well as the underlying mechanisms giving rise to these features are a source of intense debate in the community. An interpretation of the unusual magnetic properties of ensembles of gold nanoparticles that has been recently proposed by the team of Jean-Louis Gallani in the Department of Organic Materials at IPCMS is that it could be of orbital character, independent of the molecules surrounding the nanoparticles. Our research project aims at investigating the orbital magnetism of nanoparticle assemblies and determine whether such intriguing magnetic behaviors observed experimentally can be accounted for by this mechanism.

Other fascinating aspects of nanoparticle-based metamaterials reside in their optical properties. While the field of plasmonics mostly focuses on single or few structures, the creation of ordered arrays of nanoparticles constitutes a bridge to the realm of metamaterials [116]. This

¹ For a recent review of the magnetic properties of gold nanoparticles, see Ref. [39].

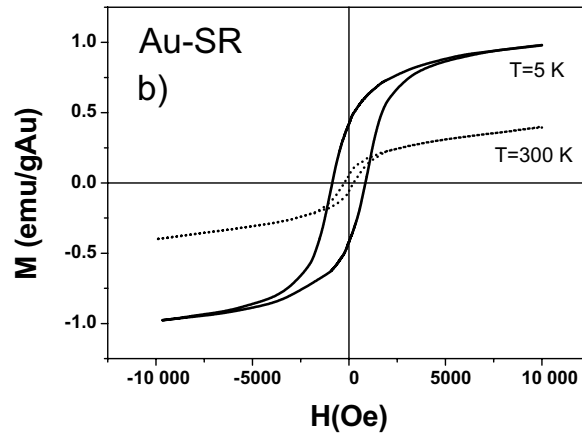


Figure 4.1: Magnetization curves of gold thiol-capped nanoparticles (Au-SR) at 5 K and 300 K (solid and dotted lines, respectively). Reproduced from Ref. [35].

interesting feature results in plasmonic metamaterials that exhibit unique properties beyond traditional optics. In Chapter 2, we have theoretically demonstrated that collective plasmons in honeycomb plasmonic lattices behave as Dirac-like massless bosonic excitations [26,28]. These excitations should present some of the properties of electrons in graphene, such as a non-trivial Berry phase and the absence of backscattering off impurities. The goal of our project is to investigate the unusual properties of collective plasmons in honeycomb plasmonic lattices and then to build on such an understanding in order to propose metamaterials with novel features. Since this part of our project has been already presented quite in detail in Chapter 2, we will not come back to it in what follows. We will instead insist on the first part of the project that concerns the unusual magnetic behavior of gold nanoparticles.

This research project is funded since October 2014 by a four-year young researcher grant from the Agence Nationale de la Recherche (ANR-14-CE26-0005 Q-MetaMat, “Novel Quantum Metamaterials Based on Metallic Nanoparticles”).² The project is also supported by the CNRS international exchange PICS program (Contract No. 6384 APAG, “A Plasmonic Analogue of Graphene”) in the context of our fruitful collaboration with Eros Mariani at the University of Exeter in United Kingdom.

For confidentiality reasons, the remaining of this chapter is not included in the online version of the manuscript.

² http://www.ipcms.unistra.fr/?page_id=21342

Appendix A

Résumé détaillé en français

Introduction générale

Le présent manuscrit d'habilitation à diriger des recherches résume les activités de recherche que j'ai menées dans le domaine de la physique théorique de la matière condensée depuis la fin de ma thèse de doctorat, que j'ai soutenue en septembre 2006. Au cours de ma thèse, qui était sous le régime de cotutelle et co-encadrée par Gert Ingold (Université d'Augsbourg en Allemagne) et Rodolfo Jalabert (Université Louis Pasteur de Strasbourg), j'ai étudié la dynamique des électrons dans les nanoparticules métalliques uniques. Motivé par des expériences menées dans l'équipe de Jean-Yves Bigot [1–3] à l'Institut de Physique et Chimie des Matériaux de Strasbourg (IPCMS), j'étais en particulier intéressé par l'élaboration d'un cadre théorique cohérent [4–9] pour comprendre les mécanismes conduisant à la durée de vie finie des excitations électroniques collectives dans des amas métalliques de taille nanométrique.

Dans le but d'explorer de nouveaux sujets de recherche, j'ai déménagé en octobre 2006 à Berlin afin d'effectuer un stage post-doctoral dans le groupe de transport quantique de Felix von Oppen à la Freie Universität de Berlin (FU). Je suis de la sorte entré dans le domaine des nanosystèmes électromécaniques (NEMS : NanoElectroMechanical Systems), dans lesquels un petit objet mécanique mobile (tels que, par exemple, une molécule unique, un nanorésonateur ou un nanotube de carbone suspendu) est couplé au transport électronique [10–12]. En particulier, j'ai participé à un projet visant à comprendre comment le courant émanant d'une pointe de microscope à effet tunnel vers une molécule présentant différentes conformations peut induire la commutation entre ses différents isomères [13]. Ce travail, motivé par des expériences [14] menées dans le groupe de Nacho Pascual à la FU (maintenant à San Sebastian), a été réalisé en collaboration avec un étudiant en thèse (Florian Elste), Carsten Timm (Technische Universität de Dresde) et Felix von Oppen. Avec Fabio Pistolesi (Bordeaux), Eros Mariani (à l'époque également en postdoc à la FU, aujourd'hui « Lecturer » à l'Université d'Exeter) et Felix von Oppen, nous avons démarré lors de cette période un travail sur les instabilités mécaniques dans les NEMS [15], en prenant la bien connue instabilité d'Euler comme exemple [16, 17]. Avec Eros Mariani et un étudiant de Master (Christian Graf), nous avons également commencé une nouvelle ligne de recherche au cours de ces années à Berlin, à savoir l'étude des résonances paramétriques dans des systèmes fermioniques à plusieurs corps [18].

En décembre 2009, je suis revenu à Strasbourg afin de prendre un poste de trois ans de chercheur CR2 en CDD à l'IPCMS, dans l'Équipe de Physique Mésoscopique dirigée par Rodolfo Jalabert et Dietmar Weinmann. C'est alors, en collaboration avec Fabio Pistolesi et Felix von Oppen, mais aussi avec deux étudiants en Master que j'ai supervisé (Dominique Meyer et Jochen Brüggemann), que j'ai étudié plus en détail les NEMS à proximité d'une instabilité mécanique [19–21]. Pendant cette même période, avec Eros Mariani, nous avons progressé dans notre compréhension des résonances paramétriques dans les systèmes fermioniques à

plusieurs corps [22]. C'est également au cours de ces années de postdoc à l'IPCMS que, en collaboration avec Dietmar Weinmann, nous avons prédit l'existence de magnétoplasmons de surface dans les nanoparticules métalliques [23], une prédiction qui a été récemment confirmée expérimentalement [24, 25].

En novembre 2011, j'ai été nommé en tant que Maître de Conférences à l'Université de Strasbourg, dans l'Équipe de Physique Mésoscopique à l'IPCMS, un poste que j'ai débuté en septembre 2012. Avec Eros Mariani, deux de ses doctorants (Claire Woollacott et Tom Sturges) et en collaboration avec Bill Barnes (Université d'Exeter) et Ortwin Hess (Imperial College de Londres), nous avons alors commencé un projet sur le graphène artificiel plasmonique, où des nanoparticules métalliques forment un réseau en nid d'abeilles et où l'interaction en champ proche entre elles conduit à des modes collectifs qui se comportent comme les électrons dans le graphène [26–28]. Une telle ligne de recherche a ensuite motivé d'autres travaux sur la façon dont les plasmons se couplent à la lumière dans des réseaux plasmoniques tri-dimensionnels [29], et comment les plasmons collectifs se désintègrent dans des réseaux de nanoparticules métalliques en interaction [30]. Ce dernier sujet est l'objet de la thèse de doctorat d'Adam Brandstetter-Kunc, que je cosupervise avec Rodolfo Jalabert. Récemment, je me suis également impliqué dans le problème de la phase de transmission d'une boîte quantique dans une collaboration avec Rodolfo Jalabert, Hans Weidenmüller (Institut Max Planck de Heidelberg) et Dietmar Weinmann [31].

Les différents systèmes de matière condensée que j'étudie (nanoparticules métalliques, nanorésonateurs, nanotubes de carbone, molécules uniques, boîtes quantiques semiconductrices, etc.) ont en commun leur petite taille (de quelques nanomètres à quelques micromètres). En effet, ces systèmes sont suffisamment petits (et/ou à suffisamment basse température) de sorte que la cohérence de phase est préservée et des effets quantiques apparaissent dans diverses propriétés de ces systèmes.¹ Toutefois, ces systèmes contiennent encore un nombre relativement important de particules, assez grand de telle sorte qu'une description statistique est souvent nécessaire. L'approche appropriée pour aborder les diverses questions décrites dans cette habilitation à diriger des recherches est donc celle de la physique mésoscopique [32–34], comme illustrée dans les différents chapitres du manuscrit.

Le document contient trois chapitres résumant mes activités de recherche sur les nanosystèmes électromécaniques (chapitre 1), sur les métamatériaux plasmoniques (chapitre 2), et sur les systèmes fermioniques à plusieurs corps modulés paramétriquement (chapitre 3).² Chacun de ces chapitres peut être lu indépendamment. Le chapitre 4 présente mes projets de recherche en cours à l'IPCMS et conclut le manuscrit.

Le chapitre 1 décrit nos activités de recherche visant à comprendre le sort d'une instabilité mécanique dans un résonateur nanométrique (comme, par exemple, un nanotube de carbone suspendu) lorsqu'un courant électrique traverse le système. En raison du couplage entre les degrés de liberté mécaniques et électroniques, le flux de courant modifie inévitablement les propriétés mécaniques du nanorésonateur, et donc la nature même de l'instabilité mécanique. En raison de la rétroaction du nanorésonateur sur les degrés de liberté électroniques, les propriétés de transport du dispositif sont également modifiées. En particulier, nous montrons au chapitre 1 comment l'instabilité d'Euler, qui est le paradigme d'une instabilité mécanique continue, peut

¹ D'où le titre de ce manuscrit.

² Pour des raisons de cohérence thématique et par souci de concision, j'ai décidé de ne pas inclure dans le manuscrit notre travail [31] sur la phase de transmission des boîtes quantiques. En outre, alors que les références [13] et [23] portent sur des sujets liés au chapitre 1 et aux chapitres 2 & 3, respectivement, ces deux travaux ne sont pas résumés dans le manuscrit et peuvent être lu indépendamment.

être exploitée afin d'augmenter efficacement de plusieurs ordres de grandeur l'effet du couplage électromécanique sur la caractéristique courant-tension et le bruit en courant du système. Nous montrons en outre qu'un couplage électron-phonon intrinsèque au nanorésonateur modifie qualitativement la nature de l'instabilité d'Euler, en la modifiant en une instabilité discontinue pour certaines plages de paramètres.

Le chapitre 2 résume nos activités récentes dans le domaine des métamatériaux plasmoniques et du graphène artificiel. Nous montrons dans ce chapitre qu'un réseau en nid d'abeilles de nanoparticules métalliques, supportant chacune un plasmon de surface localisé et interagissant via leurs champs proches, présente des modes plasmoniques collectifs qui imitent les propriétés uniques des électrons dans le graphène. En effet, lorsque la polarisation des plasmons pointe dans une direction à proximité de la normale au plan du réseau en nid d'abeilles de nanoparticules, le spectre présente des cônes de Dirac, semblables à ceux présents dans la structure de bande électronique du graphène. Nous montrons que les états propres plasmoniques correspondants représentent des excitations bosoniques de type Dirac sans masse qui présentent des effets similaires aux électrons dans le graphène, tels qu'une phase de Berry non triviale et l'absence de rétrodiffusion par des inhomogénéités. Nous discutons en outre comment on peut manipuler les points de Dirac dans la zone de Brillouin et créer une bande interdite dans la dispersion des plasmons collectifs, ceci en modifiant la polarisation des plasmons de surface localisés, ouvrant ainsi la voie à un analogue plasmonique du graphène entièrement modulable. Puisque des phénomènes d'amortissement limiteront inévitablement la propagation des plasmons collectifs, nous étudions en détail au chapitre 2 la question cruciale de la durée de vie limitée des modes plasmoniques couplés, et nous analysons comment ces excitations bosoniques se couplent à la lumière dans une situation de couplage lumière-matière fort.

Dans le chapitre 3, nous explorons les résonances paramétriques dans les systèmes fermioniques à plusieurs corps. Nous commençons par montrer que la modulation périodique des paramètres du hamiltonien d'un système uni-dimensionnel de fermions corrélés peut être utilisée pour amplifier paramétriquement leurs modes collectifs bosoniques. En traitant le problème par une approche de type liquide de Luttinger, nous montrons comment les densités d'onde de charges et de spins sont simultanément amplifiées. Nous discutons de la mise en œuvre de nos prédictions pour des systèmes d'atomes froids uni-dimensionnels dans des réseaux optiques modulés. De façon remarquable, nous montrons que la distribution d'impulsions des fermions du gaz fournit directement une signature claire de la séparation spin-charge. Nous étendons ensuite ces idées au cas difficile des systèmes à deux dimensions. En particulier, nous montrons que les modes collectifs magnétoplasmoniques dans des boîtes quantiques quasi-bidimensionnelles à base de semiconducteurs peuvent être amplifiés paramétriquement en modulant périodiquement le champ magnétique perpendiculaire à la nanostructure. Les deux modes magnétoplasmoniques sont excités et amplifiés simultanément, conduisant à une augmentation exponentielle du nombre d'excitations bosoniques dans le système. Nous démontrons en outre que les mécanismes d'amortissement ainsi que les anharmonicités dans le confinement de la boîte quantique conduisent à une saturation de l'amplification paramétrique.

Enfin, le chapitre 4 décrit notre projet de recherche qui vise à étudier de nouveaux métamatériaux quantiques basés sur des nanoparticules métalliques. Ces métamatériaux font l'objet d'études expérimentales poussées à l'IPCMS et ailleurs. Notre projet vise à apporter un soutien théorique à ces expériences. Plus précisément, une première partie du projet vise à comprendre le magnétisme inhabituel observé dans des nanoparticules d'or [35–39]. En particulier, nous prévoyons d'étudier le magnétisme orbital d'assemblages de nanoparticules métalliques et de

déterminer si les comportements magnétiques observés peuvent être pris en compte par ce mécanisme. Une deuxième partie du projet est consacrée à l'étude des propriétés des plasmons polaritons dans les réseaux de nanoparticules en nid d'abeilles [26–28] afin de prédire des signatures expérimentales claires de ce réseau particulier de nanoparticules.

Outre mes activités de recherche brièvement exposées ci-dessus, une partie importante de mon temps est consacrée à l'enseignement. J'ai effectivement la chance d'enseigner depuis le début de mon doctorat en 2003, à l'exception de mes années en tant que postdoc à Strasbourg, qui, a contrario de mon postdoc à Berlin, ne comprenaient pas une tâche d'enseignement. En tant que Maître de Conférences, je suis actuellement responsable de trois enseignements à l'Université de Strasbourg.³ Le premier de ces enseignements est un cours intégré d'électromagnétisme pour les étudiants de deuxième année de la filière Mathématiques et Physique Approfondies. Le second est un cours intégré de mécanique classique et de relativité restreinte pour les étudiants du Master MEEF préparant le concours du CAPES. Le troisième cours dans lequel j'interviens est la physique statistique au niveau M1 où j'enseigne les travaux dirigés.

Résumé du chapitre 1 – Nanosystèmes électromécaniques proches d'une instabilité mécanique

La déformation élastique d'une tige par une force de compression longitudinale F appliquée à ses deux extrémités constitue le paradigme d'une instabilité mécanique, appelée instabilité d'Euler ou flambage [16]. Ce phénomène a été étudié pour la première fois par Euler en 1744 alors qu'il cherchait à déterminer la charge maximale que peut soutenir une colonne [17]. Tant que F reste en dessous d'une certaine force critique F_c , la tige reste droite, alors que pour $F > F_c$, la tige se courbe, comme esquissé sur les figures A.1(a) et A.1(b). La transition entre les deux états est continue et la fréquence du mode fondamental de flexion s'annule à l'instabilité.

Il y a eu récemment un intérêt grandissant dans l'exploration de l'instabilité d'Euler dans des systèmes micro- et nanomécaniques. Dans la quête pour comprendre les propriétés mécaniques remarquables des nanotubes de carbone [40–42], le flambage et d'autres instabilités mécaniques ont été observés dans ces systèmes [43]. L'instabilité d'Euler a été observée dans des nanorésonateurs de SiO_2 et il a été montré que, malgré la petite taille de ces objets, ils sont régis par la théorie classique et continue de l'élasticité [44, 45]. Des travaux théoriques ont étudié les propriétés quantiques de nanorésonateurs près de l'instabilité d'Euler [48–52], proposant ce système comme candidat potentiel pour observer les fluctuations de point zéro d'un mode mécanique [49] ou servir de qubit mécanique [51, 52].

Dans le chapitre 1, nous étudions l'interaction du courant avec le mouvement vibratoire à proximité de ces instabilités mécaniques continues, ce qui constitue une question fondamentale de la nano-électro-mécanique [10–12]. De façon remarquable, nous montrons que dans des conditions assez générales, ce problème admet une solution essentiellement exacte en raison de la continuité de l'instabilité et du fait que la fréquence de vibration du nanorésonateur s'annule à la transition (« ralentissement critique »). En effet, l'annulation de la fréquence implique que le mouvement mécanique devient lent par rapport à la dynamique électronique, et une approximation hors-équilibre de Born-Oppenheimer devient asymptotiquement exacte

³ http://www.ipcms.unistra.fr/?page_id=12753

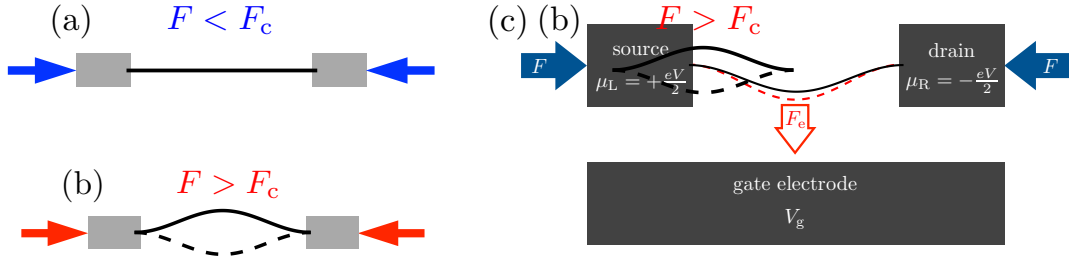


Fig. A.1: Représentation schématique d'un nanorésonateur (a) dans son état plat et (b) son état courbé avec deux positions métastables du faisceau (lignes continue et tirée). (c) Schéma d'un nanorésonateur suspendu formant une boîte quantique (ligne continue noire) connecté via des barrières tunnels à des électrodes source et drain, maintenues à des potentiels chimiques μ_L et μ_R par la tension V . La force latérale F comprime le nanorésonateur et induit le flambage. Le faisceau est couplé capacitivement à une électrode métallique maintenue à une tension de grille V_g . Ceci induit une force stochastique F_e qui attire le nanorésonateur vers la grille dès que la boîte quantique est chargée (ligne tirée rouge), engendrant des fluctuations de la déflexion du nanorésonateur, et, en retour, des fluctuations de courant à travers le système.

près de la transition. Dans le chapitre 1, nous illustrons notre cadre général en l'appliquant aux nanosystèmes électromécaniques proches de l'instabilité d'Euler. Nous montrons que l'interaction du transport électronique et de l'instabilité mécanique provoque des changements qualitatifs importants tant dans la nature de la déformation que dans les propriétés de transport électronique.

Les nanosystèmes électromécaniques dans lesquels un résonateur nanomécanique est couplé à des degrés de liberté électroniques [10–12] au travers, par exemple, d'un transistor à un électron (SET : Single-Electron Transistor), montrent des effets spectaculaires résultant du couplage de la partie mécanique du dispositif à la charge électronique. Ces effets surviennent en raison de la taille réduite du nanorésonateur, de sorte que la rétroaction du degré de liberté mécanique sur le SET peut avoir des conséquences importantes pour les propriétés de transport. Un exemple bien connu est le blocage du courant à faible tension qui se produit dans le régime du blocage de Coulomb lorsque le nanorésonateur est capacitivement couplé au SET [53,54]. La présence d'un électron supplémentaire de charge $-e < 0$ sur l'îlot central formant une boîte quantique sur la structure vibrante suspendue induit une force électrostatique F_e sur le résonateur, en déplaçant la position à l'équilibre de ce dernier par une quantité F_e/k , avec k la constante de raideur de l'oscillateur [voir la figure A.1(c)]. Ceci induit un décalage de la tension de grille $V_g \sim F_e^2/ek$ vu par le SET, et, par conséquent, un blocage du courant à travers le dispositif pour des tensions source-drain $V \lesssim F_e^2/ek$. Ce phénomène représente la contrepartie classique du phénomène de blocage de Franck-Condon dans les dispositifs moléculaires [55,56] qui a été observé récemment dans les résonateurs à base de nanotubes de carbone pour un mode vibrationnel longitudinal à haute énergie [58]. Pour les nanorésonateurs classiques, le blocage en courant n'a, à notre connaissance, jamais été observé expérimentalement en raison du relativement faible couplage électromécanique F_e au mode de flexion de la nanostructure suspendue, même si un précurseur de cet effet a été récemment reporté dans la littérature [41,42].

Après avoir introduit le sujet dans la section 1.1, nous montrons dans la section 1.2 comment

on peut augmenter le blocage classique du courant par plusieurs ordres de grandeur, ceci en exploitant l'instabilité d'Euler. En effet, la constante de raideur du nanorésonateur k (ou de manière équivalente, la fréquence de vibration du mode fondamental de flexion ω) tend vers zéro quand on amène à l'aide d'une force de compression longitudinale F le nanorésonateur à l'instabilité mécanique (voir la figure A.1). Ainsi, l'échelle d'énergie F_e^2/k à laquelle le blocage de courant se produit augmente considérablement, rendant ce phénomène potentiellement observable dans des expériences ultérieures.

Outre le couplage capacitif mentionné ci-dessus et ayant pour conséquence l'effet de blocage de courant classique, il existe un couplage qui résulte de l'interaction électron-phonon qui est intrinsèque au nanotube [61]. Dans la section 1.3, nous montrons que ce couplage modifie *qualitativement* la nature de l'instabilité d'Euler. En effet, la dynamique électronique peut changer la nature de l'instabilité, qui devient discontinue. Ceci est analogue au comportement tricritique dans la théorie de Landau des transitions de phase.

Publications reliées

- F. Elste, G. Weick, C. Timm, F. von Oppen
Current-induced conformational switching in single-molecule junctions
[Appl. Phys. A **93**, 345 \(2008\)](#)
- G. Weick, F. Pistolesi, E. Mariani, F. von Oppen
Discontinuous Euler instability in nanoelectromechanical systems
[Phys. Rev. B **81**, 121409\(R\) \(2010\)](#)
- G. Weick, F. von Oppen, F. Pistolesi
Euler buckling instability and enhanced current blockade in suspended single-electron transistor
[Phys. Rev. B **83**, 035420 \(2011\)](#)
- G. Weick, D. M.-A. Meyer
Cotunneling, current blockade, and backaction forces in nanobeams close to the Euler buckling instability
[Phys. Rev. B **84**, 125454 \(2011\)](#)
- J. Brüggemann, G. Weick, F. Pistolesi, F. von Oppen
Large current noise in nanoelectromechanical systems close to continuous mechanical instabilities
[Phys. Rev. B **85**, 125441 \(2012\)](#)

Résumé du chapitre 2 – Un analogue plasmonique du graphène

La lumière est une source d'inspiration pour la pensée scientifique depuis des millénaires. Déjà les Assyriens avaient développé les premières lentilles afin de courber la trajectoire de la lumière et de contrôler sa propagation. Contrairement à l'échelle macroscopique, l'utilisation de la lumière pour observer des structures microscopiques pose des difficultés en raison de la limite de diffraction [88]. Dans le but de surmonter cette limite et d'observer des structures de taille sub-longueur d'onde, des nanostructures plasmoniques ont été créées [89, 90], telles que des

nanoparticules métalliques isolées [91]. Le champ évanescent à la surface de la nanoparticule associé à la résonance plasmon de surface [92] produit une forte augmentation du champ électromagnétique dans la région sub-longueur d'onde, permettant ainsi de surmonter la limite de diffraction et d'obtenir une résolution à l'échelle moléculaire [93].

Alors que le domaine de la plasmonique se concentre principalement sur des structures uniques ou formées de quelques composants, la création de réseaux ordonnés de nanoparticules constitue un pont vers le domaine des métamatériaux. Les métamatériaux plasmoniques présentent des propriétés uniques qui vont au-delà de l'optique traditionnelle, comme l'apparition d'un indice de réfraction négatif [94–96], les lentilles « parfaites » [97,98], la perspective passionnante de la cape d'invisibilité [99–101], les arcs-en-ciel piégés et la lumière « lente » [102], ainsi que la capacité à effectuer des opérations mathématiques simples [103]. En effet, dans les métamatériaux plasmoniques, l'interaction entre plasmons de surface localisés sur les nanoparticules individuelles génère des modes plasmoniques étendus impliquant tous les plasmons à la fois, comme cela a été exploré expérimentalement dans des réseaux uni- et bi-dimensionnels de nanoparticules d'or [104–106] et d'argent [107–109], ainsi qu'étudié théoriquement au moyen de calculs électromagnétiques classiques [110–115]. La compréhension de la nature et les propriétés de ces modes plasmoniques collectifs est d'une importance capitale car ils sont le canal de guidage du rayonnement électromagnétique sur des distances macroscopiques, tout en étant confinés latéralement.

Les plasmons collectifs dans des réseaux périodiques de nanoparticules métalliques sont un domaine très actif de recherche de la plasmonique [116]. En effet, l'interaction des résonances de plasmons de surface localisés peut conduire à des changements dramatiques dans la réponse optique globale de ces structures. Par exemple, il est à la fois prédit [117, 118] et observé [119–121] que la réponse plasmonique d'un réseau périodique de nanoparticules peut être considérablement moins atténuée par rapport à la réponse de particules uniques si la séparation inter-particule est de l'ordre de la longueur d'onde de résonance du plasmon de surface localisé. D'autres travaux ont montré que ces résonances couplées sont pertinentes pour des applications dans l'émission de la lumière [122]. Les réseaux de nanoparticules métalliques peuvent être conçus afin de présenter par exemple des « stop-bands » [123] et sont également intensivement étudiés dans le contexte des dispositifs photovoltaïques [124].

La relation de dispersion des plasmons collectifs et leur nature physique dépendent de façon cruciale du type de réseau que présente le métamatériau, ainsi que de l'interaction microscopique entre les plasmons de surface localisés. Un réseau qui a généré récemment un très grand intérêt dans la communauté des physiciens de la matière condensée est la structure en nid d'abeilles que présente le graphène, une monocouche bidimensionnelle d'atomes de carbone [125]. Dans le cas du graphène, le recouvrement des orbitales électroniques entre atomes voisins donne lieu à une structure de bande très riche, caractérisée par la présence de quasiparticules fermioniques de Dirac sans masse à basse énergie [126,127]. La chiralité associée à ces fermions de Dirac pseudo-relativistes résulte en plusieurs des propriétés remarquables du graphène, telle qu'une phase de Berry non triviale accumulée en transport parallèle [128,129], ainsi que la suppression de la rétrodiffusion électronique par des impuretés [130]. Sans aucun doute, il serait désirable de prendre avantage des propriétés physiques remarquables des électrons dans le graphène dans des métamatériaux plasmoniques convenablement conçus, ceci en analysant le hamiltonien et la nature des modes propres de plasmons collectifs dans un réseau en nid d'abeilles de nanoparticules métalliques. Ceci est l'objet du chapitre 2.

Après avoir introduit le problème dans la section 2.1, nous étudions en détail dans la sec-

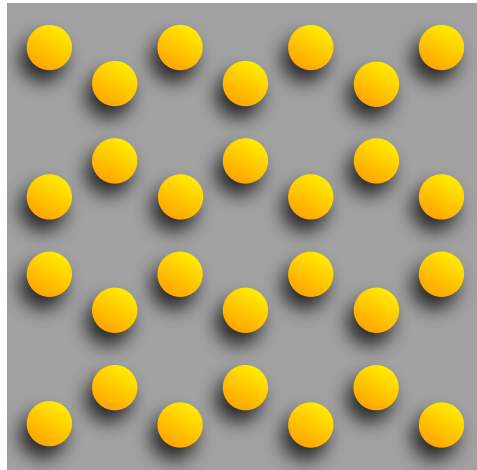


Fig. A.2: Représentation schématique d'un réseau de nanoparticules métalliques en nid d'abeilles.

tion 2.2 les propriétés des modes plasmoniques étendus dans un réseau en nid d'abeilles de nanoparticules (voir figure A.2) et nous montrons que ces modes représentent en effet des excitations chirales de type Dirac sans masse. Puisque l'amortissement de ces modes, qui limitera inévitablement leur propagation dans le réseau, est d'un intérêt crucial pour des applications potentielles, nous étudions dans la section 2.3 la désintégration de plasmons dans un système plus simple qui constitue cependant la brique élémentaire de tout métamatériau plasmonique, à savoir un dimère de nanoparticules. Un autre point d'intérêt crucial en vue d'applications possibles des excitations plasmoniques de type Dirac est leur couplage à la lumière. Motivé par ce problème, nous étudions dans la section 2.4 comment les plasmons collectifs se couplent à la lumière, formant ainsi des plasmons-polaritons dans une situation de couplage fort.

Publications reliées

- G. Weick, D. Weinmann
Lifetime of the surface magnetoplasmons in metallic nanoparticles
[Phys. Rev. B **83**, 125405 \(2011\)](#)
- G. Weick, C. Woollacott, W.L. Barnes, O. Hess, E. Mariani
Dirac-like plasmons in honeycomb lattices of metallic nanoparticles
[Phys. Rev. Lett. **110**, 106801 \(2013\)](#)
- E. Mariani, G. Weick
A plasmonic analogue of graphene
[SPIE Newsroom, DOI:10.1117/2.1201411.005673 \(2014\)](#)
- G. Weick, E. Mariani
Tunable plasmon polaritons in arrays of interacting metallic nanoparticles
[Eur. Phys. J. B **88**, 7 \(2015\)](#)

- A. Brandstetter-Kunc, G. Weick, D. Weinmann, R.A. Jalabert
Decay of dark and bright plasmonic modes in a metallic nanoparticle dimer
Phys. Rev. B **91**, 035431 (2015)
- T.J. Sturges, C. Woollacott, G. Weick, E. Mariani
Dirac plasmons in bipartite lattices of metallic nanoparticles
2D Mater. **2**, 014008 (2015); focus issue on artificial graphene

Résumé du chapitre 3 – Résonances paramétriques dans les systèmes fermioniques à plusieurs corps

La balançoire est l'exemple le plus connu d'un système classique présentant une résonance paramétrique [186]. En effet, la modulation de la longueur effective de la balançoire grâce au mouvement des jambes entraîne une amplification exponentielle du mouvement de la balançoire, ceci si la fréquence de modulation est égale à deux fois la fréquence naturelle du pendule associé. En quantifiant ce problème classique et en considérant un oscillateur harmonique quantique dont la fréquence est modulée de façon paramétrique, on se rend compte que les opérateurs création et annihilation de quanta de vibration sont amplifiés exponentiellement en fonction du temps [22]. Cet effet est particulièrement fort si la fréquence de modulation est à peu près deux fois la fréquence naturelle de l'oscillateur.

Dans un système de plusieurs bosons en interaction, ceux dont la fréquence remplit la condition de résonance seront amplifiés, faisant de la résonance paramétrique un outil spectroscopique dans les systèmes à plusieurs corps. Ces idées ont acquis récemment une importance particulière depuis l'avènement des pièges optiques pour les gaz d'atomes froids [187]. En effet, une résonance paramétrique peut être engendrée lorsque l'intensité des lasers piégeant les atomes est modulée périodiquement en temps [188]. Du point de vue théorique, l'amplification paramétrique de quasiparticules de Bogoliubov pour des gaz d'atomes bosoniques dans des réseaux optiques a déjà été étudiée dans le passé [189, 190]. Dans ces systèmes, la nature bosonique des quasiparticules apparaît déjà lorsque les interactions sont traitées en champ moyen, et permet à l'amplification de se produire.

Dans le chapitre 3, nous analysons les résonances paramétriques dans les systèmes *fermioniques* à plusieurs corps, en commençant par la question cruciale de savoir si l'amplification peut se produire. En effet, contrairement au cas des bosons, dans les systèmes fermioniques tout traitement de champ moyen des interactions, y compris en présence de brisures de symétries, préserve la nature fermionique des quasiparticules. Le principe de Pauli bloque ainsi leur amplification, comme on peut facilement le vérifier par calcul direct [22]. La question qui se pose alors est si des modes collectifs bosoniques d'un système à plusieurs corps fermionique peuvent être soumis à une amplification par la modulation d'un paramètre du hamiltonien microscopique du système.

Afin de répondre à cette question fondamentale, nous devons traiter les corrélations dans un système fermionique au-delà du champ moyen. Après une introduction au sujet (section 3.1), dans la section 3.2 nous limitons donc notre analyse au cas de fermions en interaction à une dimension, où la théorie du liquide de Luttinger permet de prendre en compte les interactions et où apparaît naturellement des modes collectifs d'ondes de densité de charge et de spin [191, 192].

Étendre les idées exposées ci-dessus aux cas de systèmes fermioniques à plusieurs corps bi- ou tri-dimensionnels est un formidable défi théorique, car il faut capturer les corrélations

pertinentes en traitant les interactions au-delà du champ moyen. Ceci est une tâche très difficile et non triviale à réaliser. Dans la section 3.3, nous nous concentrons sur le cas des systèmes fermioniques à plusieurs corps *confinés*, où les modes collectifs existent en raison de la taille finie du système [167]. Des exemples de ces modes collectifs sont les excitations de plasmons qui correspondent au mouvement du centre de masse électronique dans des nanoparticules métalliques [167] (voir chapitre 2) et dans des boîtes quantiques quasi-bidimensionnelles à base de semiconducteurs [169,194].

Publications reliées

- C. D. Graf, G. Weick, E. Mariani
Parametric resonance and spin-charge separation in 1D fermionic systems
[EPL **89**, 40005 \(2010\)](#)
- G. Weick, D. Weinmann
Lifetime of the surface magnetoplasmons in metallic nanoparticles
[Phys. Rev. B **83**, 125405 \(2011\)](#)
- G. Weick, E. Mariani
Parametric amplification of magnetoplasmons in semiconductor quantum dots
[Phys. Rev. B **84**, 125441 \(2011\)](#)

Résumé du chapitre 4 – Projet de recherche : nouveaux métamatériaux quantiques basés sur des nanoparticules métalliques

Du fait de leurs petites tailles, les nanoparticules métalliques présentent des effets quantiques spectaculaires. La plupart de ces effets proviennent du confinement des états propres électroniques, ce confinement étant dû au relativement grand rapport surface-sur-volume de particules de tailles nanométriques [223, 224]. La preuve la plus frappante de la quantification des états électroniques dans les nanoparticules métalliques est la structure électronique en couche, observée pour la première fois par Knight et collaborateurs en 1984 [225]. Les effets de taille résultants apparaissent dans la plupart des propriétés physiques des amas métalliques, par exemple dans leur spectre d'abondance, dans la polarisabilité dipolaire statique, le potentiel d'ionisation, et les propriétés optiques [226, 227].

Une fois que les nanoparticules métalliques sont mises ensembles et interagissent entre elles et/ou avec le milieu environnant, elles forment des métamatériaux avec des propriétés intrigantes qui sont différentes de celles des nanoparticules individuelles et isolées. Ces métamatériaux à base de nanoparticules font l'objet d'actives recherches expérimentales à l'IPCMS et ailleurs, et notre projet de recherche vise à apporter un soutien théorique à ces expériences.

Les métamatériaux à base de nanoparticules présentent un large éventail de propriétés particulières qui peuvent être très différentes de celles des briques élémentaires. Notre projet met l'accent sur deux de ces propriétés : les propriétés magnétiques et optiques. Plus précisément, un aspect qui a attiré une attention considérable au cours de la dernière décennie est le comportement magnétique inhabituel d'ensembles de nanoparticules d'or. En effet, tandis que l'or est diamagnétique dans le massif, plusieurs expériences ont montré que les ensembles

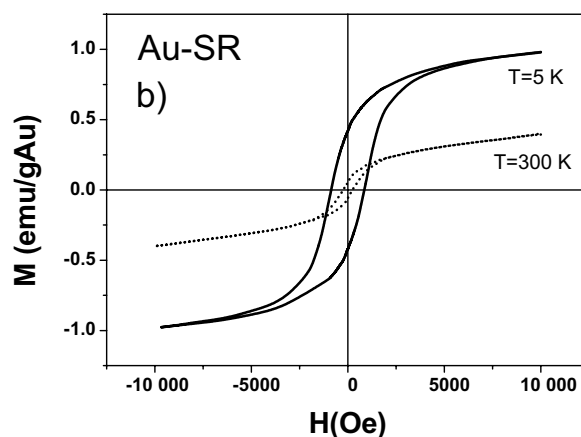


Fig. A.3: Courbes d'aimantation de nanoparticules d'or fonctionnalisées avec des ligands thiols (Au-SR) à des températures de 5 K (ligne continue) et 300 K (ligne tirée). Reproduit de la référence [35].

de nanoparticules d'or recouvertes avec des ligands organiques peuvent présenter un comportement ferromagnétique de l'aimantation [35–38] (voir figure A.3). D'autres échantillons montrent un comportement de type paramagnétique, et quelques autres un diamagnétisme qui est généralement plus fort que dans le massif.⁴ Ces différentes propriétés magnétiques qui varient d'un échantillon à l'autre, ainsi que les mécanismes sous-jacents à l'origine de ces caractéristiques sont une source d'intenses débats dans la communauté. Une interprétation des propriétés magnétiques inhabituelles d'ensembles de nanoparticules d'or qui a été récemment proposée par l'équipe de Jean-Louis Gallani du Département des Matériaux Organiques (DMO) de l'IPCMS est qu'elles pourraient être de caractère orbital, indépendantes des molécules entourant les nanoparticules. Notre projet vise à étudier le magnétisme orbital des assemblées de nanoparticules et de déterminer si ces comportements magnétiques intrigants peuvent être pris en compte par ce mécanisme.

D'autres aspects fascinants des métamatériaux à base de nanoparticules résident dans leurs propriétés optiques. Alors que le domaine de la plasmonique se concentre principalement sur des structures simples, la création de réseaux ordonnés de nanoparticules constitue un pont vers le domaine des métamatériaux [116]. Il en résulte des métamatériaux plasmoniques qui présentent des propriétés uniques au-delà de l'optique traditionnelle. Dans le chapitre 2, nous avons démontré théoriquement que les plasmons collectifs dans un réseau plasmonique en nid d'abeilles se comportent comme des excitations bosoniques de type Dirac sans masse [26, 28]. Ces excitations doivent donc présenter des propriétés similaires aux électrons dans le graphène, comme une phase de Berry non triviale et l'absence de rétrodiffusion due aux impuretés. L'objectif de notre projet de recherche est d'exploiter les propriétés inhabituelles des plasmons collectifs dans des réseaux plasmoniques en nid d'abeilles, et d'en tirer des connaissances approfondies afin de proposer des métamatériaux avec des propriétés nouvelles.

Ce projet de recherche est depuis octobre 2014 financé par l'Agence Nationale de la Recherche dans le cadre de l'appel à projet générique « Jeunes Chercheurs », et ceci pour une durée de

⁴ Pour un état de l'art récent des propriétés magnétiques des nanoparticules d'or, voir l'article de revue [39].

4 ans (projet ANR-14-CE26-0005 Q-MetaMat « Nouveaux Métamatériaux Quantiques Basés sur des Nanoparticules métalliques »).⁵ Notre projet est également supporté par le programme PICS du CNRS depuis janvier 2014, et ceci pour trois années (contrat No. 6384 APAG, « Un Analogue Plasmonique du Graphène ») dans le cadre de notre collaboration très fructueuse avec Eros Mariani de l'Université d'Exeter au Royaume-Uni.

⁵ http://www.ipcms.unistra.fr/?page_id=21342

Bibliography

- [1] J.-Y. Bigot, J. Y. Merle, O. Cregut, and A. Daunois, *Electron dynamics in copper metallic nanoparticles probed with femtosecond optical pulses*, Phys. Rev. Lett. **75**, 4702 (1995).
- [2] V. Halté, J. Guille, J.-C. Merle, I. Perakis, and J.-Y. Bigot, *Electron dynamics in silver nanoparticles: Comparison between thin films and glass embedded nanoparticles*, Phys. Rev. B **60**, 11738 (1999).
- [3] J.-Y. Bigot, V. Halté, J.-C. Merle, and A. Daunois, *Electron dynamics in metallic nanoparticles*, Chem. Phys. **251**, 181 (2000).
- [4] G. Weick, R. A. Molina, D. Weinmann, and R. A. Jalabert, *Lifetime of the first and second collective excitations in metallic nanoparticles*, Phys. Rev. B **72**, 115410 (2005).
- [5] G. Weick, G.-L. Ingold, R. A. Jalabert, and D. Weinmann, *Surface plasmon in metallic nanoparticles: Renormalization effects due to electron-hole excitations*, Phys. Rev. B **74**, 165421 (2006).
- [6] G. Weick, *Quantum dissipation and decoherence of collective excitations in metallic nanoparticles* (PhD thesis, Universität Augsburg & Université Louis Pasteur, Strasbourg, 2006).
- [7] G. Weick, D. Weinmann, G.-L. Ingold, and R. A. Jalabert, *Anomaly in the relaxation dynamics close to the surface plasmon resonance*, EPL **78**, 27002 (2007).
- [8] C. Seoanez, G. Weick, R. A. Jalabert, and D. Weinmann, *Friction of the surface plasmon by high-energy particle-hole pairs*, Eur. Phys. J. D **44**, 351 (2007).
- [9] G. Weick, G.-L. Ingold, D. Weinmann, and R. A. Jalabert, *Sidebands in the light absorption of driven metallic nanoparticles*, Eur. Phys. J. D **44**, 359 (2007).
- [10] H. G. Craighead, *Nanoelectromechanical systems*, Science **290**, 1532 (2000).
- [11] K. L. Ekinici and M. L. Roukes, *Nanoelectromechanical systems*, Rev. Sci. Instrum. **76**, 061101 (2005).
- [12] M. Poot and H. S. J. van der Zant, *Mechanical systems in the quantum regime*, Phys. Rep. **511**, 273 (2012).
- [13] F. Elste, G. Weick, C. Timm, and F. von Oppen, *Current-induced conformational switching in single-molecule junctions*, Appl. Phys. A **93**, 345 (2008).
- [14] N. Henningsen, K. J. Franke, I. F. Torrente, G. Schulze, B. Prievisch, K. Rück-Braun, J. Dokic, T. Klamroth, P. Saalfrank, and J. I. Pascual, *Inducing the rotation of a single phenyl ring with tunneling electrons*, J. Phys. Chem. C **111**, 14843 (2007).

Bibliography

- [15] G. Weick, F. Pistolesi, E. Mariani, and F. von Oppen, *Discontinuous Euler instability in nanoelectromechanical systems*, Phys. Rev. B **81**, 121409(R) (2010).
- [16] L. D. Landau and E. M. Lifshitz, *Theory of Elasticity* (Pergamon, Oxford, 1970).
- [17] L. Euler, in *Leonhard Euler's Elastic Curves*, translated and annotated by W. A. Oldfather, C. A. Ellis, and D. M. Brown, reprinted from ISIS, No. 58 XX(1), 1744 (Saint Catherine Press, Bruges).
- [18] C. D. Graf, G. Weick, and E. Mariani, *Parametric resonance and spin-charge separation in 1D fermionic systems*, EPL **89**, 40005 (2010).
- [19] G. Weick, F. von Oppen, and F. Pistolesi, *Euler buckling instability and enhanced current blockade in suspended single-electron transistors*, Phys. Rev. B **83**, 035420 (2011).
- [20] G. Weick and D. M.-A. Meyer, *Cotunneling, current blockade, and backaction forces in nanobeams close to the Euler buckling instability*, Phys. Rev. B **84**, 125454 (2011).
- [21] J. Brüggemann, G. Weick, F. Pistolesi, and F. von Oppen, *Large current noise in nanoelectromechanical systems close to continuous mechanical instabilities*, Phys. Rev. B **85**, 125441 (2012).
- [22] G. Weick and E. Mariani, *Parametric amplification of magnetoplasmons in semiconductor quantum dots*, Phys. Rev. B **84**, 125441 (2011).
- [23] G. Weick and D. Weinmann, *Lifetime of the surface magnetoplasmons in metallic nanoparticles*, Phys. Rev. B **83**, 125405 (2011).
- [24] F. Pineider, G. Campo, V. Bonanni, C. de Julián Fernández, G. Mattei, A. Caneschi, D. Gatteschi, and C. Sangregorio, *Circular magnetoplasmonic modes in gold nanoparticles*, Nano Lett. **13**, 4785 (2013).
- [25] Y. Ishikawa and H. Yao, *Surface magnetoplasmons in silver nanoparticles: Apparent magnetic-field enhancement manifested by simultaneous deconvolution of UV-vis absorption and MCD spectra*, Chem. Phys. Lett. **609**, 93 (2014).
- [26] G. Weick, C. Woollacott, W. L. Barnes, O. Hess, and E. Mariani, *Dirac-like plasmons in honeycomb lattices of metallic nanoparticles*, Phys. Rev. Lett. **110**, 106801 (2013).
- [27] E. Mariani and G. Weick, *A plasmonic analogue of graphene*, SPIE Newsroom, DOI:10.1117/2.1201411.005673 (2014).
- [28] T. J. Sturges, C. Woollacott, G. Weick, and E. Mariani, *Dirac plasmons in bipartite lattices of metallic nanoparticles*, 2D Mater. **2**, 014008 (2015).
- [29] G. Weick and E. Mariani, *Tunable plasmon polaritons in arrays of interacting metallic nanoparticles*, Eur. Phys. J. B **88**, 7 (2015).
- [30] A. Brandstetter-Kunc, G. Weick, D. Weinmann, and R. A. Jalabert, *Decay of dark and bright plasmonic modes in a metallic nanoparticle dimer*, Phys. Rev. B **91**, 035431 (2015).

- [31] R. A. Jalabert, G. Weick, H. A. Weidenmüller, and D. Weinmann, *Transmission phase of a quantum dot and statistical fluctuations of partial-width amplitudes*, Phys. Rev. E **89**, 052911 (2014).
- [32] E. Akkermans, G. Montambaux, J.-L. Pichard, and J. Zinn-Justin (eds.), *Mesoscopic Quantum Physics* (Les Houches 1994, Session LXI).
- [33] Y. Imry, *Introduction to Mesoscopic Physics* (Oxford University Press, Oxford, 2002).
- [34] E. Akkermans and G. Montambaux, *Mesoscopic Physics of Electrons and Photons* (Cambridge University Press, Cambridge, 2007).
- [35] P. Crespo, R. Litrán, T. C. Rojas, M. Multigner, J. M. de la Fuente, J. C. Sánchez-López, M. A. García, A. Hernando, S. Penadés, and A. Fernández, *Permanent magnetism, magnetic anisotropy, and hysteresis of thiol-capped gold nanoparticles*, Phys. Rev. Lett. **93**, 087204 (2004).
- [36] Y. Yamamoto, T. Miura, M. Suzuki, N. Kawamura, H. Miyagawa, T. Nakamura, K. Kobayashi, T. Teranishi, and H. Hori, *Direct observation of ferromagnetic spin polarization in gold nanoparticles*, Phys. Rev. Lett. **93**, 116801 (2004).
- [37] B. Donnio, P. García-Vázquez, J.-L. Gallani, D. Guillon, and E. Terazzi, *Dendronized ferromagnetic gold nanoparticles self-organized in a thermotropic cubic phase*, Adv. Mater. **19**, 3534 (2007).
- [38] B. Donnio, A. Derory, E. Terazzi, M. Drillon, D. Guillon, and J.-L. Gallani, *Very slow high-temperature relaxation of the remnant magnetic moment in 2 nm mesomorphic gold nanoparticles*, Soft Matter **6**, 965 (2010).
- [39] G. L. Nealon, B. Donnio, R. Greget, J.-P. Kappler, E. Terazzi, and J.-L. Gallani, *Magnetism in gold nanoparticles*, Nanoscale **4**, 5244 (2012).
- [40] P. Poncharal, Z. L. Wang, D. Ugarte, and W. A. de Heer, *Electrostatic deflections and electromechanical resonances of carbon nanotubes*, Science **283**, 1513 (1999).
- [41] G. A. Steele, A. K. Hüttel, B. Witkamp, M. Poot, H. B. Meerwaldt, L. P. Kouwenhoven, and H. S. J. van der Zant, *Strong coupling between single-electron tunneling and nanomechanical motion*, Science **325**, 1103 (2009).
- [42] B. Lassagne, Y. Tarakanov, J. Kinaret, D. Garcia-Sanchez, and A. Bachtold, *Coupling mechanics to charge transport in carbon nanotube mechanical resonators*, Science **325**, 1107 (2009).
- [43] M. R. Falvo, G. J. Harris, R. M. Taylor, V. Chi, F. P. Brooks, S. Washburn, and R. Superfine, *Bending and buckling of carbon nanotubes under large strain*, Nature **389**, 582 (1997).
- [44] S. M. Carr and M. N. Wybourne, *Elastic instability of nanomechanical beams*, Appl. Phys. Lett. **82**, 709 (2003).
- [45] S. M. Carr, W. E. Lawrence, and M. N. Wybourne, *Buckling cascade of free-standing mesoscopic beams*, Europhys. Lett. **69**, 952 (2005).

Bibliography

- [46] W. Bao, F. Miao, Z. Chen, H. Zhang, W. Jang, C. Dames, and C. N. Lau, *Controlled ripple texturing of suspended graphene and ultrathin graphite membranes*, Nature Nanotech. **4**, 562 (2009).
- [47] J. C. Meyer, A. K. Geim, M. I. Katsnelson, K. S. Novoselov, T. J. Booth, and S. Roth, *The structure of suspended graphene sheets*, Nature **446**, 60 (2007).
- [48] S. M. Carr, W. E. Lawrence, and M. N. Wybourne, *Accessibility of quantum effects in mesomechanical systems*, Phys. Rev. B **64**, 220101(R) (2001).
- [49] P. Werner and W. Zwerger, *Macroscopic quantum effects in nanomechanical systems*, Europhys. Lett. **65**, 158 (2004).
- [50] V. Peano and M. Thorwart, *Nonlinear response of a driven vibrating nanobeam in the quantum regime*, New J. Phys. **8**, 21 (2006).
- [51] S. Savel'ev, X. Hu, and F. Nori, *Quantum electromechanics: qubits from buckling nanobars*, New J. Phys. **8**, 105 (2006).
- [52] S. Savel'ev, A. L. Rakhmanov, X. Hu, A. Kasumov, and F. Nori, *Quantum electromechanics: Quantum tunneling near resonance and qubits from buckling nanoscale bars*, Phys. Rev. B **75**, 165417 (2007).
- [53] F. Pistolesi and S. Labarthe, *Current blockade in classical single-electron nanomechanical resonator*, Phys. Rev. B **76**, 165317 (2007).
- [54] F. Pistolesi, Y. M. Blanter, and I. Martin, *Self-consistent theory of molecular switching*, Phys. Rev. B **78**, 085127 (2008).
- [55] J. Koch and F. von Oppen, *Franck-Condon blockade and giant Fano factors in transport through single molecules*, Phys. Rev. Lett. **94**, 206804 (2005).
- [56] J. Koch, F. von Oppen, and A. V. Andreev, *Theory of the Franck-Condon blockade regime*, Phys. Rev. B **74**, 205438 (2006).
- [57] S. Sapmaz, P. Jarillo-Herrero, Y. M. Blanter, C. Dekker, and H. S. J. van der Zant, *Tunneling in suspended carbon nanotubes assisted by longitudinal phonons*, Phys. Rev. Lett. **96**, 026801 (2006).
- [58] R. Leturcq, C. Stampfer, K. Inderbitzin, L. Durrer, C. Hierold, E. Mariani, M. G. Schultz, F. von Oppen, and K. Ensslin, *Franck-Condon blockade in suspended carbon nanotube quantum dots*, Nature Phys. **5**, 327 (2009).
- [59] E. Burzurí, Y. Yamamoto, M. Warnock, X. Zhong, K. Park, A. Cornia, and H. S. J. van der Zant, *Franck-Condon blockade in a single-molecule transistor*, Nano Lett. **14**, 3191 (2014).
- [60] E. M. Weig, R. H. Blick, T. Brandes, J. Kirschbaum, W. Wegscheider, M. Bichler, and J. P. Kotthaus, *Single-electron-phonon interaction in a suspended quantum dot phonon cavity*, Phys. Rev. Lett. **92**, 046804 (2004).

- [61] E. Mariani and F. von Oppen, *Electron-vibron coupling in suspended carbon nanotube quantum dots*, Phys. Rev. B **80**, 155411 (2009).
- [62] A. K. Hüttel, G. A. Steele, B. Witkamp, M. Poot, L. P. Kouwenhoven, and H. S. J. van der Zant, *Carbon nanotubes as ultrahigh quality factor mechanical resonators*, Nano Lett. **9**, 2547 (2009).
- [63] S. Sapmaz, Y. M. Blanter, L. Gurevich, and H. S. J. van der Zant, *Carbon nanotubes as nanoelectromechanical systems*, Phys. Rev. B **67**, 235414 (2003).
- [64] W. Izumida and M. Grifoni, *Phonon-assisted tunnelling in interacting suspended single-wall carbon nanotubes*, New J. Phys. **7**, 244 (2005).
- [65] K. Flensberg, *Electron-vibron coupling in suspended nanotubes*, New J. Phys. **8**, 5 (2006).
- [66] Y. M. Blanter, O. Usmani, and Y. V. Nazarov, *Single-electron tunneling with strong mechanical feedback*, Phys. Rev. Lett. **93**, 136802 (2004), **94**, 049904(E) (2005).
- [67] D. Mozyrsky, M. B. Hastings, and I. Martin, *Intermittent polaron dynamics: Born-Oppenheimer approximation out of equilibrium*, Phys. Rev. B **73**, 035104 (2006).
- [68] R. Hussein, A. Metelmann, P. Zedler, and T. Brandes, *Semiclassical dynamics of nano-electromechanical systems*, Phys. Rev. B **82**, 165406 (2010).
- [69] A. Nocera, C. A. Perroni, V. Marigliano Ramaglia, and V. Cataudella, *Stochastic dynamics for a single vibrational mode in molecular junctions*, Phys. Rev. B **83**, 115420 (2011).
- [70] N. Bode, S. Viola Kusminskiy, R. Egger, and F. von Oppen, *Scattering theory of current-induced forces in mesoscopic systems*, Phys. Rev. Lett. **107**, 036804 (2011).
- [71] N. Bode, S. Viola Kusminskiy, R. Egger, and F. von Oppen, *Current-induced forces in mesoscopic systems: A scattering-matrix approach*, Beilstein J. Nanotechnol. **3**, 144 (2012).
- [72] R. Zwanzig, *Nonequilibrium Statistical Mechanics* (Oxford University Press, Oxford, 2001).
- [73] T. Novotný, A. Donarini, C. Flindt, and A.-P. Jauho, *Shot noise of a quantum shuttle*, Phys. Rev. Lett. **92**, 248302 (2004).
- [74] F. Pistolesi, *Full counting statistics of a charge shuttle*, Phys. Rev. B **69**, 245409 (2004).
- [75] A. D. Armour, *Current noise of a single-electron transistor coupled to a nanomechanical resonator*, Phys. Rev. B **70**, 165315 (2004).
- [76] C. Flindt, T. Novotný, and A.-P. Jauho, *Full counting statistics of nano-electromechanical systems*, Europhys. Lett. **69**, 475 (2005).
- [77] A. Donarini, T. Novotný, and A.-P. Jauho, *Simple models suffice for the single-dot quantum shuttle*, New J. Phys. **67**, 237 (2005).

Bibliography

- [78] O. Usmani, Y. M. Blanter, and Y. V. Nazarov, *Strong feedback and current noise in nanoelectromechanical systems*, Phys. Rev. B **75**, 195312 (2007).
- [79] Y. M. Blanter and M. Büttiker, *Shot noise in mesoscopic conductors*, Phys. Rep. **336**, 1 (2000).
- [80] P. Kloeden and E. Platen, *Numerical Solution of Stochastic Differential Equations* (Springer, Berlin, 1999).
- [81] S. Machlup, *Noise in semiconductors: spectrum of a two-parameter random signal*, J. Appl. Phys. **25**, 341 (1954).
- [82] H. A. Kramers, *Brownian motion in a field of force and the diffusion model of chemical reactions*, Physica **7**, 284 (1940).
- [83] P. Hänggi, P. Talkner, and M. Borkovec, *Reaction-rate theory: fifty years after Kramers*, Rev. Mod. Phys. **62**, 251 (1990).
- [84] C. Meyer zu Rheda, *Euler instability in suspended molecular quantum dots* (Bachelor thesis, Freie Universität Berlin & Université de Strasbourg, 2010).
- [85] P. M. Chaikin and T. C. Lubensky, *Principles of Condensed Matter Physics* (Cambridge University Press, Cambridge, 1995).
- [86] T. Dittrich, P. Hänggi, G.-L. Ingold, B. Kramer, G. Schön, and W. Zwerger, *Quantum Transport and Dissipation* (Wiley-VCH, Weinheim, 1998).
- [87] H. S. J. van der Zant, private communication (2009).
- [88] M. Born and E. Wolf, *Principles of Optics* (Cambridge University Press, Cambridge, 2002).
- [89] W. L. Barnes, A. Dereux, and T. W. Ebbesen, *Surface plasmon subwavelength optics*, Nature **424**, 824 (2003).
- [90] S. A. Maier, *Plasmonics: Fundamentals and Applications* (Springer, Berlin, 2007).
- [91] T. Klar, M. Perner, S. Grosse, G. von Plessen, W. Spirkl, and J. Feldmann, *Surface-plasmon resonances in single metallic nanoparticles*, Phys. Rev. Lett. **80**, 4249 (1998).
- [92] U. Kreibig and M. Vollmer, *Optical Properties of Metal Clusters* (Springer, Berlin, 1995).
- [93] K. Kneipp, Y. Wang, H. Kneipp, L. T. Perelman, I. Itzkan, R. R. Dasari, and M. S. Feld, *Single molecule detection using surface-enhanced Raman scattering (SERS)*, Phys. Rev. Lett. **78**, 1667 (1997).
- [94] V. G. Veselago, *The electrodynamics of substances with simultaneously negative values of ϵ and μ* , Sov. Phys. Usp. **10**, 509 (1968).
- [95] D. R. Smith, W. J. Padilla, D. C. Vier, S. C. Nemat-Nasser, and S. Schultz, *Composite medium with simultaneously negative permeability and permittivity*, Phys. Rev. Lett. **84**, 4184 (2000).

- [96] R. A. Shelby, D. R. Smith, and S. Schultz, *Experimental verification of a negative index of refraction*, Science **292**, 77 (2001).
- [97] J. B. Pendry, *Negative refraction makes a perfect lens*, Phys. Rev. Lett. **85**, 3966 (2000).
- [98] N. Fang, H. Lee, C. Sun, and X. Zhang, *Subdiffraction-limited optical imaging with a silver superlens*, Science **308**, 534 (2005).
- [99] U. Leonhardt, *Optical conformal mapping*, Science **312**, 1777 (2006).
- [100] J. B. Pendry, D. Schurig, and D. R. Smith, *Controlling electromagnetic fields*, Science **312**, 1780 (2006).
- [101] D. Schurig, J. J. Mock, B. J. Justice, S. A. Cummer, J. B. Pendry, A. F. Starr, and D. R. Smith, *Metamaterial electromagnetic cloak at microwave frequencies*, Science **314**, 977 (2006).
- [102] K. L. Tsakmakidis, A. D. Boardman, and O. Hess, *“Trapped rainbow” storage of light in metamaterials*, Nature **450**, 397 (2007).
- [103] A. Silva, F. Monticone, G. Castaldi, V. Galdi, A. Alù, and N. Engheta, *Performing mathematical operations with metamaterials*, Science **343**, 160 (2014).
- [104] J. R. Krenn, A. Dereux, J. C. Weeber, E. Bourillot, Y. Lacroute, J. P. Goudonnet, G. Schider, W. Gotschy, A. Leitner, F. R. Aussenegg, et al., *Squeezing the optical near-field zone by plasmon coupling of metallic nanoparticles*, Phys. Rev. Lett. **82**, 2590 (1999).
- [105] S. A. Maier, M. L. Brongersma, P. G. Kik, and H. A. Atwater, *Observation of near-field coupling in metal nanoparticle chains using far-field polarization spectroscopy*, Phys. Rev. B **65**, 193408 (2002).
- [106] N. Féridj, J. Aubard, G. Lévi, J. R. Krenn, G. Schider, A. Leitner, and F. R. Aussenegg, *Enhanced substrate-induced coupling in two-dimensional gold nanoparticle arrays*, Phys. Rev. B **66**, 245407 (2002).
- [107] S. Maier, P. G. Kik, H. A. Atwater, S. Meltzer, E. Harel, B. E. Koel, and A. A. G. Requicha, *Local detection of electromagnetic energy transport below the diffraction limit in metal nanoparticle plasmon waveguides*, Nature Mater. **2**, 229 (2003).
- [108] L. A. Sweatlock, S. A. Maier, H. A. Atwater, J. J. Penninkhof, and A. Polman, *Highly confined electromagnetic fields in arrays of strongly coupled Ag nanoparticles*, Phys. Rev. B **71**, 235408 (2005).
- [109] D. K. Polyushkin, E. Hendry, E. K. Stone, and W. L. Barnes, *THz generation from plasmonic nanoparticle arrays*, Nano Lett. **11**, 4718 (2011).
- [110] M. Quinten, A. Leitner, J. R. Krenn, and F. R. Aussenegg, *Electromagnetic energy transport via linear chains of silver nanoparticles*, Opt. Lett. **23**, 1331 (1998).
- [111] M. L. Brongersma, J. W. Hartman, and H. A. Atwater, *Electromagnetic energy transfer and switching in nanoparticle chain arrays below the diffraction limit*, Phys. Rev. B **62**, R16356 (2000).

Bibliography

- [112] S. Y. Park and D. Stroud, *Surface-plasmon dispersion relations in chains of metallic nanoparticles: An exact quasistatic calculation*, Phys. Rev. B **69**, 125418 (2004).
- [113] W. H. Weber and G. W. Ford, *Propagation of optical excitations by dipolar interactions in metal nanoparticle chains*, Phys. Rev. B **70**, 125429 (2004).
- [114] A. F. Koenderink and A. Polman, *Complex response and polariton-like dispersion splitting in periodic metal nanoparticle chains*, Phys. Rev. B **74**, 033402 (2006).
- [115] A. F. Koenderink, *Plasmon nanoparticle array waveguides for single photon and single plasmon sources*, Nano Lett. **9**, 4228 (2009).
- [116] N. Meinzer, W. L. Barnes, and I. R. Hooper, *Plasmonic meta-atoms and metasurfaces*, Nature Photon. **8**, 889 (2014).
- [117] K. T. Carron, W. Fluhr, M. Meier, A. Wokaun, and H. W. Lehmann, *Resonances of two-dimensional particle gratings in surface-enhanced Raman scattering*, J. Opt. Soc. Am. B **3**, 430 (1986).
- [118] S. Zou, N. Janel, and G. C. Schatz, *Silver nanoparticle array structures that produce remarkably narrow plasmon lineshapes*, J. Chem. Phys. **120**, 10871 (2004).
- [119] V. G. Kravets, F. Schedin, and A. N. Grigorenko, *Extremely narrow plasmon resonances based on diffraction coupling of localized plasmons in arrays of metallic nanoparticles*, Phys. Rev. Lett. **101**, 087403 (2008).
- [120] B. Auguie and W. L. Barnes, *Collective resonances in gold nanoparticle arrays*, Phys. Rev. Lett. **101**, 143902 (2008).
- [121] Y. Chu, E. Schonbrun, T. Yang, and K. B. Crozier, *Experimental observation of narrow surface plasmon resonances in gold nanoparticle arrays*, Appl. Phys. Lett. **93**, 181108 (2008).
- [122] S. R. K. Rodriguez, G. Lozano, M. A. Verschuuren, R. Gomes, K. Lambert, B. De Geyter, A. Hassinen, D. Van Thourhout, Z. Hens, and J. Gómez Rivas, *Quantum rod emission coupled to plasmonic lattice resonances: A collective directional source of polarized light*, Appl. Phys. Lett. **100**, 111103 (2012).
- [123] S. R. K. Rodriguez, A. Abass, B. Maes, O. T. A. Janssen, G. Vecchi, and J. Gómez Rivas, *Coupling bright and dark plasmonic lattice resonances*, Phys. Rev. X **1**, 021019 (2011).
- [124] H. A. Atwater and A. Polman, *Plasmonics for improved photovoltaic devices*, Nature Mater. **9**, 205 (2010).
- [125] K. S. Novoselov, A. K. Geim, S. V. Morozov, D. Jiang, Y. Zhang, S. V. Dubonos, I. V. Grigorieva, and A. A. Firsov, *Electric field effect in atomically thin carbon films*, Science **306**, 666 (2004).
- [126] P. R. Wallace, *The band theory of graphite*, Phys. Rev. **71**, 622 (1947).
- [127] A. H. Castro Neto, F. Guinea, N. M. R. Peres, K. S. Novoselov, and A. K. Geim, *The electronic properties of graphene*, Rev. Mod. Phys. **81**, 109 (2009).

- [128] K. S. Novoselov, A. K. Geim, S. M. Morozov, D. Jiang, M. I. Katsnelson, I. V. Grigorieva, S. V. Dubonos, and A. A. Firsov, *Two-dimensional gas of massless Dirac fermions in graphene*, Nature **438**, 197 (2005).
- [129] Y. Zhang, Y.-W. Tan, H. L. Stormer, and P. Kim, *Experimental observation of the quantum Hall effect and Berry's phase in graphene*, Nature **438**, 201 (2005).
- [130] V. V. Cheianov and V. I. Fal'ko, *Selective transmission of Dirac electrons and ballistic magnetoresistance of n-p junctions in graphene*, Phys. Rev. B **74**, 041403(R) (2006).
- [131] D. Han, Y. Lai, J. Zi, Z.-Q. Zhang, and C. T. Chan, *Dirac spectra and edge states in honeycomb plasmonic lattices*, Phys. Rev. Lett. **102**, 123904 (2009).
- [132] F. D. M. Haldane and S. Raghu, *Possible realization of directional optical waveguides in photonic crystals with broken time-reversal symmetry*, Phys. Rev. Lett. **100**, 013904 (2008).
- [133] O. Peleg, G. Bartal, B. Freedman, O. Manela, M. Segev, and D. N. Christodoulides, *Conical diffraction and gap solitons in honeycomb photonic lattices*, Phys. Rev. Lett. **98**, 103901 (2007).
- [134] R. A. Sepkhanov, Y. B. Bazaliy, and C. W. J. Beenakker, *Extremal transmission at the Dirac point of a photonic band structure*, Phys. Rev. A **75**, 063813 (2007).
- [135] R. A. Sepkhanov, J. Nilsson, and C. W. J. Beenakker, *Proposed method for detection of the pseudospin- $\frac{1}{2}$ Berry phase in a photonic crystal with a Dirac spectrum*, Phys. Rev. B **78**, 045122 (2008).
- [136] S. R. Zandbergen and M. J. A. de Dood, *Experimental observation of strong edge effects on the pseudodiffusive transport of light in photonic graphene*, Phys. Rev. Lett. **104**, 043903 (2010).
- [137] J. Bravo-Abad, J. D. Joannopoulos, and M. Soljačić, *Enabling single-mode behavior over large areas with photonic Dirac cones*, Proc. Natl. Acad. Sci. USA **109**, 9761 (2012).
- [138] D. Torrent and J. Sánchez-Dehesa, *Acoustic analogue of graphene: Observation of Dirac cones in acoustic surface waves*, Phys. Rev. Lett. **108**, 174301 (2012).
- [139] L. Tarruell, D. Greif, T. Uehlinger, G. Jotzu, and T. Esslinger, *Creating, moving and merging Dirac points with a Fermi gas in a tunable honeycomb lattice*, Nature **483**, 302 (2012).
- [140] M. Bellec, U. Kuhl, G. Montambaux, and F. Mortessagne, *Topological transition of Dirac points in a microwave experiment*, Phys. Rev. Lett. **110**, 033902 (2013).
- [141] M. Bellec, U. Kuhl, G. Montambaux, and F. Mortessagne, *Tight-binding couplings in microwave artificial graphene*, Phys. Rev. B **88**, 115437 (2013).
- [142] T. Jacqmin, I. Carusotto, I. Sagnes, M. Abbarchi, D. D. Solnyshkov, G. Malpuech, E. Galopin, A. Lemaitre, J. Bloch, and A. Amo, *Direct observation of Dirac cones and a flatband in a honeycomb lattice for polaritons*, Phys. Rev. Lett. **112**, 116402 (2014).

Bibliography

- [143] M. Milicevic, T. Ozawa, P. Andreakou, I. Carusotto, T. Jacqmin, E. Galopin, A. Lemaître, L. Le Gratiet, I. Sagnes, J. Bloch, and A. Amo, *Edge states in polariton honeycomb lattices*, arXiv:1504.05761.
- [144] M. Polini, F. Guinea, H. C. M. M. Lewenstein, and V. Pellegrini, *Artificial honeycomb lattices for electrons, atoms and photons*, Nature Nanotech. **8**, 625 (2013).
- [145] L. M. Woods and G. D. Mahan, *Electron-phonon effects in graphene and armchair (10,10) single-wall carbon nanotubes*, Phys. Rev. B **61**, 10651 (2000).
- [146] H. Suzuura and T. Ando, *Phonons and electron-phonon scattering in carbon nanotubes*, Phys. Rev. B **65**, 235412 (2002).
- [147] I. M. Lifshitz, Sov. Phys. JETP **21**, 1130 (1960).
- [148] A. Kawabata and R. Kubo, *Electronic properties of fine metallic particles - II. Plasma resonance absorption*, J. Phys. Soc. Jpn. **21**, 1765 (1966).
- [149] C. Yannouleas and R. Broglia, *Landau damping and wall dissipation in large metal clusters*, Ann. Phys. (NY) **217**, 105 (1992).
- [150] L. G. Gerchikov, C. Guet, and A. N. Ipatov, *Multiple plasmons and anharmonic effects in small metallic clusters*, Phys. Rev. A **66**, 053202 (2002).
- [151] R. A. Molina, D. Weinmann, and R. A. Jalabert, *Oscillatory size dependence of the surface plasmon linewidth in metallic nanoparticles*, Phys. Rev. B **65**, 155427 (2002).
- [152] H. Tamaru, H. Kuwata, H. T. Miyazaki, and K. Miyano, *Resonant light scattering from individual Ag nanoparticles and particle pairs*, Appl. Phys. Lett. **80**, 1826 (2002).
- [153] W. Rechberger, A. Hohenau, A. Leitner, J. Krenn, B. Lamprecht, and F. Aussenegg, *Optical properties of two interacting gold nanoparticles*, Opt. Commun. **220**, 137 (2003).
- [154] P. Olk, J. Renger, M. T. Wenzel, and L. M. Eng, *Distance dependent spectral tuning of two coupled metal nanoparticles*, Nano Lett. **8**, 1174 (2008).
- [155] P. K. Jain and M. A. El-Sayed, *Plasmonic coupling in noble metal nanostructures*, Chem. Phys. Lett. **487**, 153 (2010).
- [156] M.-W. Chu, V. Myroshnychenko, C. H. Chen, J.-P. Deng, C.-Y. Mou, and F. J. García de Abajo, *Probing bright and dark surface-plasmon modes in individual and coupled noble metal nanoparticles using an electron beam*, Nano Lett. **9**, 399 (2009).
- [157] A. L. Koh, K. Bao, I. Khan, W. E. Smith, G. Kothleitner, P. Nordlander, S. A. Maier, and D. W. McComb, *Electron energy-loss spectroscopy (EELS) of surface plasmons in single silver nanoparticles and dimers: Influence of beam damage and mapping of dark modes*, ACS Nano **3**, 3015 (2009).
- [158] S. J. Barrow, D. Rossouw, A. M. Funston, G. A. Botton, and P. Mulvaney, *Mapping bright and dark modes in gold nanoparticle chains using electron energy loss spectroscopy*, Nano Lett. **14**, 3799 (2014).

- [159] R. Ruppin, *Surface modes of two spheres*, Phys. Rev. B **26**, 3440 (1982).
- [160] J. M. Gérardy and M. Ausloos, *Absorption spectrum of clusters of spheres from the general solution of Maxwell's equations. IV. Proximity, bulk, surface, and shadow effects (in binary clusters)*, Phys. Rev. B **27**, 6446 (1983).
- [161] P. Nordlander, C. Oubre, E. Prodan, K. Li, and M. I. Stockman, *Plasmon hybridization in nanoparticle dimers*, Nano Lett. **4**, 899 (2004).
- [162] C. Dahmen, B. Schmidt, and G. von Plessen, *Radiation damping in metal nanoparticle pairs*, Nano Lett. **7**, 318 (2007).
- [163] G. Bachelier, I. Russier-Antoine, E. Benichou, C. Jonin, N. Del Fatti, F. Vallée, and P.-F. Brevet, *Fano profiles induced by near-field coupling in heterogeneous dimers of gold and silver nanoparticles*, Phys. Rev. Lett. **101**, 197401 (2008).
- [164] J. Zuloaga, E. Prodan, and P. Nordlander, *Quantum description of the plasmon resonances of a nanoparticle dimer*, Nano Lett. **9**, 887 (2009).
- [165] R. Esteban, A. G. Borisov, P. Nordlander, and J. Aizpurua, *Bridging quantum and classical plasmonics with a quantum-corrected model*, Nature Comm. **3**, 825 (2012).
- [166] P. Zhang, J. Feist, A. Rubio, P. García-González, and F. J. García-Vidal, *Ab-initio nanoplasmonics: atoms matter*, Phys. Rev. B **90**, 161407(R) (2014).
- [167] G. F. Bertsch and R. A. Broglia, *Oscillations in Finite Quantum Systems* (Oxford University Press, Oxford, 1994).
- [168] W. Kohn, *Cyclotron resonance and de Haas-van Alfen oscillations of an interacting electron gas*, Phys. Rev. **123**, 1242 (1961).
- [169] L. Jacak, P. Hawrylak, and A. Wójs, *Quantum Dots* (Springer-Verlag, Berlin, 1998).
- [170] Equation (2.23) corrects an error in Eq. (8) of Ref. [30].
- [171] C. Tsallis, *Diagonalization methods for the general bilinear Hamiltonian of an assembly of bosons*, J. Math. Phys. **19**, 277 (1978).
- [172] A. Brandstetter-Kunc, G. Weick, D. Weinmann, and R. A. Jalabert, unpublished.
- [173] G. S. Smith, *An insightful problem involving the electromagnetic radiation from a pair of dipoles*, Eur. J. Phys. **31**, 819 (2010).
- [174] K.-P. Charlé, W. Schulze, and B. Winter, *The size dependent shift of the surface plasmon absorption band of small spherical metal particles*, Z. Phys. D **12**, 471 (1989).
- [175] O. L. Krivanek, T. C. Lovejoy, N. Dellby, T. Aoki, R. W. Carpentera, P. Rez, E. Soignard, J. Zhu, P. E. Batson, M. J. Lagos, et al., *Vibrational spectroscopy in the electron microscope*, Nature **514**, 209 (2014).
- [176] D. Felbacq, *Commentary: Quantum way for metamaterials*, J. Nanophotonics **5**, 050302 (2011).

Bibliography

- [177] A. Brandstetter-Kunc, G. Weick, D. Weinmann, and R. A. Jalabert, in preparation.
- [178] U. Fano, *Atomic theory of electromagnetic interactions in dense materials*, Phys. Rev. **103**, 1202 (1956).
- [179] J. J. Hopfield, *Theory of the contribution of excitons to the complex dielectric constant of crystals*, Phys. Rev. **112**, 1555 (1958).
- [180] S. J. Tan, M. J. Campolongo, D. Luo, and W. Cheng, *Building plasmonic nanostructures with DNA*, Nature Nanotech. **6**, 268 (2011).
- [181] C. Cohen-Tannoudji, J. Dupont-Roc, and G. Grynberg, *Photons and Atoms: Introduction to Quantum Electrodynamics* (Wiley-VCH, Weinheim, 2004).
- [182] V. M. Agranovich and V. L. Ginzburg, *Crystal Optics with Spatial Dispersion, and Excitons* (Springer-Verlag, Berlin, 1984).
- [183] F. Hellbach, *Tunable plasmon polaritons in arrays of interacting metallic nanoparticles* (Bachelor thesis, Universität Konstanz, 2014).
- [184] S. Lamowki, F. Hellbach, F. Pauly, and G. Weick, in preparation.
- [185] G. Weick and E. Mariani, unpublished.
- [186] L. D. Landau and E. M. Lifshitz, *Mechanics* (Pergamon, Oxford, 1976).
- [187] I. Bloch, J. Dalibard, and W. Zwerger, *Many-body physics with ultracold gases*, Rev. Mod. Phys. **80**, 885 (2008).
- [188] T. Stöferle, H. Moritz, C. Schori, M. Köhl, and T. Esslinger, *Transition from a strongly interacting 1d superfluid to a Mott insulator*, Phys. Rev. Lett. **92**, 130403 (2004).
- [189] C. Tozzo, M. Krämer, and F. Dalfovo, *Stability diagram and growth rate of parametric resonances in Bose-Einstein condensates in one-dimensional optical lattices*, Phys. Rev. A **72**, 023613 (2005).
- [190] L. Goren, E. Mariani, and A. Stern, *Probing the superfluid Mott-insulating shell structure of cold atoms by parametric excitations*, Phys. Rev. A **75**, 063612 (2007).
- [191] G. F. Giuliani and G. Vignale, *Quantum Theory of the Electron Liquid* (Cambridge University Press, Cambridge, 2005).
- [192] T. Giamarchi, *Quantum Physics in One Dimension* (Oxford University Press, Oxford, 2004).
- [193] P. W. Brouwer, *Theory of Many-Particle Systems*, Lecture notes (Cornell University, 2005).
- [194] S. M. Reimann and M. Manninen, *Electronic structure of quantum dots*, Rev. Mod. Phys. **74**, 1283 (2002).
- [195] O. M. Auslaender, H. Steinberg, A. Yacoby, Y. Tserkovnyak, B. I. Halperin, K. W. Baldwin, L. N. Pfeiffer, and K. W. West, *Spin-charge separation and localization in one dimension*, Science **308**, 88 (2005).

- [196] B. J. Kim, H. Koh, E. Rotenberg, S.-J. Oh, H. Eisaki, N. Motoyama, S. Uchida, T. Tohyama, S. Maekawa, Z.-X. Shen, et al., *Distinct spinon and holon dispersions in photoemission spectral functions from one-dimensional SrCuO₂*, Nature Phys. **2**, 397 (2006).
- [197] A. Recati, P. O. Fedichev, W. Zwerger, and P. Zoller, *Spin-charge separation in ultracold quantum gases*, Phys. Rev. Lett. **90**, 020401 (2003).
- [198] L. Kecke, H. Grabert, and W. Häusler, *Charge and spin dynamics of interacting fermions in a one-dimensional harmonic trap*, Phys. Rev. Lett. **94**, 176802 (2005).
- [199] C. Kollath, U. Schollwöck, and W. Zwerger, *Spin-charge separation in cold Fermi gases: A real time analysis*, Phys. Rev. Lett. **95**, 176401 (2005).
- [200] M. Polini and G. Vignale, *Spin drag and spin-charge separation in cold Fermi gases*, Phys. Rev. Lett. **98**, 266403 (2007).
- [201] A. Kleine, C. Kollath, I. P. McCulloch, T. Giamarchi, and U. Schollwöck, *Spin-charge separation in two-component Bose gases*, Phys. Rev. A **77**, 013607 (2008).
- [202] L. Mathey, E. Altman, and A. Vishwanath, *Noise correlations in one-dimensional systems of ultracold fermions*, Phys. Rev. Lett. **100**, 240401 (2008).
- [203] Y. Kagan and L. A. Manakova, *Parametric generation of density and spin modes with formation of stationary condensed states in ultracold two-component quasi-one-dimensional Fermi gases*, Phys. Rev. A **80**, 023625 (2009).
- [204] M. Dalmonte, G. Pupillo, and P. Zoller, *One-dimensional quantum liquids with power-law interactions: The Luttinger staircase*, Phys. Rev. Lett. **105**, 140401 (2010).
- [205] P. Pirooznia and P. Kopietz, *Damping of zero sound in Luttinger liquids*, Eur. Phys. J. B **58**, 291 (2007).
- [206] M. Olshanii, *Atomic scattering in the presence of an external confinement and a gas of impenetrable bosons*, Phys. Rev. Lett. **81**, 938 (1998).
- [207] W. Ketterle and M. W. Zwierlein, *Making, probing and understanding ultracold Fermi gases*, in Ultracold Fermi Gases, Proceedings of the International School of Physics “Enrico Fermi”, Course CLXIV, Varenna, 20–30 June 2006, edited by M. Inguscio, W. Ketterle and C. Salomon (IOS Press, Amsterdam, 2008).
- [208] S. J. Allen, H. L. Störmer, and J. C. M. Hwang, *Dimensional resonance of the two-dimensional electron gas in selectively doped GaAs/AlGaAs heterostructures*, Phys. Rev. B **28**, 4875(R) (1983).
- [209] C. Sikorski and U. Merkt, *Spectroscopy of electronic states in InSb quantum dots*, Phys. Rev. Lett. **62**, 2164 (1989).
- [210] B. Meurer, D. Heitmann, and K. Ploog, *Single-electron charging of quantum-dot atoms*, Phys. Rev. Lett. **68**, 1371 (1992).
- [211] W. H. Louisell, A. Yariv, and A. E. Siegman, *Quantum fluctuations and noise in parametric processes – I*, Phys. Rev. **124**, 1646 (1961).

Bibliography

- [212] J. P. Gordon, W. H. Louisell, and L. R. Walker, *Quantum fluctuations and noise in parametric processes – II*, Phys. Rev. **129**, 481 (1963).
- [213] B. R. Mollow and R. J. Glauber, *Quantum theory of parametric amplification – I*, Phys. Rev. **160**, 1076 (1967).
- [214] B. R. Mollow and R. J. Glauber, *Quantum theory of parametric amplification – II*, Phys. Rev. **160**, 1097 (1967).
- [215] D. F. Walls and G. J. Milburn, *Quantum Optics* (Springer-Verlag, Berlin, 1994).
- [216] H.-P. Breuer and F. Petruccione, *The Theory of Open Quantum Systems* (Oxford University Press, Oxford, 2002).
- [217] B. Ferguson and X.-C. Zhang, *Materials for terahertz science and technology*, Nature Mater. **1**, 26 (2002).
- [218] M. Tonouchi, *Cutting-edge terahertz technology*, Nature Photon. **1**, 97 (2007).
- [219] M. I. Dyakonov, *Generation and detection of terahertz radiation by field effect transistors*, C. R. Phys. **11**, 413 (2010).
- [220] T. Maltezopoulos, A. Bolz, C. Meyer, C. Heyn, W. Hansen, M. Morgenstern, and R. Wiesendanger, *Wave-function mapping of InAs quantum dots by scanning tunneling spectroscopy*, Phys. Rev. Lett. **91**, 196804 (2003).
- [221] T. H. Oosterkamp, S. F. Godijn, M. J. Uilenreef, Y. V. Nazarov, N. C. van der Vaart, and L. P. Kouwenhoven, *Changes in the magnetization of a double quantum dot*, Phys. Rev. Lett. **80**, 4951 (1998).
- [222] M. P. Schwarz, D. Grundler, M. Wilde, C. Heyn, and D. Heitmann, *Magnetization of semiconductor quantum dots*, J. Appl. Phys. **91**, 6875 (2002).
- [223] R. Kubo, *Electronic properties of fine metallic particles - I.*, J. Phys. Soc. Jpn. **17**, 975 (1962).
- [224] W. P. Halperin, *Quantum size effects in metal particles*, Rev. Mod. Phys. **58**, 533 (1986).
- [225] W. D. Knight, K. Clemenger, W. A. de Heer, W. A. Saunders, M. Y. Chou, and M. L. Cohen, *Electronic shell structure and abundances of sodium clusters*, Phys. Rev. Lett. **52**, 2141 (1984).
- [226] W. A. de Heer, *The physics of simple metal clusters: experimental aspects and simple models*, Rev. Mod. Phys. **65**, 611 (1993).
- [227] M. Brack, *The physics of simple metal clusters: self-consistent jellium model and semi-classical approaches*, Rev. Mod. Phys. **65**, 677 (1993).